Universitat de les Illes Balears

Departament de Física

PhD thesis

Programa de doctorat dels Estudis Oficials de Postgrau:
Doctorat de Física

Gravitational wave observation of compact binaries

Detection, parameter estimation and template accuracy

Miquel Trias Cornellana

(Advisor: Dr. Alicia M. Sintes)

November 2010

Universitat de les Illes Balears

Gravitational wave observation of compact binaries: detection, parameter estimation and template accuracy

by
Miquel Trias Cornellana

THESIS
Presented to the Physics Department of
Universitat de les Illes Balears
in Partial Fulfillment
of the Requirements
for the Degree of

DOCTOR
in
PHYSICS

November 2010

Gravitational wave observation of compact binaries: detection, parameter estimation and template accuracy

Miquel Trias (`miquel.trias@uib.es`)
Departament de Física, Universitat de les Illes Balears,
Carretera de Valldemossa km. 7.5, 07122 Palma de Mallorca, Spain

PhD Thesis

Supervisor: Dr. Alicia M. Sintes

This document was typeset with $\text{\LaTeX}\,2_\varepsilon$

La directora de tesi Alicia M. Sintes Olives, Professora titular d'universitat de la Universitat de les Illes Balears, adscrita al Departament de Física, certifica que aquesta tesi doctoral ha estat realitzada pel Sr. Miquel Trias Cornellana, i perquè en quedi constància escrita, signa la present

a Palma de Mallorca, 29 de Novembre de 2010,

Dr. Alicia M. Sintes   Miquel Trias

Resum (en català)

En aquesta tesi es presenten els resultats obtinguts en tres línies de recerca diferents, totes elles relacionades amb l'anàlisi de dades per a la detecció directa d'ones gravitatòries emeses per sistemes binaris d'objectes compactes (forats negres, estels de neutrons, nanes blanques) de massa similar.

Per una banda, hem estudiat quina serà l'estimació de paràmetres que es podrà fer quan s'observin les ones gravitatòries emeses pels xocs entre dos forats negres supermassius (normalment, situats als centres de les galàxies) en la seva fase *inspiral* amb el futur detector interferomètric espacial d'ones gravitatòries, LISA. En particular, estudiem l'impacte que té la inclusió de tots els harmònics de la senyal en l'estimació de paràmetres, i ho comparem amb el resultat clàssic allà on només es considerava l'harmònic dominant de la senyal (el corresponent a una freqüència $2f_{\mathrm{orb}}$); veure Cap. 4. Els resultats obtinguts confirmen la gran importància d'emprar la senyal completa (amb tots els harmònics), bàsicament per dos motius: en primer lloc, ja que incrementen el rang de masses en el que LISA podrà detectar senyals d'ones gravitatòries procedents d'aquests objectes; però principalment, perquè la seva inclusió augmenta la riquesa dels detalls de la senyal rebuda, de manera que es fa més fàcil distingir entre dues senyals amb distints paràmetres i per tant, es redueixen significativament (fins a diversos ordres de magnitud) els errors en la seva estimació. A conseqüència d'aquest important resultat, també hem estudiat el nombre esperat de fonts que LISA detectarà cada any amb un cert error donat [tant en la determinació de la distància, com de la posició al cel], i en funció del model de formació de galàxies que es considera per al nostre Univers; i per altra banda, la precisió amb la què podríem mesurar l'equació d'estat de l'energia fosca a partir d'una única observació de LISA (veure Cap. 5). Les conclusions d'aquests dos darrers estudis és que LISA observarà cada any, unes 20 fonts (només de xocs entre forats negres supermassius) amb precisió de fins al 10% en la mesura de la distància, 10 fonts amb una resolució al cel millor de 10 deg^2 i el que és més interessant, esperem observar $1-3$ fonts amb una exel·lent precisió, tant en la determinació de la posició al cel (millor que 1 deg^2) com de la distància (millor de l'1%); tot plegat ens permetrà emprar LISA per a realitzar cosmografia de precisió, sempre i quan puguem eliminar l'efecte de lents gravitatòries creat pels objectes que hi ha entre nosaltres i les fonts que volem estudiar a $0.5 < z < 1$.

Per altra banda, hem desenvolupat un algorisme de cerca de senyals gravitatòries procedents de sistemes binaris estel·lars situats dins la nostra pròpia galàxia. Aquest algorisme està basat en la interpretació Bayesiana de la probabilitat i empra tècniques d'integració

per Monte Carlo mitjançant cadenes de Markov (MCMC) de manera que ens permet, no només detectar les senyals, sinó que alhora estimem la distribució de probabilitat dels paràmetres que caracteritzen la font. S'espera que el detector LISA observi simultàniament desenes de milers d'aquestes senyals, així doncs, la distinció entre cadascuna d'elles és una tasca que es realitza amb l'anàlisi de dades posterior. En aquesta tesi, hem implementat un mètode que serveix tant per cercar una única senyal dins les dades, com un nombre fixat d'elles (veure Cap. 6). A més, hem desenvolupat un algorisme totalment general i que preserva el caràcter Markovià de la cadena que es genera, basat en el *Delayed Rejection* per tal de mostrejar eficientment funcions que presenten una estructura multimodal (és a dir, que tenen diversos màxims relatius separats per una certa distància); veure Cap. 7. Aquest tipus d'estructures són molt comuns en un nombre molt divers d'aplicacions del MCMC (no només en l'area d'anàlisi de dades d'ones gravitatòries, ni tan sols únicament en l'àrea de Física) i la presència de diversos màxims de la funció pot reduir considerablement l'eficiència dels mètodes de mostreig. L'algorisme que nosaltres hem dissenyat, esperem que pugui solventar aquest tipus de situacions, que són particularment comuns i rellevants en l'anàlisi de dades per LISA.

Finalment, la tercera línia de recerca portada a terme durant el doctorat ha consistit en estudiar el rang de validesa dels models de patrons d'ones gravitatòries (emeses per sistemes binaris compactes) més ràpids de generar computacionalment que existeixen, però que alhora contenen certes aproximacions. El context d'aquest estudi es troba en les cerques que actualment es fan amb els detectors interferomètrics terrestres (LIGO i Virgo) d'una de les fonts més prometedores de ser detectada: el xoc entre dos forats negres (o estels de neutrons) de fins a $500 M_\odot$. Tots els mètodes de cerca emprats es basen comparar les dades mesurades, amb els patrons teòrics que esperem que estiguin continguts dins aquestes en cas de que hi hagi una senyal (*matched filtering*); com més s'ajustin aquests patrons a la senyal real, més possibilitats hi ha de reconèixer-la d'entre el renou. Així doncs, per una banda necessitem que els patrons emprats en la cerca siguin el més precisos possible, però per l'altra, resulta que hem cobrir tot l'espai de paràmetres, el que implica la generació de molts d'aquests patrons, així que també requerirem que siguin ràpids de generar. En el Cap. 8 definim matemàticament quins són els requisits mínims de precisió que han de satisfer els models de patrons d'ones gravitatòries i estudiem per quin rang de masses es poden emprar els models més ràpids, aquells que directament ens donen una expressió analítica tancada per als patrons. Les conclusions que obtenim són que aquests models ràpids ens garanteixen (per sistemes amb una relació de masses entre 1:1 i 4:1) no perdre més de 6% de les possibles senyals quan es consideren els detectors actuals i no més del 9% quan es consideren detectors avançats. Per sistemes amb un quocient de masses major i en qualsevol cas en què un estigui interessat no només en detectar la senyal, sinó també en extreure informació creïble sobre els paràmetres físics mesurats; aleshores serà necessari emprar models més precisos.

Acknowledgements

I would like to express my sincere gratitude to my thesis advisor, Dr. Alicia M. Sintes, for introducing me to research and for her guidance and help during these four years.

I would like to especially thank Prof. Alberto Vecchio for all the invaluable lessons, advices and ideas that I received from him, and also for his hospitality during the many times that I visited the University of Birmingham. He truly has been like a co-advisor to me during all these years.

I also would like to thank Prof. Thibault Damour for many useful discussions and suggestions, and for his hospitality during my visit at the Institut des Hautes Études Scientifiques (IHÉS) in the autumn 2009. From him I have learned the power of thoroughness and simplicity in science.

I am grateful to Dr. John Veitch for "converting" me to Bayesian statistics and showing to me how powerful it can be, and also for his infinite patience in the development and implementation of the algorithms described in Chapters 6 and 7. I thank Dr. Alessandro Nagar for all the useful discussions we had about the physics behind a compact binary coalescence, also for his (and his wife's) hospitality during my visit at the IHÉS and specially for his encouragement and support during this last year.

I would like to thank all my colleagues from the UIB Agencia EFE and the Relativity and Gravitation group at the UIB for all their support and specially to Dr. Sascha Husa for many valuable discussions and suggestions.

I thank Dr. Alexander Stroeer for sharing his MCMC code, which facilitated the development of the software used in Chapter 6. I am grateful to Dr. Badri Krishnan, Dr. Stanislav Babak, Dr. Edward K. Porter and Dr. Jonathan R. Gair for all the discussions we had about extreme mass ratio inspiral signals while I was visiting the Albert Einstein Institute (AEI) in the spring 2007. I also would like to thank Prof. Bangalore S. Sathyaprakash, Dr. Chris Van Den Broeck and all the members of the LISA Performance Evaluation Taskforce[1] for many useful discussions about LISA parameter estimation and higher harmonics.

I thank the organizers of the LIGO Astrowatch program and all the scientists, operators and other 'astrowatchers' of the LIGO Hanford Observatory that had the patience to

---

[1] `http://www.tapir.caltech.edu/dokuwiki/lisape:home`

teach me how to operate an interferometer and more importantly that became friends in the middle of that desert.

I would like to thank all the institutions where I spent some of the time of my doctorate for hospitality and the possibility of meeting new people: the University of Birmingham (Prof. Alberto Vecchio), the AEI (Prof. Bernard F. Schutz, Dr. Badri Krishnan and Dr. Maria A. Papa), the LIGO Hanford Observatory (Prof. Fred Raab and Dr. Michael Landry) and the IHÉS (Prof. Thibault Damour). In all of them I took many valuable lessons.

Volia agrair el suport i consells rebuts per part de tota la meva família: pares, germanes, padrins, . . . Heu estat sempre allà en els moments difícils, preocupant-vos i assessorant-me per trobar el camí que m'ha permès arribar fins aquí.

Dono les gràcies a tots els meus companys de voleibol de la UIB per la seva amistat i per proporcionar-me aquestes dues hores setmanals d'adrenalina i desconnexió que tant he agraït, sobretot en aquests darrers mesos d'escriptura. En especial, hem d'estar agraïts a Rubén Santamarta per iniciar i mantenir viva aquesta activitat.

Tampoc m'oblido dels meus amics. Aquesta és la primera de cinc tesis que començaren com a discussions de cafè i gelat ara ja fa gairebé deu anys per allà per Porto Pí; gràcies Toni, Víctor, Pau i Javi per tot el suport, força i afecte que m'heu donat durant aquests anys, sabeu que és recíproc! Moltes gràcies també a Aina, Esther i Sergio, parte de esta tesis también es gracias a vuestro apoyo.

Finalment, el meu agraïment més especial és per na Llucia, la meva millor amiga, companya i al·lota des de fa deu anys i mig. Amb ella he compartit tots els instants dels darrers quatre anys; hem viscut plegats els millors moments del doctorat [el meu primer article, creuant mitja Europa en cotxo, vivint tres mesos enmig d'un desert americà, el dia en què el DR a la fi va funcionar, els *shifts* al detector de Hanford, el congrés a Nova York. . .], però sobretot sempre hi ha estat quan més ho he necessitat [el primer cap de setmana en aquella casa de Birmingham, els *deadlines* dels MLDCs, els dies previs a la xerrada als Amaldi, l'escriptura de la tesi. . .]. Al mirar aquesta tesi, veig un recull de les experiències que hem viscut plegats.

Contents

Preface

This thesis is divided in two different parts, clearly separating what corresponds to *Introductory notions* from the *Original (published) scientific results*. Since most of the results produced during the doctorate were already published in refereed international scientific journals, or about to be accepted, we decided that this second part would consist in the inclusion of the publications produced by the applicant. There are several reasons behind this decision that, in our opinion, benefit all the parts that will 'interact' with this PhD thesis. On one hand, it gives more time to the applicant to focus on the introductory notions and on better understanding the basics related with the field they have been working on during the last years. On the other hand, it also easies the referee process as the original scientific results are written as they were originally published, instead of repeating the same information with other words. And finally, it is also useful for future readers of this thesis, as they can clearly distinguish between what are the side results only produced for the thesis and what has been published in a refereed journal and therefore spread to the wide scientific community.

In the first three chapters of the thesis, comprising Part I, we first give (Chapter 1) a brief introduction to the research field and then, in Chapters 2 and 3 we try to derive and understand the basic expressions that form the well-stablished basics of GW data analysis, at the same time that justify the scientific studies that are presented in Part II. Of course, all the results derived in Part I can be found in many other publications, and for this reason they would never be accepted in a refereed journal; however, we consider that the knowledge acquired from deriving all the expressions from scratch and using a uniform notation can be extremely useful for the applicant in his future scientific career and we wish that also this material could be useful for future students entering this field.

The scientific results presented in this thesis (Part II) can be divided into three different research lines (see Tab. 9.1 for a summary), all of them related to data analysis studies of gravitational waves emitted by compact binary objects. Our main conclusions are summarized in Chapter 9.

- First, we perform parameter estimation studies (Chapter 4) of supermassive binary black hole inspirals observed with LISA (the future gravitational wave space antenna) using post-Newtonian waveforms that include all the harmonics and we compare the output with the classical results where only the dominant ($\ell = 2, m = \pm 2$) was present. Then, we also study what are the consequences of this improvement on the

science that LISA will be able to do, in particular, we study what is the expected number of SMBH sources that LISA will observe with a particular error and also, the precision on the estimation of the dark energy equation of state (Chapter 5)

- Second, we develop a search method for galactic binary signals with LISA based on Bayesian probability and Markov chain Monte Carlo techniques and apply it to a number of simulated data sets containing one or several overlapping signals (Chapter 6). On the way, we shall face the problem of efficiently sampling a multimodal distribution, and the solution we propose in Chapter 7 is a completely Markovian and fully general algorithm, based on a technique called Delayed Rejection, that we successfully implement for the search of galactic binaries with LISA. We belief that this general method can be applied to a number of problems in a variety of fields.

- Finally, we study the accuracy and effectualness of some model waveforms used in searches for compact binary coalescences with ground-based interferometric detectors. In particular, we study the validity range of the fastest (but also approximated) waveform models either when they are used just for detection, or also for measurement purposes (Chapter 8).

As it is usual within the scientific community working on GR problems, in most of the situations we will use so-called *geometrized units* in which $c \equiv 1 \left[1 \text{ s} = \tilde{c} \text{ m} \simeq 3 \times 10^8 \text{ m}\right]$ and $G \equiv 1 \left[1 \text{ s} = \dfrac{\tilde{c}^3}{\tilde{G}} \text{ kg} \simeq 4 \times 10^{35} \text{ kg}\right]$, so we shall be effectively measuring length and mass in units of *time*. Working with astrophysical problems, some significant relation to have in mind are the following,

$$10^6 M_\odot = 4.93 \text{ s} \qquad ; \qquad 1 \text{ AU} = 499 \text{ s} \qquad ; \qquad 1 \text{ Gpc} = 1.03 \times 10^{17} \text{ s}$$

We also would like to take this opportunity to define some very common quantities that appear throughout all the thesis and that sometimes it is useful to have all of them defined in the same place.

- Total mass: $M \equiv m_1 + m_2$;

- Mass difference: $\delta m \equiv m_2 - m_1$;

- Reduced mass: $\mu \equiv \dfrac{m_1 \cdot m_2}{m_1 + m_2}$;

- Symmetric mass ratio: $\nu \equiv \dfrac{\mu}{M} = \dfrac{m_1 \cdot m_2}{(m_1 + m_2)^2}$ [sometimes designated by η];

- Chirp mass: $\mathcal{M} \equiv M\nu^{3/5}$;

- Characteristic velocity of a CBC inspiral: $\text{v} \equiv (\pi f M)^{1/3}$;

- Post-Newtonian expansion parameter: $x = (\pi f M)^{2/3} = \text{v}^2$;

- Characteristic velocity at the (test-mass particle) last stable orbit: $\text{v}_{\text{LSO}} = 1/\sqrt{6}$.

Part I

Introductory notions

Chapter 1

Introduction

According to Einstein's theory of general relativity (GR), compact concentrations of energy [*e.g.* neutron stars (NSs) and black holes (BHs)] should wrap spacetime strongly, and whenever such an energy concentration changes shape, it should create a dynamically changing spacetime warpage that propagates out through the Universe at the speed of light. This propagating warpage is called a *gravitational wave* — a name, that arises from GR's description of gravity as a consequence of spacetime warpage.

Although gravitational waves (GWs) have not yet been detected directly, their first indirect evidence was found in the observed inspiral of the binary pulsar PSR 1913+16, discovered by Hulse and Taylor [1]. Taylor (and colleagues) demonstrated [2, 3] that the observed NSs are spiraling together at just the rate predicted by GR's theory of gravitational radiation reaction; the computed and observed inspiral rates agree to within the experimental accuracy, which is better than one per cent. In 1993, the Nobel Prize in physics was awarded to Hulse and Taylor for their discovery. This is a great triumph for Einstein's theory, however it is not a firm proof that GR is correct in all aspects. Other relativistic theories of gravity (*i.e.* compatible with special relativity) also predict the existence of GWs; and some of them predict the same inspiral rate for PSR 1913+16 as GR, to within the experimental accuracy [4, 5].

The emission of detectable GWs is related to catastrophic, high-energetic events in the Universe, such as supernovae explosions, compact binary coalescences (CBCs), rapidly spinning NSs or even the Big Bang. Some of these events have already been observed through their electromagnetic emission; although if we compare the energy emitted as GWs to the electromagnetic counter-part, it turns out that the gravitational radiation luminosity is many order of magnitudes larger. The reason behind is because spacetime is a very "stiff" medium, *i.e. large amounts of energy are carried by GWs of small amplitude.* This fact can be easily seen, for instance, considering one among the most promising sources for GW detectors [it is also the source considered in all the studies of this thesis], which is the (similar mass) compact binary coalescences (CBCs), including from stellar-mass compact systems (NSs and BHs), up to supermassive black holes (SMBHs). Within the Newtonian approximation, the GW luminosity (or "flux"), $\mathcal{F}_{\mathrm{GW}}$, and amplitude, a_{GW}, can

be written as [6]

$$\mathcal{F}_{\mathrm{GW,\,N}} = \frac{32c^5}{5G}\nu^2 \mathrm{v}^{10} \qquad \text{and} \qquad |a_{\mathrm{GW,\,N}}| = 4\frac{\nu M}{D_L}\mathrm{v}^2 \,, \tag{1.1}$$

where G and c are the gravitational constant and speed of light, respectively[1]; $M = m_1 + m_2$ is the total mass of the system, $\nu = \frac{m_1 m_2}{M^2}$ is the symmetric mass ratio, D_L is the luminosity distance to the source and $\mathrm{v} = (\pi f M)^{1/3}$ is a characteristic speed of the two orbiting objects. Taking a typical equal-mass ($\nu = 1/4$) BH-BH coalescence ($M = 20M_\odot$) within the Virgo supercluster ($D_L = 30$ Mpc) at its last stable orbit, LSO ($\mathrm{v}_{\mathrm{LSO}} = 6^{-1/2}$), we obtain a GW luminosity $\mathcal{F}_{\mathrm{GW,\,N}} \simeq 2 \times 10^{48}$ W $\simeq 5 \times 10^{21} L_\odot$, whereas the GW amplitude (which directly represents the relative length changes induced by the GW) is $|a_{\mathrm{GW,\,N}}| = 2\frac{|\Delta L|}{L} \simeq 5 \times 10^{-21}$. These are typical values for the expected GW sources and they explain why we have been able to indirectly measure the effect of gravitational radiation in terms of energy losses, but it is so hard to directly observe them. Notice from Eq. (1.1) that the GW luminosity of a CBC at the last stable orbit (LSO) is independent of the total mass, *i.e.* the power emitted by two stellar-mass BHs is the same as a $10^7 M_\odot - 10^7 M_\odot$ system; what is different is the amount of time that such luminosity is held (the time scales of massive systems are much longer).

Recent years have seen a shift in the technologies used in GW searches, as the first generation of large GW interferometers has begun operation at, or near, their design sensitivities, taking up the baton from the bar detectors that pioneered the search for the first direct detection of GWs. In particular, an international network of ground-based multi-kilometer scale interferometers is currently operating and fundings are already approved to built an advanced generation of the current interferometers, which should provide an order of magnitude improvement in their sensitivity.

The direct detection of GWs will represent a confirmation of the GR's predictions, but more importantly, it will open the exciting new field of GW astronomy which will provide answers to a number of questions in various different areas [7]. In particular, we expect to get answers to questions for

- *Fundamental Physics and General Relativity*: What are the properties of GWs? Is GR the correct theory of gravity, and is it still valid under strong-gravity conditions? How does matter behave under extremes of density and pressure?

- *Astronomy and Astrophysics*: How abundant are stellar-mass BHs? What is the central engine behind gamma-ray bursts? Do intermediate mass BHs exist? Where and when do massive BHs form and how are the connected to the formation of galaxies? How massive can a NS be and how is their interior? What is the history of star formation rate in the Universe?

- *Cosmology*: What is the history of the accelerating expansion of the Universe? Were there phase transitions in the early Universe?

---

[1]In most situations throughout this thesis, we shall use so-called geometrized units in which $G = c = 1$; however, here they are written explicitly in order to be able to compute quantities in SI units.

1.1 Gravitational waves

GWs are oscillations of the spacetime propagating away from the source that generated them as waves at the speed of light. There is an enormous difference [8] between GWs, and the electromagnetic (EM) waves on which our present knowledge of the Universe is based, and indeed are these differences what make the information brought to us by GWs to be very different from (almost "orthogonal to") that carried by EM waves, *i.e.* it is usually said that GW astronomy will be a completely new window to observe the Universe through.

- EM waves are oscillations of the EM field that propagate through spacetime; whereas GWs are oscillations of the "fabric" of spacetime itself.

- GWs are produced by coherent, bulk motions of huge amounts of mass/energy and the wavelengths are comparable to, or larger than, the emitting sources; kilometric ground-based detectors will observe GW signals within the $\lambda \in [10, 10^5]$ km range, whereas the 5×10^6 km long future space antenna will have the observable range within $\lambda \in [10^6, 10^9]$ km; which, in both cases, correspond to the typical size of the sources. On the other hand, EM waves are almost always incoherent superpositions of emission from individual electrons, atoms or molecules, with much smaller emission wavelengths.

- EM waves are easily absorbed, scattered, and dispersed by matter. Despite the huge amount of energy carried by GWs, they almost do not interact with matter, this is why it is so hard to detect them, but at the same time this also means that the information from the emitting source is preserved almost unaltered.

1.1.1 Einstein's equations for a weak gravitational field

The existence of GWs was a prediction of theory of GR, and from it one can derive the main (general) properties that characterize them. As an introductory chapter, here we just present a brief derivation of the main properties of GWs, which are covered in much greater depth in Refs. [8–12]; this section has been written mainly following Ref. [13].

We shall start by considering a GW as a 'weak' perturbation of a flat spacetime, which can be expressed mathematically as

$$g_{\alpha\beta} = \eta_{\alpha\beta} + h_{\alpha\beta} \, , \tag{1.2}$$

where $\eta_{\alpha\beta} = diag(-1, 1, 1, 1)$ is the Minkowski metric of Special Relativity and $|h_{\alpha\beta}| \ll 1$ for all α and β. The coordinate system in which the metric components of a 'nearly' flat spacetime can be written as in Eq.(1.2) is not unique. Actually, once it has been identified a coordinates system in which the metric components can be written in such way, it is possible to find an infinite family of other coordinates systems that also have the metric components written as Eq. (1.2); for instance, the Lorentz and *gauge* transformations are two changes of coordinates that preserve such general expression. Then, it is possible to demonstrate[2] that in a free space (*i.e.* $T_{\mu\nu} = 0$) and making the appropriated coordinate

---

[2]Since this is an introductory chapter, we shall not go through all the details needed to finally obtain the wave equation for $h_{\alpha\beta}$. See Refs. [9, 10] for further details.

transformations, Einstein's equations for the propagation of a metric perturbation can be written as $\Box \, \bar{h}_{\mu\nu} = 0$, or in other words,

$$\left(-\frac{\partial^2}{\partial t^2} + \nabla^2 \right) \bar{h}_{\mu\nu} = 0 \ . \tag{1.3}$$

This Equation (1.3) is nothing but a waves equation with a propagation velocity equal to $1 \equiv c$, *i.e.* it is found that the metric perturbations propagate at the speed of light through free space.

1.1.2   Independent components of $h_{\mu\nu}$

The simplest solution to Eq. (1.3) is a superposition of plane waves, that can be written as

$$\bar{h}_{\mu\nu} = Re \left[A_{\mu\nu} \exp(ik_\alpha x^\alpha) \right] \ , \tag{1.4}$$

where the constant components $A_{\mu\nu}$ and k_α are known as the *wave amplitude* and *wave vector* respectively. These two quantities are not arbitrary; instead, they must satisfy some conditions that shall reduce the number of independent components from 16 to only 2:

- $A_{\mu\nu}$ is symmetric, since $\bar{h}_{\mu\nu}$ is symmetric; this immediately reduces the number of independent components from 16 to 10. Also, it is easy to show that the wave vector, k_α, is a *null vector*.

- From the Lorentz gauge condition [which has been applied to obtain Eq. (1.3)], it can also be seen that the wave amplitude components must be orthogonal to the wave vector: $A_{\mu\alpha}k^\alpha = 0$, reducing the number of independent components from 10 to 6.

- It can be shown [9, 10] that the choice of coordinates that satisfy the Lorentz gauge is not unique. This provides the freedom to choose a coordinates system in which $\bar{h}_{\mu\nu}$, and therefore $A_{\mu\nu}$, can be written in an even more simplified way. In particular, we shall work with the *transverse-traceless gauge*[3] (TT), where four more amplitude components are fixed, leaving only 2 independent components.

Hence, after all these considerations and arbitrarily setting the propagation direction of the GW to be parallel to the z-axis, we have that

$$\bar{h}_{\mu\nu}^{(\mathrm{TT})} = A_{\mu\nu}^{(\mathrm{TT})} \cos\left[\omega(t - z)\right] \ , \tag{1.5}$$

where only two amplitude components are independent

$$A_{\mu\nu}^{(\mathrm{TT})} = \begin{pmatrix} 0 & 0 & 0 & 0 \\ 0 & A_{xx}^{(\mathrm{TT})} & A_{xy}^{(\mathrm{TT})} & 0 \\ 0 & A_{xy}^{(\mathrm{TT})} & -A_{xx}^{(\mathrm{TT})} & 0 \\ 0 & 0 & 0 & 0 \end{pmatrix} \ . \tag{1.6}$$

---

[3]With this choice of coordinates, one finds that the trace of $A_{\mu\nu}$ is null, besides that their components are perpendicular to the wave's propagation direction (*i.e.* it is a transverse wave).
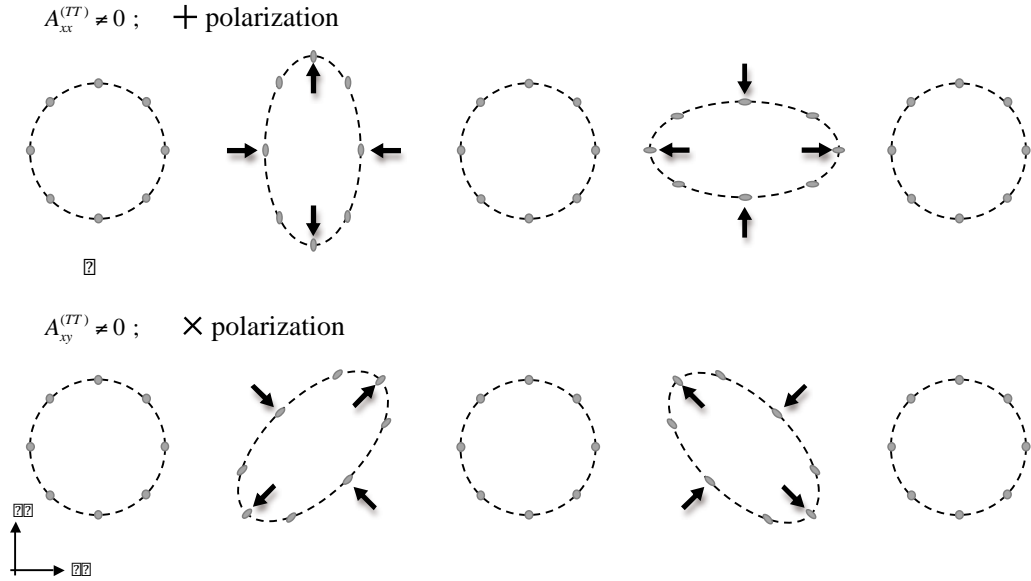
Figure 1.1: Cartoon of the effects that the two independent polarizations of a GW traveling in the direction perpendicular to the paper sheet produce over an annular distribution of mass. The top panel is obtained by setting $A_{xx}^{(\mathrm{TT})} \neq 0$; $A_{xy}^{(\mathrm{TT})} = 0$ and it corresponds to the '+' *polarization*; whereas in the bottom panel, we are setting $A_{xx}^{(\mathrm{TT})} = 0$; $A_{xy}^{(\mathrm{TT})} \neq 0$, getting the '×' *polarization*. [Diagrams: own production based on [13]]

1.1.3 Effect of gravitational waves on free particles

We have just obtained a solution to Einstein's equations for a metric perturbation propagating in free space. Now, we want to understand the effect that a GW produces when it passes through matter and hence, to understand the significance of the two independent amplitude components, $A_{xx}^{(\mathrm{TT})}$ and $A_{xy}^{(\mathrm{TT})}$, obtained in Eq. (1.5).

A free particle initially at rest, will remain at rest indefinitely. However, 'being at rest' in this context simply means that the *coordinates* of the particle do *not* change when a GW passes through. What will manifest the effect of the gravitational radiation is the change in the proper distance between two free particles. Hence, *the effect of GWs is to modify the proper distance between two free masses*, and indeed the relative length change is directly related to the perturbation's amplitude, $\frac{\Delta L}{L} = \frac{h}{2}$. It is essentially this change in the proper distance between test particles what GW detectors attempt to measure.

Suppose a GW that passes through a ring of test particles and first assume that $A_{xx}^{(\mathrm{TT})} \neq 0$; $A_{xy}^{(\mathrm{TT})} = 0$, and then assume the opposite case; with this, we shall be able to see the effect of each of the independent amplitude components of the wave. In Fig. 1.1 we can observe the time evolution of the system in each case, the former usually known as '+' *polarization* and the latter as '×' *polarization*. Hence, in general any GW propagating along the z-axis can be expressed as a linear combination of two independent polarization states,

$$\mathbf{h} = h_+\mathbf{e}_+ + h_\times\mathbf{e}_\times \ , \tag{1.7}$$

where h_+ and $h_\times$ are the two independent components of the GW, and $\mathbf{e}_+$ and $\mathbf{e}_\times$ are the

polarization tensors

$$\mathbf{e}_+ \equiv \begin{pmatrix} 0 & 0 & 0 & 0 \\ 0 & 1 & 0 & 0 \\ 0 & 0 & -1 & 0 \\ 0 & 0 & 0 & 0 \end{pmatrix} \quad ; \quad \mathbf{e}_\times \equiv \begin{pmatrix} 0 & 0 & 0 & 0 \\ 0 & 0 & 1 & 0 \\ 0 & 1 & 0 & 0 \\ 0 & 0 & 0 & 0 \end{pmatrix} . \tag{1.8}$$

We can see from the panels in Fig. 1.1 that the distortion produced by a gravitational wave is *quadrupolar*. Moreover, at any instant, a GW is invariant under a rotation of 180° about its direction of propagation[4] and the two independent polarization states can be seen as inclined 45° with respect each other. Putting all pieces together[5] is consistent with the fact that a hypothetical *graviton* particle (which it is, as yet undiscovered, since we do not have a fully developed theory of quantum gravity) must be a spin $S = 2$ particle.

1.1.4   Production of gravitational waves

In order to study the *propagation* of GWs in the vacuum, we have made use of the weak field approximation, besides assuming the energy momentum tensor to be null; and under these assumptions we have been able to find an analytical expression for the propagation of a metric perturbation. Difficulties appear when one is interested in studying the *production* of GWs, since now one has to describe the metric close to the compact source, where the weak field approximation is not valid. In the best scenario, it will not be necessary to solve the full Einstein's equations, instead it could be enough by making post-Newtonian (PN) approximations; however, in a number of problems one will have to solve Einstein's equations numerically.

A crude estimation of orders of magnitude and dominant contributions to the luminosity emitted by a source as gravitational radiation, can be done [13] by drawing analogies with the formulae that describe electromagnetic radiation in terms of the multipolar expansion, but replacing $e^2 \leftrightarrow -m^2$, in order to go from electrostatic's Coulomb force to Newton's law[6].

- In electromagnetic theory, the dominant form of radiation from a moving charge is the *electric dipole radiation*, whose luminosity (or "flux") is given by

$$\mathcal{F}_{electric\ dipole} = (2/3)\ \ddot{\mathbf{d}}^2 \ ,$$

  where $\mathbf{d}$ is the dipole moment and the *dots* denote time derivatives. The gravitational analogue of the electric dipole moment is the mass dipole moment, summed over a distribution of particles, $\{A_i\}$

$$\mathbf{d} = \sum_A m_A \mathbf{x}_A \ .$$

---

[4]By contrast, an electromagnetic wave is invariant under a rotation of 360°, and a *neutrino* wave is invariant under a rotation of 720°.

[5]In general, the classical radiation field of a particle of spin, S, is invariant under a rotation of $360°/S$, besides that the different polarization states are inclined to each other at an angle of $90°/S$.

[6]This procedure treats gravity as vectorial field instead of a tensorial fields, but it is good enough for our present purposes.

Now, we realize that the first derivative of the mass dipole moment is the total linear momentum of the system, $\dot{\mathbf{d}} = \mathbf{p}$. Since the linear momentum is conserved, it follows that there can be no mass dipole radiation from any source.

- The next strongest types of electromagnetic radiation are *magnetic dipole* and *electric quadrupole radiation*. The magnetic dipole radiation is proportional to the second time derivative of the magnetic dipole, $\ddot{\boldsymbol{\mu}}$. As before, its gravitational analogue also corresponds to a preserved quantity, in this case the total angular momentum

$$\boldsymbol{\mu} = \sum_{\mathrm{A}} \mathbf{r}_{\mathrm{A}} \times (m\mathbf{v}_{\mathrm{A}}) = \mathbf{J} \, ,$$

hence, there is no radiation either; in other words, *there can be no dipole radiation of any sort from a gravitational source.*

- In order to find the first not null contribution to gravitational radiation, one must consider the *quadrupole term*. The emitted luminosity predicted by electromagnetism is

$$\mathcal{F}_{electric\ quadrupole} \;\;=\;\; \frac{1}{20}\dddot{Q}_{jk}\dddot{Q}_{jk} \, ,$$

$$Q_{jk} \;\;\equiv\;\; \sum_{\mathrm{A}} e_{\mathrm{A}} \left(x_{\mathrm{A}j} x_{\mathrm{A}k} - \frac{1}{3}\delta_{jk}r_{\mathrm{A}}^2 \right) \, .$$

And the gravitational analogue,

$$\mathcal{F}_{mass\ quadrupole} = \frac{1}{5} \left\langle \dddot{\mathcal{J}}_{jk}^{(TT)} \dddot{\mathcal{J}}_{jk}^{(TT)} \right\rangle \, , \tag{1.9}$$

$$\mathcal{J}_{jk}^{(TT)} \equiv \sum_{\mathrm{A}} m_{\mathrm{A}} \left(x_{\mathrm{A}j} x_{\mathrm{A}k} - \frac{1}{3}\delta_{jk}r_{\mathrm{A}}^2 \right) = \int \rho \left(x_j x_k - \frac{1}{3}\delta_{jk}r^2 \right) \mathrm{d}^3 x \, , \tag{1.10}$$

where $\mathcal{J}_{jk}^{(TT)}$ is known as the *reduced* quadrupole moment, the factor $1/5$ that appears instead of the $1/20$ is due to the tensorial nature of the gravitational field and "$\langle \cdot \rangle$" denotes the average over several periods of the source.

We see from these results that a perfectly axisymmetric object rotating around its symmetry axis will *not* emit GWs, as its quadrupole moment is constant in time. Only objects with some sort of axial asymmetry (even if it is small) will produce gravitational radiation. This means that not all the objects in the Universe are candidates to be GW sources, only *stellar-core collapses, CBCs, rapidly spinning NSs, the Big Bang...* (see Fig. 1.2). We shall discuss more about astronomical GW sources in Sec. 1.2.

1.2 Astronomical gravitational wave sources

From the wide variety of objects that we find in the Universe, it will be good candidates only those ones being compact, rapidly moving and presenting some sort of axial asymmetry (see Sec. 1.1.4). This provides a wide range of possible sources, from NSs ($M \lesssim 2M_\odot$ and $R \sim R_T$) with very short orbital periods, up to galaxy mergers or even the Big Bang. In order to estimate the emission frequency of such objects, we can assume

HIGH FREQUENCY SOURCES (GROUND-BASED DETECTORS)

Stellar core collapses   Stellar-mass binary
(SNs, newborn BH/NS)   Pulsars   coalescences   Stochastic background

LOW FREQUENCY SOURCES (SPACE-BASED DETECTORS)

                                                          Supermassive black
Galactic binaries   EMRIs   hole coalescences   Stochastic background
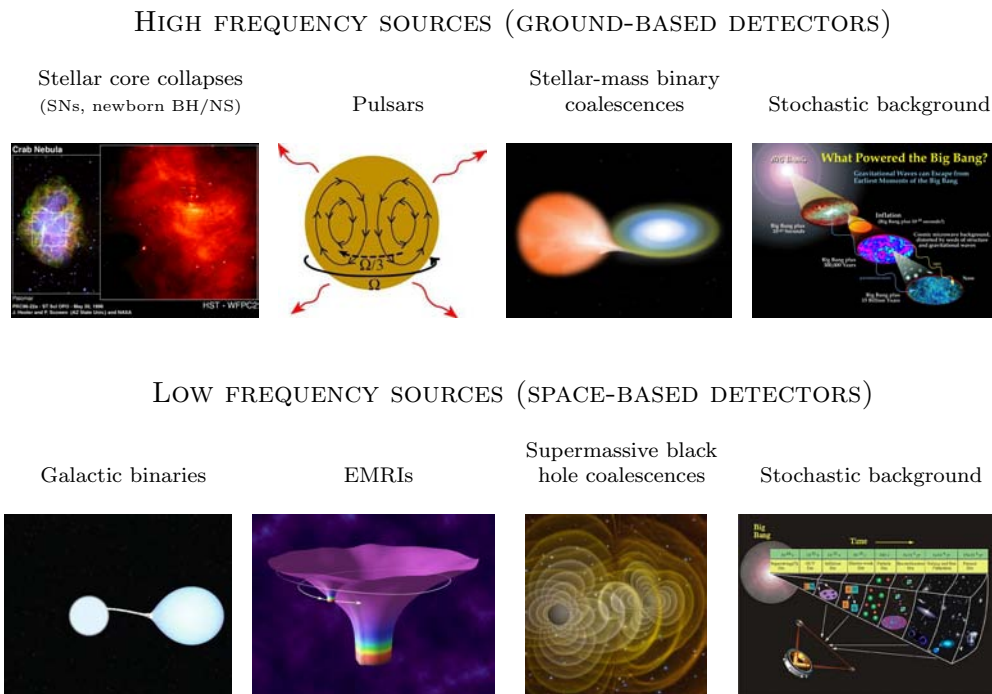
Figure 1.2: Artistic representation of some of the expected GW sources in the high and low frequency bands. [Images: various sources]

that a gravitational-wave (compact) source of mass M cannot be much smaller than its gravitational radius, $2GM/c^2$, and cannot emit strongly at periods much smaller than the light-travel time $4\pi GM/c^3$ around this gravitational radius. Correspondingly, the frequencies at which it emits are [8]

$$f \lesssim \frac{1}{4\pi GM/c^3} \sim 10^4 \text{ Hz } \frac{M_\odot}{M} \ . \tag{1.11}$$

To achieve a size of order its gravitational radius and thereby emit near this maximum frequency, an object presumably must be heavier than the Chandrasekhar limit, *i.e.* $M \gtrsim 1.44 M_\odot$. Thus, the highest frequency expected for strong GWs is $f_{\max} \sim 10^4$ Hz. This define the upper edge of the high-frequency GW band, which spans up to frequencies 20 orders of magnitude smaller than $f_{\max}$. So, this results into a very wide frequency range, that is usually divided into different bands depending on the kind of sources and detection methods used in each case. For instance, Ref. [8] distinguish between the *high-frequency band* ($f \sim 10^4 - 1$ Hz), the *low-frequency band* ($f \sim 1 - 10^{-4}$ Hz), the *very-low-frequency band* ($f \sim 10^{-7} - 10^{-9}$ Hz) and the *extremely-low-frequency band* ($f \sim 10^{-15} - 10^{-18}$ Hz). In Fig. 1.2 it is shown some of the expected sources in the high-frequency and low-frequency bands.

High-Frequency band, $1 - 10^4$ Hz

The high-frequency band is the domain of Earth-based GW detectors: laser interferometers and resonant mass antennas. At frequencies below about 1 Hz, the noise produced either by fluctuating Newtonian gravity gradients (*e.g.* due to inhomogeneities in the Earth's atmosphere which move overhead with the wind) or by Earth seismic vibrations (which

are extremely difficult to filter our mechanically below $\sim$ Hz) become very important. In order to detect waves below this frequency, one must fly the detectors into space.

A number of interesting GW sources fall in the high-frequency band, mainly objects with masses similar to the Sun:

- the stellar collapse to a NS or BH in our Galaxy (or galaxies nearby). Sometimes, they trigger supernovae, in which case one could also observe their electromagnetic counter-parts;

- the rotation and vibration of NSs (pulsars) in our Galaxy;

- the coalescence of NSs and stellar-mass BHs (*i.e.* $M < 1000 M_\odot$) binaries in distant galaxies;

- stochastic background generated by vibrating loops of cosmic strings, phase transitions in the early Universe, or even the Big Bang.

Low-Frequency band, $10^{-4} - 1$ Hz

The low-frequency band is the domain of the detectors flown in space, either in Earth orbit or in interplanetary orbit. In the 1970s, NASA tried to measure the GW effects by Doppler tracking a spacecraft via microwave signals sent from Earth to the spacecraft and there transponded back to Earth, although they did not success. Currently, a joint NASA/ESA project is under development in order to send the Laser Interferometer Space Antenna (LISA) into space over the next decade (2020+). As we shall see, LISA will be able to observe a wide variety of sources, some of them located at very high redshifts. Many of the studies performed during this thesis are related to LISA observations.

The $\sim 10^{-4}$ Hz lower edge of this frequency band is defined by expected severe difficulties at lower frequencies in isolating the spacecraft from the buffeting forces of fluctuating solar radiation pressure, solar wind and cosmic rays.

The low-frequency band should be populated by GWs from

- short-period binary stars in our own Galaxy, such as main-sequence stars, white-dwarfs, NSs...;

- white dwarfs, NSs and small BHs inspiraling into massive BHs ($M \sim 3 \times 10^5 - 3 \times 10^7 M_\odot$), so-called extreme mass ratio inspirals (EMRIs), in distant galaxies;

- SMBHs coalescences ($M \sim 10^5 - 10^9 M_\odot$);

- it is also expected to observe a low-frequency component of the stochastic background radiation generated in the early Universe.

Very-Low-Frequency band, $10^{-9} - 10^{-7}$ Hz

In order to detect such very-low-frequency signals, it would be necessary to build detectors larger than the Solar System, what makes to think in different detection techniques. In

particular, Joseph Taylor and others suggested to accurately measure the evolution of the emitting period of several known pulsars located in our own Galaxy over several decades: the idea behind is that when a GW passes over the Earth, it perturbs our rate of flow of time and thence the ticking rates of our clocks relative to the clocks outside the wave. The deviations between the predicted and the observed time of arrivals (TOAs) are known as the pulsar 'timing residuals' and indicate unmodelled effects. In particular, GW signals are not included in the pulsar timing model, hence, if these residuals are seen simultaneously in the timing of several different pulsars, then the cause could well be GWs bathing the Earth.

Unfortunately, the expected signal induced by GWs is small, with typical residuals being < 100 ns. The TOA precision achievable for the majority of pulsars is ~ 1 ms and most pulsars show long-term timing irregularities that would make the detection of the expected GW signal difficult or impossible [14]. However, a sub-set of the pulsar population, the *millisecond pulsars*, have very high spin rates, much smaller timing irregularities and can be observed with much greater TOA precision (~ 30 ns).

The recently created International Pulsar Timing Array project [15] combines observations of millisecond pulsars from both northern and southern hemisphere observatories with the main aim of detecting GWs in this very-low-frequency band. Given the current theoretical models, it is likely that these GWs will be detected by pulsar timing experiments within $5-10$ years. The first detections are expected to be of an isotropic, stochastic GW background created by coalescing SMBH systems [16, 17].

Extremely-Low-Frequency band, $10^{-18} - 10^{-15}$ Hz

GWs in the extremely-low-frequency band should produce anisotropies in the cosmic microwave background radiation. Thus, these GW signals could be (indirectly) detected by studying the cosmic microwave background radiation maps obtained with missions like COBE[7], WMAP[8] and the on-going PLANCK[9].

1.3   Direct detection of gravitational waves (from High- and Low-Frequency bands)

It is now 50 years since J. Weber initiated his pioneering development of GW detectors [18] and 40 years since R. Forward [19] and R. Weiss [20] initiated work on interferometric detectors. Since then, hundreds of experimental physicists have worked to improve the sensitivities of these instruments, at the same time that theoretical physicists have explored in detail which GR predictions will be able to be tested with these detectors. The current sensitivities achieved by the interferometric detectors, place GW science on the verge of direct observation of the waves predicted by Einstein's theory of GR and opening the exciting new field of GW astronomy. It is hoped that the first direct observation of GWs will be made in the next few years.

---

[7]`http://lambda.gsfc.nasa.gov/product/cobe/`
[8]`http://wmap.gsfc.nasa.gov/`
[9]`www.esa.int/planck/`

The aim of this section is to give a very brief introduction to the most relevant properties of the two most important kind of GW detectors built up to now (*cryogenic resonant-mass detectors* and *interferometric detectors*, these last ones both ground- and space-based), which are their main noise sources, what are their current sensitivities, future plans. . .

1.3.1   Cryogenic resonant-mass detectors

Following J. Weber's efforts in the 1960s and after many years of investigations, in 1986 three cryogenic antennas in Stanford, Baton Rouge (ALLEGRO) and at CERN in Geneva (EXPLORER, built by the University of Rome) operated in coincidence for three months; and for increasingly longer periods in the following years. Unfortunately, the Stanford group withdrew from the field, after the untimely death of W. Fairbanks and as a consequence of the damage of their detector during the earthquake of 17 October 1989. However, two other groups joined the search, the University of Perth in Australia (NIOBI) and the University of Padova in Italy (AURIGA); and the Rome group designed and assembled a new generation of resonant detector (NAUTILUS) that used a ^{3}He $-$ ^{4}He dilution refrigerator to cool down the 2500 kg aluminum bar to 0.1 K. Thus, in the 1990s and up to 2006, there was five such resonant-mass instruments around the world [21] working in cooperation in the so-called, IGEC[10] (International Gravitational Event Collaboration). Currently, both AURIGA and NAUTILUS antennas are still in operation, permanently on watch in case a supernovae event in our galaxy is detected, covering with their observations the periods when all other gravitational wave antennas on the world are offline.

A resonant-mass detector (colloquially known as *bar*) consists of a solid body, usually a cylinder (though spheres are also being considered) of about 3 meters long and a few tons of weight that vibrates "considerably" when a GW with a frequency similar to its resonance passes through. The resonant mass is typically made from an alloy of aluminum, but some have been made of niobium or single-crystal silicon or sapphire. To control thermal noise, all the resonant-mass detectors are cryogenically cooled down to temperatures, $T \sim 0.1-6$ K, depending on the detector. For instance, the ultra-cryogenic detector NAUTILUS showed a capability of reaching a temperature as low as 0.1 K being equipped with a ^{3}He $-$ ^{4}He dilution refrigerator [22].

In comparison to the interferometric detectors, current resonant-mass detectors are characterized to be sensitive in a narrow frequency band (a bandwidth of about 30 Hz) in the uppermost reaches of the high frequency band $\sim 10^3$ to 10^4 Hz, where photon shot noise debilitates the performance of interferometric detectors. Thus, resonant-mass detectors have observational frequency windows complementary to the interferometric GW detectors. Current detectors present spectral strain sensitivities of $\tilde{h} \sim 3 \times 10^{-21}$ Hz$^{-1/2}$, which corresponds to a conventional (1 ms) amplitude of GW bursts $h \sim 4 \times 10^{-19}$.

Future detectors may reach sensitivities up to $h \sim 10^{-21}$, which corresponds to the quantum limit directly obtained from the Heisenberg uncertainty principle. This lower limit in the sensitivity of the resonant-mass detectors is what propitiated, already 30 years ago, that most of the efforts in designing and building GW detectors were put on the interferometers, which have this lower bound much below. Anyway, resonant-mass detectors have their importance even in the LIGO/Virgo era, since they provide the opportunity to

---

[10]`http://igec.lnl.infn.it`

Figure 1.3: Basic diagram of an interferometric detector: four masses (*test masses*) isolated from external vibrations, two of them located close together in the vertex of the 'L' shaped structure and the other two at the end of each of the interferometer's arms. By studying via interferometry techniques, the dephasing between the laser beams that have traveled along each of the arms, we can obtain precise measures of how the length difference between the two arms changes over time. In practice, these "masses" are mirrors with a reflectivity (for the frequency of the laser beam) close to 1. [Image: LIGO]
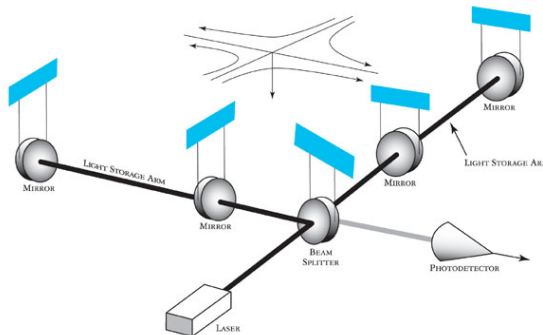
search for GW signals in very high frequency regions, where the interferometer detectors are not that sensitive.

1.3.2 Interferometric gravitational wave detectors

Given the quadrupolar nature of the gravitational waves (see Fig. 1.1), the best approach to directly detect such waves would be to monitor the time dependency of the length difference between two orthogonal directions. With this, since the relative length change produced by a GW in each direction is $\frac{\Delta L}{L} = \frac{h}{2}$; when the GW plane is aligned with the detector's plane, we will have $L_x = L + \Delta L$ and $L_y = L - \Delta L$, hence $\frac{\Delta L_{\mathrm{arms}}}{L} \equiv \frac{L_x - L_y}{L} = 2\frac{\Delta L}{L} = h$. Moreover, the longer the distance L we are measuring length differences over is, the higher the sensitivity in measuring GWs, for a fixed ΔL precision, will be.

These arguments made scientists think about the Michelson-Morley interferometer as the starting design to built alternative (to resonant-mass bars) and more sensitive GW detectors. The basic diagram of an interferometric (ground-based) detector consists in four masses (*test masses*) suspended as pendula using seismic isolation systems, distributed as it is shown in Fig. 1.3 and the corresponding optical system to monitor the separation between masses. Two masses are located very close together, in the vertex of the 'L' shaped structure, whereas the other two are at the end of each interferometer's arms[11]. In ground-based detectors, these "masses" are mirrors with an extremely high reflectivity and therefore they are already part of the optical system.

To measure the relative length difference of the arms, a single laser beam is split at the intersection of the two arms (*beam splitter mirror*). Half of the laser light is transmitted into one arm while the other half is reflected into the second arm. Laser light in each arm bounces back and forth between these mirrors (*test masses*) forming a Fabry-Perot cavity, and finally returns to the intersection, where it interferes with light from the other arm. If the lengths of both arms have remained unchanged, then the two combining light waves should completely subtract each other (destructively interfere) and there will be no light observed at the output of the detector (*photodetector*). However, if a GW were to slightly [assuming $h \sim 10^{-21}$ and $L = 4$ km, then $\Delta L \sim 2 \times 10^{-18}$ m $\sim 1/1000$ the diameter of a proton] stretch one arm and compress the other, the two light beams would no longer

---

[11]The arms of the interferometer do not have to be orthogonal, although this is the optimal configuration and indeed, the one used in all ground-based detectors. However, the future Laser Interferometer Space Antenna, for design reasons, will have $60°$ arms and it will consist in 6 free masses, instead of 4.

completely subtract each other, yielding light patterns at the detector output. Encoded in these light patterns is the information about the relative length change between the two arms, which in turn tells us about what produced the GWs.

Many things on Earth are constantly causing very small relative length changes in the arms of the interferometers. These every-present terrestrial signals are regarded as noise. The goal when designing a GW detector is to reduce this noise contributions to levels below the expected GW amplitudes and current technology is on the verge of reaching these levels.

- One of the most important parts in any ground-based GW detector are the *seismic isolation systems*. On one hand, there are tiny magnets attached to the back of each mirror, and the positions of these magnets are sensed by the shadows they cast from LED light sources. If the mirrors are moving too much, an electromagnet creates a countering magnetic field to push or pull the magnets and mirror back into position [this method is not only good for countering the motion of the mirrors due to local vibrations, but also to counter the tidal force of the Sun and the Moon]. Externally, there are very sophisticated hydraulic systems that filter out the Earth's surface vibrations.

- Also, all the optical components are placed inside a *vacuum*. On the superficial level this keeps air current from disturbing the mirrors, but mainly this is to ensure that the laser light will travel a straight path in the $\sim$ kilometer arms [notice that slight temperature differences across the arm would cause the light to bend due to temperature dependent index of refraction].

- First generation of detectors include an extra mirror between the laser source and the beam splitter, called *power recycling mirror*. Its purpose is to coherently re-inject the fraction of power that the detector is sending back to the laser source and that, otherwise would be wasted. With this, one gets more power into the detector's arms and reduces some of the noise contributions. Also, GEO-600 has been testing a *signal recycling mirror*, which has the same purpose as the former, but this one re-injects a fraction of the power sent to the photodetector. It is planned that Adv. LIGO is going to incorporate this extra mirror.

- A lot of development has also been done in the *laser technology*. The laser beam injected into the arms is previously frequency and amplitude stabilized [a changing laser frequency would add noise in the output of detector], and also they add some secondary modes necessary to lock the different Fabry-Perot cavities that are formed between the mirrors that compose the interferometer.

- Also, there are some on-going investigations towards building *cryogenic interferometric GW detectors*, *e.g.* the japanese Large Cryogenic Gravitational Telescope (LCGT)[12] or the european 3rd generation GW interferometer project, called Einstein Telescope (ET).

Current and future interferometric GW detector projects are (see also, Fig. 1.4):

---

[12]http://tamago.mtk.nao.ac.jp/spacetime/lcgt_e.html

| LIGO Hanford observatory | Einstein Telescope (ET) | LISA |
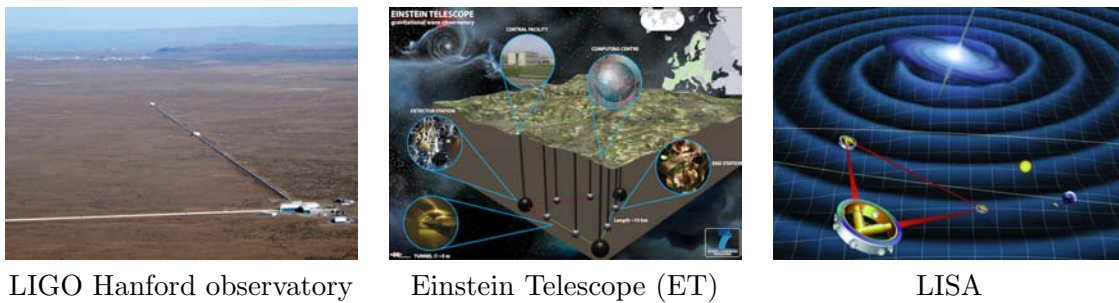
Figure 1.4: Pictures (or artistic representations) of some interferometric GW detectors. [Images: institutional web pages]

- The Laser Interferometer Gravitational-wave Observatory (LIGO) consists in three detectors, two colocated interferometers (with 2 km and 4 km arms, respectively) in Hanford (WA) and another 4 km detector in Livingston (LA). Currently they are the most sensitive GW detectors in the world and they were operating in science mode up to Oct. 2010, when it concluded the sixth science mode run, called 'S6'. Since that date, all scientists and engineers are working on the implementation of what will be the second generation of GW interferometric detectors, so-called Adv. LIGO. Some of the enhancements of this new generation (like the output mode cleaner and higher power mode) have been already tested during this very last science run, but now much greater updates are being implemented. Adv. LIGO is expected to be operational in about 4 years, with an improvement of almost an order of magnitude in sensitivity, *i.e.* a factor 1000 in observable volume.

- The Virgo detector is the result of a french-italian collaboration and consists in a 3 km interferometer located in Cascina (Italy). In general, the sensitivity of this detector is a little bit worse than LIGO; however it has a more sophisticated suspension system that provides better sensitivity at lower frequencies, where the inspiral signals from CBCs within the Virgo supercluster are located. During the last decade, the network LIGO-Virgo have been the most sensitive GW detectors in the world, and they have tried to collaborate and have 'science mode' time in coincidence. Indeed, some years ago the two scientific collaborations joined efforts creating the LIGO-Virgo Scientific Collaboration. As in LIGO, Virgo is currently being upgraded to Adv. Virgo; also an order of magnitude of improvement in sensitivity is expected from this second generation detector.

- GEO-600 is a 600 m detector built as a collaboration between the United Kingdom and Germany. The detector is located in Hannover (Germany) and, although it can not compete with LIGO or Virgo, it has been used as a test bank for the technology [mainly in collaboration with the LIGO Scientific Collaboration (LSC)] that, then, is going to be implemented in the next generation of detectors. For instance, GEO-600 has been running with a high power laser, output mode cleaner, signal recycling mirror, monolithic suspensions and electrostatic test mass actuators [23]; that now are planned to be installed in Adv. LIGO and Adv. Virgo. The future plans for this detector is to improve its sensitivity curve with further experimental upgrades in what will be GEO-HF, such as the tuned signal recycling and DC readout, the implementation of an output mode cleaner, the injection of squeezed vacuum into the anti-symmetric port, the reduction of the signal recycling mirror reflectivity and a power increase. In comparison with its contemporary detectors (Adv. LIGO and Adv.

Virgo), GEO-HF will be focused in improving its sensitivity in the high frequency range.

- TAMA-300 is a 300 m interferometric japanese project built in the city of Tokyo. For many years it was the most sensitive GW detector in the world, but now it is used just as a bank test for the extremely ambitious project of building an underground, cryogenic GW detector, the LCGT project.

- AIGO is an australian prototype for a GW detector. Currently, the most likely next step will be to build an exact replica of one of the LIGO interferometers in Australia. This is the cheapest solution and adding these new detector to the current network would significantly increase the network's sky resolution.

- Einstein Telescope (ET)[13] is the european project to build a third generation GW detector. GEO and Virgo members [and other european institutions] have joined efforts in designing what should be the new generation of GW interferometric detectors, possibly underground and using cryogenic techniques. Currently, ET is in its design phase, but it is receiving a lot of attention from all the european GW scientific community. Its design sensitivity should be an extra order of magnitude below the advanced detectors noise curves.

- The Laser Interferometer Space Antenna (LISA) is the most ambitious project to built an space-based interferometric GW detector to observe the Low-Frequency band. The technology needed for this project is so demanding, that the two most important space agencies, NASA and ESA, have joined their efforts to built LISA. It will consist in a constellation of 3 free-falling spacecrafts forming an equilateral triangle of 5×10^6 km long each edge, and following the Earth in its motion around the Sun, about 20° behind. The orbits have been designed in such a way that the triangle constellation will also rotate 360° around its center every time it completes an orbital cycle around the Sun (*i.e.* every year), by doing this, the detector obtains more angular resolution. Although the main working principle of LISA is the same as in the ground-based interferometers, the length of its arms (≈ 16.7 light-seconds), the fact that each spacecraft can have its own independent movement besides the effect of GWs and the impossibility of repairing anything once it has been launched into space, make LISA's design much more complicated. The expected launch date of LISA is in 2020+, although in order to test the feasibility of its technology a precursor mission fully managed and funded by European Space Agency (ESA), LISA Pathfinder, is being launched in 2012.

- As a follow-on mission to LISA, the Big Bang Observer (BBO) is proposed to NASA as a Beyond Einstein mission, targeted at detecting stochastic gravitational waves from the very early universe in the band 0.03 Hz to 3 Hz [7]. BBO will also be sensitive to the final year of binary compact body (NSs and stellar-mass BHs) inspirals out to $z < 8$, mergers of intermediate mass black holes at any redshift, rapidly rotating white dwarf, explosions from Type 1a supernovas at distances less than 1 Mpc and < 1 Hz pulsars.

- While BBO is seen as a successor to LISA in the US and Europe, the DECi-hertz Interferometer Gravitational wave Observatory (DECIGO) is the future Japanese space gravitational wave antenna [7]. The goal of DECIGO is to detect GWs from

---

[13]http://www.et-gw.eu/

various kinds of sources mainly between 0.1 Hz and 10 Hz. The current plan is
for DECIGO to be a factor 2-3 less sensitive than BBO, but for an earlier launch.
DECIGO can play a role of follow-up for LISA by observing inspiral sources that
have moved above the LISA band, and can also play a role of predictor for terrestrial
detectors by observing inspiral sources that have not yet moved into the terrestrial
detector band. In order to increase the technical feasibility of DECIGO before its
planned launch in 2024, the Japanese are planning to launch two milestone missions:
DECIGO pathfinder and pre-DECIGO.

An important difference of the GW detectors in comparison to standard electromagnetic
telescopes is that the former are *omnidirectional*, *i.e.* with a single strain time series $h(t)$,
we observe overlapped signals coming from any direction in the sky. The advantage is that
we are always making all-sky observations and therefore we will not miss any event because
of 'not pointing' at the right sky location. However, this also implies some disadvantages,
in particular, the sky resolution of GW detectors will be very poor compared to any
electromagnetic telescope; and also it can be a problem to observe too many overlapped
signals, which can even be indistinguishable becoming an extra source of noise (*e.g.* this
is case of galactic binaries with the LISA detector).

The angular resolution in GW detectors is basically given by three effects: *(i)* the *time-delay* in observing an event from distant locations (this implies having several detectors
working in coincidence); *(ii)* the *Doppler effect*[14] due to the relative motion of the detector
with the respect to the source and *(iii)* the *anisotropic sensitivity* of the GW detectors
(see, for instance, Fig. 2.2). Any of these effects require either long observation times so
that the velocity and orientation of the detector have substantially changed during the
observation, or the simultaneous observation of the same event with several detectors well
separated one from each other; a 'burst' signal observed by a single GW detector will imply
an unknown sky location. For these reasons, it has been built a network of ground-based
detectors located all over the world that work collaboratively in order to accumulate the
most coincidence observational time as possible. For the case of LISA, most of the expected
sources are long-lived sources in the LISA band and therefore, the yearly motion of the
detector around the Sun will provide a good sky resolution. For instance, in Fig. 1.5
we show the same inspiral signal from a $10^6 M_\odot - 10^7 M_\odot$ SMBH coalescence at different
locations, observed by LISA during the last year of inspiral phase; we see how the amplitude
modulations clearly allow one to localize long-lived GW signals. The Doppler shift, on the
other hand, can not be measured from signals in the Low-Frequency band since the typical
Doppler frequency shifts, $\Delta f = f\frac{v}{c}$, are smaller than the frequency resolution provided by
the observational time, $\delta f = 1/T_{\rm obs}$.

In comparison to the resonant-mass detectors, the interferometers are wide-band detectors.
In particular, the km-scale ground-based detectors will cover the High-Frequency band
$(1 - 10^4$ Hz$)$ of GW sources, whereas the space missions (such as LISA) will be observing
signals from the Low-Frequency band $(10^{-4} - 10^{-1}$ Hz$)$ of the GW spectrum. The ground-based detectors that have been in operation up to this date (first generation), have reached
spectral sensitivities[15] of $\sqrt{S_n} \sim 3 \times 10^{-23}$ Hz$^{-1/2}$, and if one considers the LIGO-Virgo
network, the expected detection rates for NS-NS systems is 0.02 yr^{-1} [24]. Currently, the

---

[14]Actually, given the frequency resolution and typical velocities of the detectors, only the signals in the
High-Frequency band will produce measurable frequency shits, since $\Delta f = f\frac{v}{c}$.
[15]See a proper definition of the noise power spectral density in Sec. 3.1.
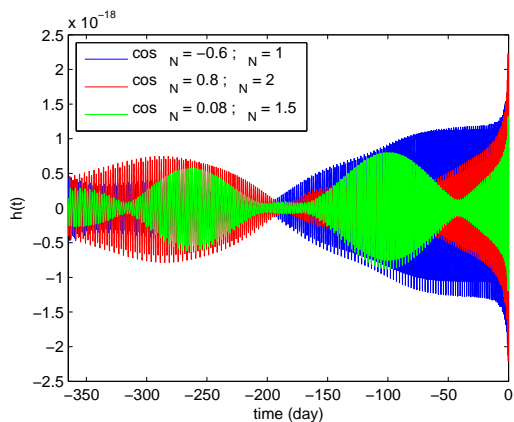
Figure 1.5: Time-domain waveforms observed by LISA from a SMBH binary system of $10^6 M_\odot - 10^7 M_\odot$ at redshift $z = 1$ during the last year of the inspiral phase before the last stable orbit (instant of time where we set $t = 0$). The three different curves represent the same source located at different position in the sky, which clearly shows the effect of the amplitude modulation in the observed signals due to the anisotropic sensitivity of the LISA detector. [Plot: own production]

new generation of ground-based detectors is being implemented and we expect them to be operational by 2015; the expected spectral sensitivities of such advanced detectors is $\sqrt{S_n} \sim 4 \times 10^{-24}$ Hz$^{-1/2}$ [24], *i.e.* a factor almost 10 of improvement in comparison with the first generation, which directly translates into a factor 10 of increase in the horizon distance and therefore a factor 10^3 in 'observable volume'. The (likely) expected events rates for the Advanced LIGO-Virgo network for the same NS-NS systems is 40 yr^{-1} [24]. Finally, let us say that a third generation of GW interferometric is current in the designing phase, and for instance, the expected sensitivity for ET is $\sqrt{S_n} \sim 3 \times 10^{-25}$ Hz$^{-1/2}$ [25].

1.4 Compact Binary Coalescences

Among the different potential sources for interferometric GW detectors, compact binary coalescences (CBCs) in the Universe are the most promising ones, both in terms of scientific results and detectability, given the wide range of masses and distances that can be observed. Ground-based detectors will observe NSs and stellar-mass BHs binary mergers (i.e.: the last phase of the coalescence) at any point of the Virgo Supercluster, including the Local Group and therefore the Milky Way. On the other hand, space-based detectors are sensitive to a lower frequency band and therefore will observe mergers of SMBHs (more than $10^5 M_\odot$) at any place in the Universe; besides tens of thousands of stellar-mass binaries located in our Galaxy that are in an early stage of their coalescing evolution, slowly inspiraling one around each other. See Sec. 3.5 for further details.

In order to detect all the signal-to-noise ratio (SNR) and to extract reliable physical information from GW observations, an accurate representation of the dynamics of the source and its emitted gravitational waveform is needed. The coalescence of a compact binary can be divided into three successive phases according to its dynamics: *(i)* an initial adiabatic *inspiral phase* where the emitted gravitational waveform is a chirping signal (i.e.: frequency and amplitude slowly increasing over time) that can be analytically described as a PN expansion; *(ii)* when the two objects are very close together, the velocities become relativistic, the energy emitted importantly increases and the process is not adiabatic anymore (*merger phase*); thus, full GR equations must be solved in order to provide a faithful representation of the dynamics; finally, after the merger, *(iii)* the resulting excited Kerr BH will settle down (*ring-down phase*) by emitting gravitational radiation analytically described as a superposition of quasi-normal modes.

It is known that the extremely long inspiral process that precedes the 'visible' (most energetic) final stages of the evolution (late inspiral, merger and ring-down), tends to circularize the orbits [26, 27]. This is the reason why one normally expects to find circular or quasi-circular orbits in Nature. Only recent catastrophic events near the CBC, three-body interactions or highly spinning compact objects can break this quasi-circular condition [28–30]. In this thesis, we shall always *assume circular orbits*.

Also, we shall consider the particular case of *non-spinning* black holes (BHs) [or compact starts with *negligible* effects coming from their *equation of state*]. Although this represents a restriction with respect to what is expected to be found in the Universe, the current 'state of the art' on source modeling is well-stablished for non-spinning BHs but it just starts being developed for spinning compact objects with possible presence of matter. Some of our future plans are related to the extension of the analyses performed in this thesis to the more general case of *spinning* BHs or NSs with different equations of state.

References

[1] R. A. Hulse, J. H. Taylor, Astrophys. J. **195** L51-L53 (1975).

[2] J. M. Weisberg, J. H. Taylor, Phys. Rev. Lett. **52** 1348-1350 (1984).

[3] J. H. Taylor, J. M. Weisberg, Astrophys. J. **345** 434-450 (1989).

[4] C. M. Will, *Theory and Experiment in Gravitational Physics*, (Cambridge Univ. Press) (1994).

[5] T. Damour, J. H. Taylor, Phys. Rev. D **45** 1840-1868 (1992).

[6] T. Damour, B. R. Iyer, B. S. Sathyaprakash, Phys. Rev. D **63** 044023 (2001) [Erratum-ibid. D **72** 029902 (2005)].

[7] J. Marx *et al.*, *Gravitational Waves International Committee Roadmap, The future of gravitational waves astronomy*, `http://gwic.ligo.org/roadmap/Roadmap_100627.pdf` (2010).

[8] K. S. Thorne, *Gravitational waves*, Proceedings of the Summer Study on particle and nuclear astrophysics and cosmology in the next millennium, Snowmass 1994:0160-184, Edited by E. W. Kolb and R. D. Peccei (River Edge, N.J., World Scientific) (1995), [gr-qc/9506086].

[9] C. W. Misner, K. S. Thorne, J. A. Wheeler, *Gravitation*, (W. H. Freeman and Co.) (1973).

[10] B. F. Schutz, *A First Course in General Relativity*, Second Edition, (Cambridge University Press, Cambridge, England) (2009).

[11] K. S. Thorne, in *300 Years of Gravitation*, edited by S. W. Hawking and W. Israel (Cambridge University Press, Cambridge, England) (1987) p. 330.

[12] B. F. Schutz, *Gravitational wave astronomy*, [gr-qc/9911034].

[13] M. Hendry, *An Introduction to General Relativity, Gravitational Waves and Detection Principles*, Second VESF School on Gravitational Waves, Cascina, Italy (2007).

[14] G. Hobbs, A. Lyne, M. Kramer, Chin. J. Astron. Astrophys. **6** 169 (2006).

[15] G. Hobbs *et al.*, Class. Quant. Grav. **27** 084013 (2010).

[16] A. Sesana, A. Vecchio, C. N. Colacino, Mon. Not. R. Astron. Soc. **390** 192 (2008).

[17] A. Sesana, A. Vecchio, M. Volonteri, Mon. Not. R. Astron. Soc. **394** 2255 (2009).

[18] J. Weber, Phys. Rev. **117** 306 (1960).

[19] G. E. Moss, L. R. Miller, R. L. Forward, Applied Optics **10** 2495 (1971).

[20] R. Weiss, Quarterly Progress Report of RLE, MIT **105** 54 (1972).

[21] P. Rapagnani, Class. Quant. Grav. **27** 194001 (2010).

[22] P. Astone *et al.*, Class. Quant. Grav. **25** 114048 (2008).

[23] H. Grote [for the LIGO Scientific Collaboration], Class. Quant. Grav. **27** 084003 (2010).

[24] J. Abadie *et al.* [LIGO and Virgo Collaborations], Class. Quant. Grav. **27** 173001 (2010).

[25] S. Hild, S. Chelkowski, A. Freise, "Pushing towards the ET sensitivity using 'conventional' technology," [arXiv:0810.0604].

[26] P. C. Peters, J. Mathews, Phys. Rev. **131** 435-439 (1963).

[27] P. C. Peters, Phys. Rev. **136** B1224-B1232 (1964).

[28] K. Gultekin, M. Coleman Miller, D. P. Hamilton, Astrophys. J. **640** 156-166 (2006).

[29] M. Campanelli, C. O. Lousto, Y. Zlochower, Phys. Rev. D **77** 101501 (2008).

[30] A. Sesana, Astrophys. J. **719** 851-864 (2010).

Chapter 2

Observed gravitational signals: from source emission to detected signals

From the source simulation point of view, GWs are small perturbations of the surrounding metric space that move away from the source, traveling at the speed of light. Along its way between the source and the observer, the intensity carried by the GWs will obey an inverse-square law (the emitted wavefront can be considered to be spherical) and, as with all radiation fields, the amplitude of the GWs falls off as D_L^{-1} far from the source [1]. Once the gravitational wavefront reaches the observer (in our case an interferometric detector), it modifies the metric of the surrounding space producing changes in the relative length difference of the two interferometer arms, which can be measured with extremely good accuracy making use of interferometric techniques.

The conversion process between the metric perturbation in the source frame and the measured wave-induced relative length changes of the two arms, despite being based on simple and well stablished spherical harmonics decomposition, coordinates transformations and matrix projections; it contains some subtleties and convention elections that may be relevant for any work related with GW data analysis. For this reason, we consider very important to, at least once, carefully study and fully understand the whole process from beginning to end. Indeed, this is the main purpose of the present chapter, where we will consider the particular case of CBCs.

Following this idea, this chapter has been organized in four sections, where we shall start from the raw output of a numerical simulation, this is, the Regge-Wheeler and Zerilli functions, $\Psi_{\ell m}^{(o)}$ and $\Psi_{\ell m}^{(e)}$; in order to then, add their corresponding angular dependence in form of spin-weighted spherical harmonics (see Sec. 2.1); followed by their projection into the detector's arms (Sec. 2.2). Since we are interested in data analysis studies, we shall write the final expression for the measured GW strain in its most compact form, as a simple superposition of (co)sinusoidal functions of the different GW phase harmonics

(Sec. 2.3). The following diagram schematizes the derivation process that we shall follow:

$$\left\{ \Psi_{\ell m}^{(o)}, \Psi_{\ell m}^{(e)} \right\} \xrightarrow{\text{Sec. 2.1}} \{h_+, h_\times\} \xrightarrow{\text{Sec. 2.2}} h(t) \text{ [formal]} \xrightarrow{\text{Sec. 2.3}} h(t) \text{ [useful]} .$$

Finally, in Sec. 2.4 we shall study some residual gauge-freedom in the measured GW strain, $h(t)$, that may create (exact or approximated) degeneracies between different regions in the parameter space. If they are exact, we should be able to restrict the parameter space and avoid exploring equivalent regions [this is indeed very useful in 'blind' searches, where one has to explore the whole parameter space]; in case they are merely approximated or valid in limit cases, then we won't be able to reduce the parameter space volume, but, in any case, the knowledge about their existence will help us to increase the efficiency of Markov chain Monte Carlo searches (see Chapter 6).

Throughout this chapter, we have been very careful trying to always write the explicit dependencies of the different quantities as they appear during the derivation process. If a certain quantity is time-dependent, it is denoted by a t or τ, depending on whether one is talking about the coordinate time t or the proper time at the source's reference frame τ, followed by a semicolon and the list of physical parameters it depends on, e.g. $a_{\mathrm{N}} = a_{\mathrm{N}}(\tau; \boldsymbol{\lambda}_{\mathrm{src}})$. This should help the reader to keep track of where the dependencies on different parameters come from.

2.1   Emitted gravitational wave signals from compact binaries

We consider a GW signal traveling through the space in the $-\hat{\mathbf{N}}$ direction and generated by a rotating system with angular momentum, $\mathbf{L}$. In this notation, $\hat{\mathbf{N}}$ stands for the unitary vector from the detector to the source (*i.e.* representing the source sky location), and $\hat{\mathbf{L}}$ shall represent an unitary vector parallel to $\mathbf{L}$ (see Fig. 2.1). Let us denote the angle between the angular momentum and the propagation direction of the GW as ι, that can be univocally obtained by the following two scalar expressions:

$$\cos \iota = -\hat{\mathbf{L}} \cdot \hat{\mathbf{N}} \quad , \quad \sin \iota = |\hat{\mathbf{L}} \times \hat{\mathbf{N}}| \tag{2.1}$$

Notice that $\sin \iota$ is positive defined and therefore $\iota \in [0, \pi]$. The other spherical polar angle that univocally determine the $-\hat{\mathbf{N}}$ vector measured in the source reference frame (*i.e.* the z axis parallel to the angular momentum, $\mathbf{L}$, and $x - y$ containing the orbital plane) is β, which is measured over the orbital plane from an arbitrary, but fixed, direction in this frame.

All the potential GW sources considered both for ground-based and space-based detectors are far enough to neglect parallax effects due to the motion of the detectors around the Sun and therefore, $\hat{\mathbf{N}}$ will be constant. On the other hand, fast rotating systems can have precessing orbital planes in the observational time scale (specially, if one considers spinning compact objects, where the PN coupling between the bodies' spins and their orbital angular momentum undergoes Lense-Thirring precession [2, 3]) and in these cases, $\hat{\mathbf{L}}$ would be variable over the observation time. Thus, ι and β may not be constant for some cases, although they are going to be in all the particular cases considered in this thesis.

In general, when solving the dynamics of a CBC, given the spherical symmetry of the background metric space, the metric perturbations, h, can be expanded [4, 5] in multipoles of odd or even parity according to their transformation properties under parity [this is, $(\iota, \beta) \to (\pi - \iota, \pi + \beta)$], leaving all the angular dependency for the spin-weighted spherical harmonics. Concretely, the emitted GW signal can be written in terms of the Regge-Wheeler and Zerilli functions, $\Psi^{(o)}$ and $\Psi^{(e)}$ respectively, which can be expanded in the following way [4, 5]:

$$
\begin{aligned}
h_+ - i h_\times &= \frac{1}{D_L} \sum_{\ell=2}^{\infty} \sum_{m=-\ell}^{\ell} \sqrt{\frac{(\ell+2)!}{(\ell-2)!}} \left(\Psi_{\ell m}^{(e)}(\tau; \boldsymbol{\lambda}_{\mathrm{src}}) + i \Psi_{\ell m}^{(o)}(\tau; \boldsymbol{\lambda}_{\mathrm{src}}) \right)_{-2} Y^{\ell m}(\iota, \beta) \\
&\equiv \sum_{\ell=2}^{\infty} \sum_{m=-\ell}^{\ell} h_{\ell m}(\tau; \boldsymbol{\lambda}_{\mathrm{src}}) \, _{-2}Y^{\ell m}(\iota, \beta) \, .
\end{aligned}
\tag{2.2}
$$

In this previous expression, $h_{(+,\times)} \equiv h_{(+,\times)}(\tau; \boldsymbol{\lambda}_{\mathrm{src}}, \iota, \beta)$, where $\boldsymbol{\lambda}_{\mathrm{src}} = \{m_1, m_2, D_L, \mathrm{spins} \dots\}$ are the source physical parameters and D_L the luminosity distance. Moreover, $_{-2}Y^{\ell m}(\iota, \beta)$ are the $(s = -2)$ spin-weighted spherical harmonics [5, 6] (see also Sec. 2.1.1) and $h_{\ell m}$ are simply the spin-weighted spherical harmonic components, as they are defined in [4]. Finally, let us notice that the sum over ℓ starts at $\ell = 2$, because we are only focused on the *radiative* degrees of freedom of the perturbation; it turns out that the monopole component of the metric for a vacuum perturbation ($\ell = 0$) represents a variation in the mass-parameter of the Schwarzschild solution, whereas the dipole component ($\ell = 1$) can be removed either by means of a suitable gauge transformation (when it has even parity) or by introducing an angular momentum onto the background metric (for odd-parity metric perturbations).

2.1.1 Spin ($s = -2$) weighted spherical harmonics

The analytical expressions to compute the $(s = -2)$ spin-weighted spherical harmonics in terms of the scalar spherical harmonics are given, for instance, by Nagar and Rezzolla [5] in terms of the standard scalar spherical harmonics:

$$
_{-2}Y^{\ell m}(\iota, \beta) \equiv \sqrt{\frac{(\ell-2)!}{(\ell+2)!}} \left(W^{\ell m}(\iota, \beta) - i \frac{X^{\ell m}(\iota, \beta)}{\sin \iota} \right) ,
\tag{2.3}
$$

where

$$
\begin{aligned}
W^{\ell m}(\iota, \beta) &\equiv \partial_\iota^2 Y^{\ell m} - \cot \iota \, \partial_\iota Y^{\ell m} - \frac{1}{\sin^2 \theta} \partial_\beta^2 Y^{\ell m} \tag{2.4} \\
X^{\ell m}(\iota, \beta) &\equiv 2 \left(\partial_{\iota\beta}^2 Y^{\ell m} - \cot \iota \, \partial_\iota Y^{\ell m} \right) ,
\tag{2.5}
\end{aligned}
$$

$Y^{\ell m} \equiv Y^{\ell m}(\iota, \beta)$ being the standard scalar spherical harmonics and $\partial_x f(x)$ representing the partial derivative of the function $f(x)$ with respect to the variable x. While these expressions can easily be reproduced with straightforward algebra, they are tedious to derive and hard to find in the literature; for these reasons we have decided to include their explicit expressions in Table 2.1. By combining two symmetry properties of the general spin-weighted spherical harmonics: $_sY^{\ell m *} = (-1)^{s+m} {}_{-s}Y^{\ell -m}$ and $_sY^{\ell m}(\pi - \iota, \pi + \beta) = (-1)^\ell {}_{-s}Y^{\ell m}(\iota, \beta)$ and fixing $s = -2$, we can relate the $\pm m$ modes through a parity transformation:

$$
_{-2}Y^{\ell -m}(\iota, \beta) = (-1)^{\ell+m} {}_{-2}Y^{\ell m *}(\pi - \iota, \pi + \beta) ,
\tag{2.6}
$$

where the asterisk denotes complex conjugate.

For instance, the particular explicit expressions for the $(\ell, m) = (2, \pm 2)$ spin-weighted spherical harmonics read

$$
\begin{aligned}
{}_{-2}Y^{22}(\iota, \beta) &= \frac{1}{\sqrt{4!}} \left(e^{i2\beta} \sqrt{\frac{15}{32\pi}} (3 + \cos 2\iota) - i \frac{ie^{i2\beta}\sqrt{\frac{15}{8\pi}}\sin 2\iota}{\sin \iota} \right) \\
&= \frac{1}{16}\sqrt{\frac{5}{\pi}} e^{i2\beta} (3 + \cos 2\iota + 4\cos \iota) \\
&= \frac{1}{2}\sqrt{\frac{5}{\pi}} \cos^4 \frac{\iota}{2} e^{i2\beta}
\end{aligned} \tag{2.7}
$$

and

$$
{}_{-2}Y^{2\,-2}(\iota, \beta) = {}_{-2}Y^{22\,*}(\pi - \iota, \pi + \beta) = \frac{1}{2}\sqrt{\frac{5}{\pi}} \sin^4 \frac{\iota}{2} e^{-i2\beta} . \tag{2.8}
$$

The rest of the $(s = -2)$ spin-weighted spherical harmonics (up to $\ell = 6$) are listed in Table 2.1.

2.1.2　General expression for h_+ and $h_\times$

In this thesis we consider non-spinning compact objects coalescing in near circular orbits. For these systems, Kidder [4] makes use of the fact that the mass [current] multipoles only contribute to components with $\ell + m$ even [odd], together with other symmetry properties to determine the relation between the $h_{\ell m}$ and $h_{\ell\,-m}$ components,

$$
h_{\ell\,-m} = (-1)^\ell h_{\ell m}^* . \tag{2.9}
$$

Moreover, one can, in general, write the (spin-weighted) spherical harmonic components of the gravitational emission, $h_{\ell m}$, as a complex amplitude times a complex exponential function of the (minus) m-th harmonic of the orbital phase [4]. This is,

$$
\begin{aligned}
h_{\ell m} &\equiv (h_{\ell m}^R + i h_{\ell m}^I) e^{-im\phi_{\mathrm{orb}}} \tag{2.10} \\
h_{\ell\,-m} &= (-1)^\ell h_{\ell m}^* = (-1)^\ell (h_{\ell m}^R - i h_{\ell m}^I) e^{+im\phi_{\mathrm{orb}}} , \tag{2.11}
\end{aligned}
$$

where $h_{\ell m}^{(R,I)} \equiv h_{\ell m}^{(R,I)}(\tau; \boldsymbol{\lambda}_{\mathrm{src}})$ are real quantites; $\phi_{\mathrm{orb}} \equiv \phi_{\mathrm{orb}}(\tau; \boldsymbol{\lambda}_{\mathrm{src}})$ is the orbital phase of the binary and we have used Eq. (2.9) to obtain the general expression for $h_{\ell\,-m}$. We refer the reader to Ref. [4] for the explicit expressions of $h_{\ell m}$ as a PN expansion up to the maximum known PN order.

Comment on the way to proceed and its alternative

At this point, it is important to notice that we could proceed in two different ways. From Eq. (2.10), we have $h_{\ell m} = (h_{\ell m}^R + i h_{\ell m}^I) e^{-im\phi_{\mathrm{orb}}}$, consisting in a complex amplitude that depends on the particular (ℓ, m) mode that one is considering, and a real phase independent of ℓ and with a trivial dependency on m. On the other hand, one might be interested in

---

$\ell = 2$

$$_{-2}Y^{22} = \tfrac{1}{2}e^{2i\beta}\sqrt{\tfrac{5}{\pi}}\cos\left[\tfrac{\iota}{2}\right]^4 \qquad\qquad _{-2}Y^{21} = \tfrac{1}{4}e^{i\beta}\sqrt{\tfrac{5}{\pi}}(1+\cos\iota)\sin\iota$$

$$_{-2}Y^{20} = \tfrac{1}{4}\sqrt{\tfrac{15}{2\pi}}\sin^2\iota$$

$\ell = 3$

$$_{-2}Y^{33} = -e^{3i\beta}\sqrt{\tfrac{21}{2\pi}}\cos\left[\tfrac{\iota}{2}\right]^5\sin\left[\tfrac{\iota}{2}\right] \qquad _{-2}Y^{32} = \tfrac{1}{2}e^{2i\beta}\sqrt{\tfrac{7}{\pi}}\cos\left[\tfrac{\iota}{2}\right]^4(-2+3\cos\iota)$$

$$_{-2}Y^{31} = -\tfrac{1}{32}e^{i\beta}\sqrt{\tfrac{35}{2\pi}}(\sin\iota - 4\sin 2\iota - 3\sin 3\iota) \qquad _{-2}Y^{30} = \tfrac{1}{4}\sqrt{\tfrac{105}{2\pi}}\cos\iota\ \sin^2\iota$$

$\ell = 4$

$$_{-2}Y^{44} = \tfrac{3}{64}e^{4i\beta}\sqrt{\tfrac{7}{\pi}}\csc\left[\tfrac{\iota}{2}\right]^4\sin^6\iota$$

$$_{-2}Y^{43} = -3e^{3i\beta}\sqrt{\tfrac{7}{2\pi}}\cos\left[\tfrac{\iota}{2}\right]^5\left(-2\sin\left[\tfrac{\iota}{2}\right]+\sin\left[\tfrac{3\iota}{2}\right]\right)$$

$$_{-2}Y^{42} = \tfrac{3}{4\sqrt{\pi}}e^{2i\beta}\cos\left[\tfrac{\iota}{2}\right]^4\left(9-14\cos\iota+7\cos 2\iota\right)$$

$$_{-2}Y^{41} = \tfrac{3}{32\sqrt{2\pi}}e^{i\beta}\left(3\sin\iota - 2\sin 2\iota + 7(\sin 3\iota + \sin 4\iota)\right)$$

$$_{-2}Y^{40} = \tfrac{3}{16}\sqrt{\tfrac{5}{2\pi}}(5+7\cos 2\iota)\sin^2\iota$$

$\ell = 5$

$$_{-2}Y^{55} = -e^{5i\beta}\sqrt{\tfrac{330}{\pi}}\cos\left[\tfrac{\iota}{2}\right]^7\sin\left[\tfrac{\iota}{2}\right]^3$$

$$_{-2}Y^{54} = e^{4i\beta}\sqrt{\tfrac{33}{\pi}}\cos\left[\tfrac{\iota}{2}\right]^6\left(-2+5\cos\iota\right)\sin\left[\tfrac{\iota}{2}\right]^2$$

$$_{-2}Y^{53} = -\tfrac{1}{256}e^{3i\beta}\sqrt{\tfrac{33}{2\pi}}\left(14\sin\iota - 8\sin 2\iota + 13\sin 3\iota + 36\sin 4\iota + 15\sin 5\iota\right)$$

$$_{-2}Y^{52} = \tfrac{1}{8}e^{2i\beta}\sqrt{\tfrac{11}{\pi}}\cos\left[\tfrac{\iota}{2}\right]^4\left(-32+57\cos\iota - 36\cos 2\iota + 15\cos 3\iota\right)$$

$$_{-2}Y^{51} = \tfrac{1}{256}e^{i\beta}\sqrt{\tfrac{77}{\pi}}\left(-2\sin\iota + 8\sin 2\iota - 3\sin 3\iota + 12\sin 4\iota + 15\sin 5\iota\right)$$

$$_{-2}Y^{50} = \tfrac{1}{32}\sqrt{\tfrac{1155}{2\pi}}\left(5\cos\iota + 3\cos 3\iota\right)\sin^2\iota$$

$\ell = 6$

$$_{-2}Y^{66} = \tfrac{3}{512}e^{6i\beta}\sqrt{\tfrac{715}{\pi}}\csc\left[\tfrac{\iota}{2}\right]^4\sin^8\iota$$

$$_{-2}Y^{65} = -\tfrac{1}{2}e^{5i\beta}\sqrt{\tfrac{2145}{\pi}}\cos\left[\tfrac{\iota}{2}\right]^7\left(-1+3\cos\iota\right)\sin\left[\tfrac{\iota}{2}\right]^3$$

$$_{-2}Y^{64} = \tfrac{1}{8}e^{4i\beta}\sqrt{\tfrac{195}{2\pi}}\cos\left[\tfrac{\iota}{2}\right]^6\left(35-44\cos\iota+33\cos 2\iota\right)\sin\left[\tfrac{\iota}{2}\right]^2$$

$$_{-2}Y^{63} = \tfrac{1}{2048}3e^{3i\beta}\sqrt{\tfrac{13}{\pi}}\left(20\sin\iota - 51\sin 2\iota + 6\sin 3\iota - 5(4\sin 4\iota + 22\sin 5\iota + 11\sin 6\iota)\right)$$

$$_{-2}Y^{62} = \tfrac{1}{256}e^{2i\beta}\sqrt{\tfrac{13}{\pi}}\cos\left[\tfrac{\iota}{2}\right]^4\left(1709-3096\cos\iota+2340\cos 2\iota - 1320\cos 3\iota + 495\cos 4\iota\right)$$

$$_{-2}Y^{61} = \tfrac{1}{1024}e^{i\beta}\sqrt{\tfrac{65}{2\pi}}\left(20\sin\iota - 17\sin 2\iota + 54\sin 3\iota - 12\sin 4\iota + 66\sin 5\iota + 99\sin 6\iota\right)$$

$$_{-2}Y^{60} = \tfrac{1}{512}\sqrt{\tfrac{1365}{\pi}}\left(35+60\cos 2\iota+33\cos 4\iota\right)\sin^2\iota$$

Table 2.1: $(s=-2)$ spin-weighted spherical harmonics, $_{-2}Y^{\ell m} \equiv {}_{-2}Y^{\ell m}(\iota,\beta)$, up to $\ell=6$, obtained from the explicit expression Eq. (2.3). The harmonics with $m<0$ can be obtained from these ones, making use of Eq. (2.6).

having a real amplitude and phase values, but adding the (ℓ, m) dependency also to the phase:

$$h_{\ell m} = |h_{\ell m}|e^{-i\varepsilon_{\ell m}} \ , \tag{2.12}$$

where

$$|h_{\ell m}| \quad \equiv \quad \sqrt{(h_{\ell m}^R)^2 + (h_{\ell m}^I)^2} \ , \tag{2.13}$$

$$\varepsilon_{\ell m} \quad \equiv \quad m\phi_{\mathrm{orb}} - \arctan\left(\frac{h_{\ell m}^I}{h_{\ell m}^R}\right) \ . \tag{2.14}$$

In this thesis we shall proceed using Eq. (2.10) since, indeed, we shall make use of its trivial phase dependency with $\{\ell, m\}$, but it is important to notice that in a different context, it might be more useful to proceed with the other generic way (2.12) of writing things.

Dominant $(2, 2)$ mode

By combining Eqs. (2.6) and (2.10)-(2.11) and introducing them into (2.2) we shall obtain below the generic expressions for h_+ and $h_\times$, but before doing this and for pedagogical reasons, let us start first deriving results for the dominant $(\ell = 2, m = \pm 2)$ modes [usually referred to them just as the (2,2) mode]. Thus, we proceed by introducing the explicit expressions of the spin-weighted spherical harmonics for these modes [Eqs. (2.7)-(2.8) and (2.10)-(2.11)] into Eq. (2.2),

$$
\begin{aligned}
h_+ - ih_\times \quad &= \quad h_{22}(\tau; \boldsymbol{\lambda}_{\mathrm{src}}) \, {}_{-2}Y^{22}(\iota, \beta) + h_{2\,-2}(\tau; \boldsymbol{\lambda}_{\mathrm{src}}) \, {}_{-2}Y^{2\,-2}(\iota, \beta) \\
&= \quad \frac{1}{2}\sqrt{\frac{5}{\pi}}\left[(h_{22}^R + ih_{22}^I)e^{-i(2\phi_{\mathrm{orb}}-2\beta)}\cos^4\frac{\iota}{2} + (h_{22}^R - ih_{22}^I)e^{i(2\phi_{\mathrm{orb}}-2\beta)}\sin^4\frac{\iota}{2}\right] \ ,
\end{aligned}
$$

and, after some basic algebra one can finally get

$$
\begin{aligned}
h_+(\tau; \boldsymbol{\lambda}_{\mathrm{src}}, \iota, \beta\!\!\!/) \quad &= \quad \frac{1}{2}\sqrt{\frac{5}{\pi}}\left(\frac{1 + \cos^2\iota}{2}\right)\left[h_{22}^R\cos(2\phi_{\mathrm{orb}} - 2\beta) + h_{22}^I\sin(2\phi_{\mathrm{orb}} - 2\beta)\right] \ , \\
h_\times(\tau; \boldsymbol{\lambda}_{\mathrm{src}}, \iota, \beta\!\!\!/) \quad &= \quad \frac{1}{2}\sqrt{\frac{5}{\pi}}\cos\iota\left[h_{22}^R\sin(2\phi_{\mathrm{orb}} - 2\beta) - h_{22}^I\cos(2\phi_{\mathrm{orb}} - 2\beta)\right] \ , \tag{2.15}
\end{aligned}
$$

where we recall the explicit dependencies, $h_{22}^{(R,I)} \equiv h_{22}^{(R,I)}(\tau; \boldsymbol{\lambda}_{\mathrm{src}})$ and $\phi_{\mathrm{orb}} \equiv \phi_{\mathrm{orb}}(\tau; \boldsymbol{\lambda}_{\mathrm{src}})$. Notice that, since we are considering a $m = 2$ mode, the GW signal contains the second harmonic of the orbital phase, always combined with the spherical angle measured over the orbital plane, β, in the same way. We shall see that this is satisfied in the general case and, since the $(2, 2)$ mode is the one carrying most of the GW energy[1], this is why

$$\phi_{\mathrm{GW}}(\tau; \boldsymbol{\lambda}_{\mathrm{src}}, \beta\!\!\!/) \equiv 2\phi_{\mathrm{orb}}(\tau; \boldsymbol{\lambda}_{\mathrm{src}}) - 2\beta \tag{2.16}$$

is usually defined as the *GW phase*, and the only dependency of the measured GW signal with the angle β can be absorbed with the arbitrary initial orbital phase, namely $\phi_0 \equiv \phi_{\mathrm{GW}}(t = 0)$, if we assume β to be constant. For this reason, we represent the β-dependency of ϕ_{GW} as '$\beta\!\!\!/$'. Note in (2.16) the factor 2 with respect to the *orbital phase*; which shall also be present when one talks about the *GW frequency*, $F \equiv \dot\phi_{\mathrm{GW}}/(2\pi)$, being twice the *orbital frequency* [when β is constant].

---

[1] At least, for non-spinning sources in quasi-circular orbits.

For many data analysis purposes, it is enough to just consider the dominant $(2, 2)$ mode of the spherical harmonic decomposition and, as a matter of fact, one, normally, only considers the leading order from the PN expansion of h_{22}, obtaining what is usually called *restricted post-Newtonian approximation*. Under this approximation, the GW amplitude turns out to be,

$$h_{22}^R(\tau; \boldsymbol{\lambda}_{\text{src}}) = 2\sqrt{\frac{\pi}{5}} a_{\text{N}} \qquad ; \qquad h_{22}^I(\tau; \boldsymbol{\lambda}_{\text{src}}) = 0$$

[where the subscript 'N' stands for 'Newtonian', as the leading order in the PN expansion], whereas the GW phase, ϕ_{GW}, incorporates all the known PN corrections. The use of the *restricted* PN approximation is justified in a number of cases, since it simplifies significantly the expression of the gravitational waveform while keeping all the PN corrections to the phase, which is the most sensitive quantity when describing long GW signals, as any dephasing error is accumulated over many cycles. However, as we shall see in Chapter 4, in some cases the inclusion of full information from all the modes may significantly improve the detection and, specially, the parameter estimation of GW signals. The reason behind this fact is rather not because of adding PN corrections to the amplitude of the dominant harmonic, but because of adding contributions to higher harmonics of the signal [to $3f_{\text{orb}}$, $4f_{\text{orb}}, \dots$] which (despite being subdominant) increase the richness of the waveform.

With this, in the *restricted* PN approximation, the GW signal observed from the Solar System Barycenter (SSB) takes the following simple form:

$$
\begin{aligned}
h_+(\tau; \boldsymbol{\lambda}_{\text{src}}, \iota) &= \left[\frac{1 + \cos^2 \iota}{2}\right] a_{\text{N}} \cos \phi_{\text{GW}} , \\
h_\times(\tau; \boldsymbol{\lambda}_{\text{src}}, \iota) &= [\cos \iota] \, a_{\text{N}} \sin \phi_{\text{GW}} .
\end{aligned}
\tag{2.17}
$$

In general, all quantities may change over time, although in the case of short-lived, non-precessing binaries, the angle ι will be constant and therefore, the time dependence will come from $a_{\text{N}} = a_{\text{N}}(\tau; \boldsymbol{\lambda}_{\text{src}})$ and $\phi_{\text{GW}} = \phi_{\text{GW}}(\tau; \boldsymbol{\lambda}_{\text{src}})$ in the form of a chirping signal, *i.e.* a sinusoidal signal with amplitude and frequency increasing with time (see Chapter 3 for further details).

Looking at the leading order in the PN expansion for h_{22}, *e.g.* in [4], we obtain that

$$a_{\text{N}}(\tau; \boldsymbol{\lambda}_{\text{src}}) = -4 \frac{\nu M}{D_L} \mathrm{v}^2 , \tag{2.18}$$

where $M = m_1 + m_2$ is the total mass of the system, $\nu = \frac{m_1 m_2}{M^2}$ is the symmetric mass ratio, D_L is the luminosity distance to the source and $\mathrm{v} = (\pi f M)^{1/3}$ is a characteristic velocity of the two orbiting objects which also has the role of a PN expansion parameter. Here we keep an explicit negative sign coming from the second derivative of a complex exponential function.

Including all (ℓ, m) modes

Let us now consider the most general case, where all the spherical harmonic components are included in the gravitational waveform. Formally, this calculation is equivalent to what we have done previously to obtain Eq. (2.15) and indeed the first thing that we shall consider is the relation between the $h_{\ell \pm m}$ components given by (2.9). Moreover, we notice that any

of the $(s = -2)$ spin-weighted spherical harmonics listed in Table 2.1 can be generally written as

$$_{-2}Y^{\ell m}(\iota, \beta) = {}_{-2}Y^{\ell m}(\iota, 0)e^{im\beta} \tag{2.19}$$

where $_{-2}Y^{\ell m}(\iota, 0)$ is always a real quantity[2]; therefore, making use of (2.6),

$$_{-2}Y^{\ell - m}(\iota, \beta) = (-1)^\ell {}_{-2}Y^{\ell m}(\pi - \iota, 0)e^{-im\beta} \ . \tag{2.20}$$

With these results, we can expand the expression given in Eq. (2.2) and in particular, we shall write the contribution from a particular ℓ and $\pm m \neq 0$ (both signs) values as

$$
\begin{aligned}
_{-2}Y^{\ell m} h_{\ell m} + {}_{-2}Y^{\ell - m} h_{\ell - m} = & \ [h_{\ell m}^R + ih_{\ell m}^I] \ {}_{-2}Y^{\ell m}(\iota, 0)e^{-im(\phi_{\rm orb} - \beta)} \\
& + (-1)^{2\ell}[h_{\ell m}^R - ih_{\ell m}^I] \ {}_{-2}Y^{\ell m}(\pi - \iota, 0)e^{im(\phi_{\rm orb} - \beta)} \ ,
\end{aligned} \tag{2.21}
$$

and taking into account that ℓ is an integer number and doing some basic algebra, one finally obtains the following result:

$$
\begin{aligned}
(2.21) = & \ \mathcal{S}^{\ell m}(\iota) \left(h_{\ell m}^R \cos[m(\phi_{\rm orb} - \beta)] + h_{\ell m}^I \sin[m(\phi_{\rm orb} - \beta)] \right) \\
& -i \ \mathcal{D}^{\ell m}(\iota) \left(h_{\ell m}^R \sin[m(\phi_{\rm orb} - \beta)] - h_{\ell m}^I \cos[m(\phi_{\rm orb} - \beta)] \right) \ , \ (2.22)
\end{aligned}
$$

where the real functions $\mathcal{S}^{\ell m}(\iota)$ and $\mathcal{D}^{\ell m}(\iota)$ have been defined as

$$\binom{\mathcal{S}^{\ell m}}{\mathcal{D}^{\ell m}}(\iota) \equiv {}_{-2}Y^{\ell m}(\iota, 0) \pm {}_{-2}Y^{\ell m}(\pi - \iota, 0) \ , \tag{2.23}$$

with $\mathcal{S}$ standing for 'sum' and $\mathcal{D}$ for 'difference'. Given the explicit expressions of the spin-weighted spherical harmonics in Tab. 2.1, it is straightforward to obtain the analytical expressions of these two functions too (see Table 2.2 for the expressions up to $\ell = 6$).

Equation (2.22) is nothing but a generalization, for arbitrary (ℓ, m) values, of the result presented above [Eq. (2.15)] for the $(2, 2)$ mode. All the (m-th) modes contribute as (co)sinusoidal functions of $\frac{m}{2}\phi_{\rm GW}$, so all the dependency on the angle β [we recall that it is an angle measured over the orbital plane from a fixed direction] can be absorbed in the definition of the GW phase (2.16). Moreover, one can see directly from the definition of $\mathcal{S}^{\ell m}(\iota)$ and $\mathcal{D}^{\ell m}(\iota)$ that the '+' polarizations [sum over real parts of (2.22)] and '×' polarizations [sum over (minus) imaginary parts of (2.22)] will satisfy, in general [recall the definition in Eq. (2.2)], the same symmetry property, under the transformation of the angle ι into its supplementary, as the $\mathcal{S}^{\ell m}(\iota)$ and $\mathcal{D}^{\ell m}(\iota)$ functions, i.e. :

$$h_{\binom{+}{\times}}(\tau; \boldsymbol{\lambda}_{\rm src}, \pi - \iota) = \binom{+}{-} h_{\binom{+}{\times}}(\tau; \boldsymbol{\lambda}_{\rm src}, \iota) \ . \tag{2.24}$$

This general property, that has naturally appeared in our calculations, will be very important from a data analysis point of view, on the one hand because it will reduce the parameter space to be explored by a factor two, going from a possible range of $\iota \in [0, \pi]$ [we recall that ι was a mod(π) angle by definition: angle between two directions] to the practical range $\iota \in [0, \pi/2]$ and, on the other hand, because it may create some degeneracies in the parameter space.

---

[2]Indeed, this can be formally demonstrated from the definition of the $(s = -2)$ spin-weighted spherical harmonics, Eq. (2.3).

The cases with $m = 0$ do not require to sum the positive and negative indexes as they are just one single term. However, they can be formally written as Eq. (2.22) [with just one term in the l.h.s.] by defining

$$\mathcal{S}^{\ell 0}(\iota) = \mathcal{D}^{\ell 0}(\iota) \equiv {}_{-2}Y^{\ell 0}(\iota, 0) \ . \tag{2.25}$$

Finally, the generic sum given at the very beginning of this discussion, Eq. (2.2), can be rewritten as sums of sinusoidal functions of the different harmonics of the orbital phase; obtaining:

$$
\begin{aligned}
h_+(\tau; \boldsymbol{\lambda}_{\mathrm{src}}, \iota) &\equiv \sum_{m=0}^{\infty} \left[u_{+,m} \cos \left(\tfrac{m}{2} \phi_{\mathrm{GW}} \right) + w_{+,m} \sin \left(\tfrac{m}{2} \phi_{\mathrm{GW}} \right) \right] \ , \\
h_\times(\tau; \boldsymbol{\lambda}_{\mathrm{src}}, \iota) &\equiv \sum_{m=0}^{\infty} \left[u_{\times,m} \cos \left(\tfrac{m}{2} \phi_{\mathrm{GW}} \right) + w_{\times,m} \sin \left(\tfrac{m}{2} \phi_{\mathrm{GW}} \right) \right] \ ,
\end{aligned}
\tag{2.26}
$$

where the factors $(u, w)_{(+,\times),m}$ can be obtained from the spin-weighted spherical harmonics, $h_{\ell m}$, explicitly given in Ref. [4] and the 'sum' and 'difference' angular functions written in Tab. 2.2. Let us recall that all the dependency on β has been absorbed in the definition of the GW phase $\phi_{\mathrm{GW}}(\tau; \boldsymbol{\lambda}_{\mathrm{src}})$, see Eq. (2.16), and the amplitude terms can be written as

$$
\begin{aligned}
u_{+,m}(\tau; \boldsymbol{\lambda}_{\mathrm{src}}, \iota) &\equiv \sum_{\ell} \mathcal{S}^{\ell m}(\iota) \, h_{\ell m}^R(\tau; \boldsymbol{\lambda}_{\mathrm{src}}) \ , \\
u_{\times,m}(\tau; \boldsymbol{\lambda}_{\mathrm{src}}, \iota) &\equiv -\sum_{\ell} \mathcal{D}^{\ell m}(\iota) \, h_{\ell m}^I(\tau; \boldsymbol{\lambda}_{\mathrm{src}}) \ , \\
w_{+,m}(\tau; \boldsymbol{\lambda}_{\mathrm{src}}, \iota) &\equiv \sum_{\ell} \mathcal{S}^{\ell m}(\iota) \, h_{\ell m}^I(\tau; \boldsymbol{\lambda}_{\mathrm{src}}) \ , \\
w_{\times,m}(\tau; \boldsymbol{\lambda}_{\mathrm{src}}, \iota) &\equiv \sum_{\ell} \mathcal{D}^{\ell m}(\iota) \, h_{\ell m}^R(\tau; \boldsymbol{\lambda}_{\mathrm{src}}) \ ,
\end{aligned}
\tag{2.27}
$$

where have used a shortened notation for the sum symbol, $\sum_{\ell} \equiv \sum_{\ell=\max(2,m)}^{\infty}$. Moreover, note that in the previous expressions, the double sum over ℓ and m has been rewritten from the original $\sum_{\ell=2}^{\infty} \sum_{m=0}^{\ell}$ in Eq. (2.2) after pairing the $\pm m$ terms off, to the equivalent $\sum_{m=0}^{\infty} \sum_{\ell=\max(2,m)}^{\infty}$.

When one is working with the PN formalism, each spherical harmonic component $h_{\ell m}$ is written as a PN expansion series [4] and therefore, each of the quantities that appear in Eqs. (2.27) is indeed a sum over ℓ *and* over the PN order, n.

After a careful study of the quantities in Eq. (2.27), either within the effective-one-body (EOB) formalism or looking directly at the PN expansion terms, one finds out that there are some common terms that can be factored out. On the one hand, we shall factor the 'Newtonian' amplitude out, a_{N} [see definition in Eq. (2.18)], since it contains all the information about the order of magnitude and units of the GW amplitude; on the other hand, there are several factors common to all the $u_{(+,\times),m}$ and $w_{(+,\times),m}$ functions of a particular m-th harmonic [7] and we shall see later that it is indeed very convenient to also factor them out, mainly because these factors may be zero at some point and having them explicitly factorized will help avoiding possible numerical divergences. In particular, we shall define a new $\hat{u}_{(+,\times),m}$ and $\hat{w}_{(+,\times),m}$ functions as follows:

$$
\begin{pmatrix} u(\tau; \boldsymbol{\lambda}_{\mathrm{src}}, \iota) \\ w(\tau; \boldsymbol{\lambda}_{\mathrm{src}}, \iota) \end{pmatrix}_{(+,\times),m} \equiv a_{\mathrm{N}}(\tau; \boldsymbol{\lambda}_{\mathrm{src}}) \Upsilon_m(\boldsymbol{\lambda}_{\mathrm{src}}, \iota) \begin{pmatrix} \hat{u}(\tau; \boldsymbol{\lambda}_{\mathrm{src}}, \iota) \\ \hat{w}(\tau; \boldsymbol{\lambda}_{\mathrm{src}}, \iota) \end{pmatrix}_{(+,\times),m} \ , \tag{2.28}
$$

where the functions Υ_m (for $m \le 8$) are defined as

$$
\begin{aligned}
\Upsilon_{m=0}(\boldsymbol{\lambda}_{\mathrm{src}}, \iota) &\equiv 1 & \Upsilon_{m=1}(\boldsymbol{\lambda}_{\mathrm{src}}, \iota) &\equiv \tfrac{\delta m}{M}\sin\iota \\
\Upsilon_{m=2}(\boldsymbol{\lambda}_{\mathrm{src}}, \iota) &\equiv 1 & \Upsilon_{m=3}(\boldsymbol{\lambda}_{\mathrm{src}}, \iota) &\equiv \tfrac{\delta m}{M}\sin\iota \\
\Upsilon_{m=4}(\boldsymbol{\lambda}_{\mathrm{src}}, \iota) &\equiv \sin^2\iota & \Upsilon_{m=5}(\boldsymbol{\lambda}_{\mathrm{src}}, \iota) &\equiv \tfrac{\delta m}{M}\sin^3\iota \quad . \\
\Upsilon_{m=6}(\boldsymbol{\lambda}_{\mathrm{src}}, \iota) &\equiv \sin^4\iota & \Upsilon_{m=7}(\boldsymbol{\lambda}_{\mathrm{src}}, \iota) &\equiv \tfrac{\delta m}{M}\sin^5\iota \\
\Upsilon_{m=8}(\boldsymbol{\lambda}_{\mathrm{src}}, \iota) &\equiv \sin^6\iota &&
\end{aligned}
\tag{2.29}
$$

[We recall that $M = m_1 + m_2$ is the total mass of the binary system, and $\delta m = m_2 - m_1$ is the mass difference.] Besides this, we have noticed that properly (trigonometric) expanding all the $\mathcal{D}^{\ell m}(\iota)$ functions, they turn out to be proportional to 'cos ι' and so all '×' polarization terms are, *i.e.* $(u, w)_{\times, m} \propto \cos\iota$ for all m. We do not write it explicitly since we shall not use this property, although we found useful to let the reader know about it.

We shall see below that the notation used in Eqs. (2.26) and (2.28) is very convenient when expressing the measured strain in a GW detector as a single cosine function [see Eq. (2.55) below] and therefore, this formal expression for h_+ and $h_\times$ as an harmonics expansion is sometimes taken as the starting point for many data analysis studies [7–11]. Since from now on, there shall not be any more explicit references to the spherical harmonics, and in order to not confuse the m-th harmonic with the any 'mass' parameter, a *change of notation* is usually adopted at this point, replacing m by j. Thus, from this moment on, we shall refer any of the terms of the sum in Eq. (2.26) as the j-th harmonic of the GW signal:

$$
j \equiv m \ .
\tag{2.30}
$$

2.2   Detected gravitational wave strain

The GW signal described in the previous section as the superposition of two orthogonal polarizations, will travel, as it is predicted by the theory of general relativity, almost unaltered [given the almost null interaction of gravitational radiation with matter] at the speed of light from the violent source that generated it to the observer at Earth. Thus, in a Cartesian coordinate system tied to the wave's propagation, $\{x', y', z'\}$, where the GW travels in the $+z'$ direction and the perturbations are contained within the $x' - y'$ plane, with the x' direction being the main axis of the '+' polarization, the GW tensor in simply given by (see Sec. 1.1)

$$
H' = h_+ \left[\hat{\mathbf{x}}' \otimes \hat{\mathbf{x}}' - \hat{\mathbf{y}}' \otimes \hat{\mathbf{y}}' \right] + h_\times \left[\hat{\mathbf{x}}' \otimes \hat{\mathbf{y}}' + \hat{\mathbf{y}}' \otimes \hat{\mathbf{x}}' \right] ,
\tag{2.31}
$$

where $\hat{\mathbf{x}}'$ / $\hat{\mathbf{y}}'$ represents a unit vector parallel to the x' / y' axis, '$\otimes$' denotes the tensorial product and $h_{(+,\times)} \equiv h_{(+,\times)}(\tau; \boldsymbol{\lambda}_{\mathrm{src}}, \iota)$ are the orthogonal polarizations given in Eq. (2.26) as a function of the orientation angle, ι; the GW phase, $\phi_{\mathrm{GW}}(\tau; \boldsymbol{\lambda}_{\mathrm{src}})$; and the different spherical harmonics components, $h_{\ell m}(\tau; \boldsymbol{\lambda}_{\mathrm{src}})$.

As a metric perturbation, the effects of a GW consist on stretching and compressing the space in a perpendicular plane to the propagation direction. These are, precisely, the effects that one will measure with an interferometric detector and in particular, the length

$\ell = 2$

$\mathcal{S}^{22} = \frac{1}{4}\sqrt{\frac{5}{\pi}}(1+\cos^2\iota)$ $\qquad\qquad$ $\mathcal{D}^{22} = \frac{1}{2}\sqrt{\frac{5}{\pi}}\cos\iota$

$\mathcal{S}^{21} = \frac{1}{2}\sqrt{\frac{5}{\pi}}\sin\iota$ $\qquad\qquad$ $\mathcal{D}^{21} = \frac{1}{4}\sqrt{\frac{5}{\pi}}\sin 2\iota$

$\ell = 3$

$\mathcal{S}^{33} = -\frac{1}{16}\sqrt{\frac{21}{2\pi}}(5\sin\iota+\sin 3\iota)$ $\qquad$ $\mathcal{D}^{33} = -\frac{1}{4}\sqrt{\frac{21}{2\pi}}\sin 2\iota$

$\mathcal{S}^{32} = \frac{1}{2}\sqrt{\frac{7}{\pi}}\cos 2\iota$ $\qquad$ $\mathcal{D}^{32} = \frac{1}{16}\sqrt{\frac{7}{\pi}}(5\cos\iota+3\cos 3\iota)$

$\mathcal{S}^{31} = -\frac{1}{16}\sqrt{\frac{35}{2\pi}}(\sin\iota-3\sin 3\iota)$ $\qquad$ $\mathcal{D}^{31} = \frac{1}{4}\sqrt{\frac{35}{2\pi}}\sin 2\iota$

$\ell = 4$

$\mathcal{S}^{44} = \frac{3}{16}\sqrt{\frac{7}{\pi}}(3+\cos\iota)\sin^2\iota$ $\qquad$ $\mathcal{D}^{44} = \frac{3}{4}\sqrt{\frac{7}{\pi}}\cos\iota\sin^2\iota$

$\mathcal{S}^{43} = \frac{3}{16}\sqrt{\frac{7}{2\pi}}(\sin\iota-3\sin 3\iota)$ $\qquad$ $\mathcal{D}^{43} = -\frac{3}{2}\sqrt{\frac{7}{2\pi}}\cos^3\iota\sin\iota$

$\mathcal{S}^{42} = \frac{3}{32\sqrt{\pi}}(5+4\cos 2\iota+7\cos 4\iota)$ $\qquad$ $\mathcal{D}^{42} = \frac{3}{16\sqrt{\pi}}(\cos\iota+7\cos 3\iota)$

$\mathcal{S}^{41} = \frac{3}{16\sqrt{2\pi}}(3\sin\iota+7\sin 3\iota)$ $\qquad$ $\mathcal{D}^{41} = \frac{3}{16\sqrt{2\pi}}(-2\sin 2\iota+7\sin 4\iota)$

$\ell = 5$

$\mathcal{S}^{55} = -\frac{1}{16}\sqrt{\frac{165}{2\pi}}(3+\cos 2\iota)\sin^3\iota$ $\qquad$ $\mathcal{D}^{55} = -\frac{1}{4}\sqrt{\frac{165}{2\pi}}\cos\iota\sin^3\iota$

$\mathcal{S}^{54} = \frac{1}{4}\sqrt{\frac{33}{\pi}}(1+2\cos 2\iota)\sin^2\iota$ $\qquad$ $\mathcal{D}^{54} = \frac{1}{32}\sqrt{\frac{33}{\pi}}(19\cos\iota+5\cos 3\iota)\sin^2\iota$

$\mathcal{S}^{53} = -\frac{1}{128}\sqrt{\frac{33}{2\pi}}(14\sin\iota+13\sin 3\iota+15\sin 5\iota)$ $\qquad$ $\mathcal{D}^{53} = \frac{1}{32}\sqrt{\frac{33}{2\pi}}(2\sin 2\iota-9\sin 4\iota)$

$\mathcal{S}^{52} = \frac{1}{8}\sqrt{\frac{11}{\pi}}(\cos 2\iota+3\cos 4\iota)$ $\qquad$ $\mathcal{D}^{52} = \frac{1}{64}\sqrt{\frac{11}{\pi}}(14\cos\iota+3(\cos 3\iota+5\cos 5\iota))$

$\mathcal{S}^{51} = \frac{1}{128}\sqrt{\frac{77}{\pi}}(-2\sin\iota-3\sin 3\iota+15\sin 5\iota)$ $\qquad$ $\mathcal{D}^{51} = \frac{1}{32}\sqrt{\frac{77}{\pi}}(2\sin 2\iota+3\sin 4\iota)$

$\ell = 6$

$\mathcal{S}^{66} = \frac{3}{128}\sqrt{\frac{715}{\pi}}(3+\cos 2\iota)\sin^4\iota$ $\qquad$ $\mathcal{D}^{66} = \frac{3}{32}\sqrt{\frac{715}{\pi}}\cos\iota\ \sin^4\iota$

$\mathcal{S}^{65} = -\frac{1}{64}\sqrt{\frac{2145}{\pi}}(3+5\cos 2\iota)\sin^3\iota$ $\qquad$ $\mathcal{D}^{65} = -\frac{1}{128}\sqrt{\frac{2145}{\pi}}(13\cos\iota+3\cos 3\iota)\sin^3\iota$

$\mathcal{S}^{64} = \frac{1}{256}\sqrt{\frac{195}{2\pi}}(67+92\cos 2\iota+33\cos 4\iota)\sin^2\iota$ $\qquad$ $\mathcal{D}^{64} = \frac{1}{32}\sqrt{\frac{195}{2\pi}}(13\cos\iota+11\cos 3\iota)\sin^2\iota$

$\mathcal{S}^{63} = \frac{3}{512}\sqrt{\frac{13}{\pi}}(10\sin\iota+3\sin 3\iota-55\sin 5\iota)$ $\qquad$ $\mathcal{D}^{63} = -\frac{3}{1024}\sqrt{\frac{13}{\pi}}(51\sin 2\iota+20\sin 4\iota+55\sin 6\iota)$

$\mathcal{S}^{62} = \frac{1}{2048}\sqrt{\frac{13}{\pi}}(289\cos 2\iota+30(7+\cos 4\iota)+495\cos 6\iota)$ $\qquad$ $\mathcal{D}^{62} = \frac{1}{512}\sqrt{\frac{13}{\pi}}(10\cos\iota+81\cos 3\iota+165\cos 5\iota)$

$\mathcal{S}^{61} = \frac{1}{256}\sqrt{\frac{65}{2\pi}}(10\sin\iota+27\sin 3\iota+33\sin 5\iota)$ $\qquad$ $\mathcal{D}^{61} = \frac{1}{512}\sqrt{\frac{65}{2\pi}}(-17\sin 2\iota-12\sin 4\iota+99\sin 6\iota)$

Table 2.2: 'Sum' $[\mathcal{S}^{\ell m} \equiv \mathcal{S}^{\ell m}(\iota)]$ and 'difference' $[\mathcal{D}^{\ell m} \equiv \mathcal{D}^{\ell m}(\iota)]$ functions defined in Eq. (2.23) and computed from the explicit expressions of the $(s=-2)$ spin-weighted spherical harmonics listed in Tab. 2.1

difference between the two arms of the interferometer. The aim of this section is to translate the general tensor expression for a gravitational signal written in the wave Cartesian coordinate system, Eq. (2.31), into the measured differences between the wave-induced relative length changes of the two interferometer arms, which is an scalar[3] quantity. The response of a laser interferometric detector to a weak, plane, GW on the *long wavelength approximation (LWA)* (*i.e.* when the size of the detector is much smaller than the reduced wavelength $\lambda/(2\pi)$ of the wave) is well known [12] and can be computed as[4]

$$h(t) \equiv \frac{\Delta L_{\text{arms}}(t)}{L} = \frac{1}{2}\,\hat{\mathbf{n}}_1^T \cdot H \cdot \hat{\mathbf{n}}_1 - \frac{1}{2}\,\hat{\mathbf{n}}_2^T \cdot H \cdot \hat{\mathbf{n}}_2 \; . \qquad (2.32)$$

Here, $\hat{\mathbf{n}}_1$ and $\hat{\mathbf{n}}_2$ denote the unit vectors parallel to the two detector's arms (the order of arms is defined such that the vector $\hat{\mathbf{n}}_1 \times \hat{\mathbf{n}}_2$ points *outwards* from the surface of the Earth), H is the 3-dimensional matrix of the spatial metric perturbation produced by the wave, and a dot stands for the standard scalar product in the 3-dimensional Cartesian space. Notice that, since Eq. (2.32) is an scalar expression, it can be computed in any coordinates system.

The *long wavelength approximation* is completely valid for current and advanced ground-based interferometers, as they are [at most] 4 km long and their frequency window's high-end, $f < 2000$ Hz, translates into a reduced wavelength of $\frac{\lambda}{2\pi} > 24$ km. The future 3rd generation interferometers, such as ET, are planned to be $L_{\text{ET}} = 10$ km long, and therefore one might consider going beyond the LWA for very high frequency sources. LISA, on the other hand, is going to have an arm-length of $L_{\text{LISA}} = 5 \times 10^6$ km and it is expected to observe signals up to $f < 0.1$ Hz, which translates into $\frac{\lambda}{2\pi} > 0.45 \times 10^6$ km. Thus, LISA is going to have a non-negligible fraction of its frequency window where one must take into account the GW phase variation as the laser light of the interferometer travels between the two mirrors. The resulting response of a laser interferometric detector beyond the LWA is also well-known [13], namely the *time delay interferometry (TDI)*, and involve the evaluation of the GW waveform at different instants. We shall not go into any more details about TDI in this thesis, since the LWA has been assumed to be valid in all the studies we have performed, which is strictly true for all the ground-based detectors studies (Chapter 8) and a very good approximation for all the LISA studies that we have carried out (Chapters 4-7), since most of the sources considered lie at the very low part of the LISA's frequency window: $f \sim 10^{-4}$ Hz, which means $\frac{\lambda}{2\pi} \sim 500 \times 10^6$ km $\gg L_{\text{LISA}}$.

Before proceeding with the derivations, let us properly introduce the *three* Cartesian coordinate systems that we shall consider: a wave coordinate system $\{x', y', z'\}$ in where the GW travels in the $+z'$ direction; the "barred" coordinates $\{\overline{x}, \overline{y}, \overline{z}\}$ tied to the detector; and the "unbarred" coordinates $\{x, y, z\}$ fixed to the ecliptic plane and therefore, untied to the detector's motion. In particular,

- $\{x', y', z'\}$ is the *wave* Cartesian coordinate system, where the GW travels in the $+z'$ direction and the node direction of the '+' polarization is parallel to the x' axis. In this frame, the 3-dimensional matrix of the spatial metric perturbation, H', is simply

---

[3]By scalar, we mean that the result is invariant under Cartesian coordinate transformations.

[4]We recall that the relative length change produced by a GW is $\frac{\Delta L}{L} = \frac{h}{2}$. Now, considering a two-arms interferometer and given the quadrupole nature of gravitational radiation, when one arm is stretched in a certain direction, it is compressed in the orthogonal one; *i.e.* $L_x = L + \Delta L$ and $L_y = L - \Delta L$, hence $\frac{\Delta L_{\text{arms}}}{L} \equiv \frac{L_x - L_y}{L} = 2\frac{\Delta L}{L} = h$.
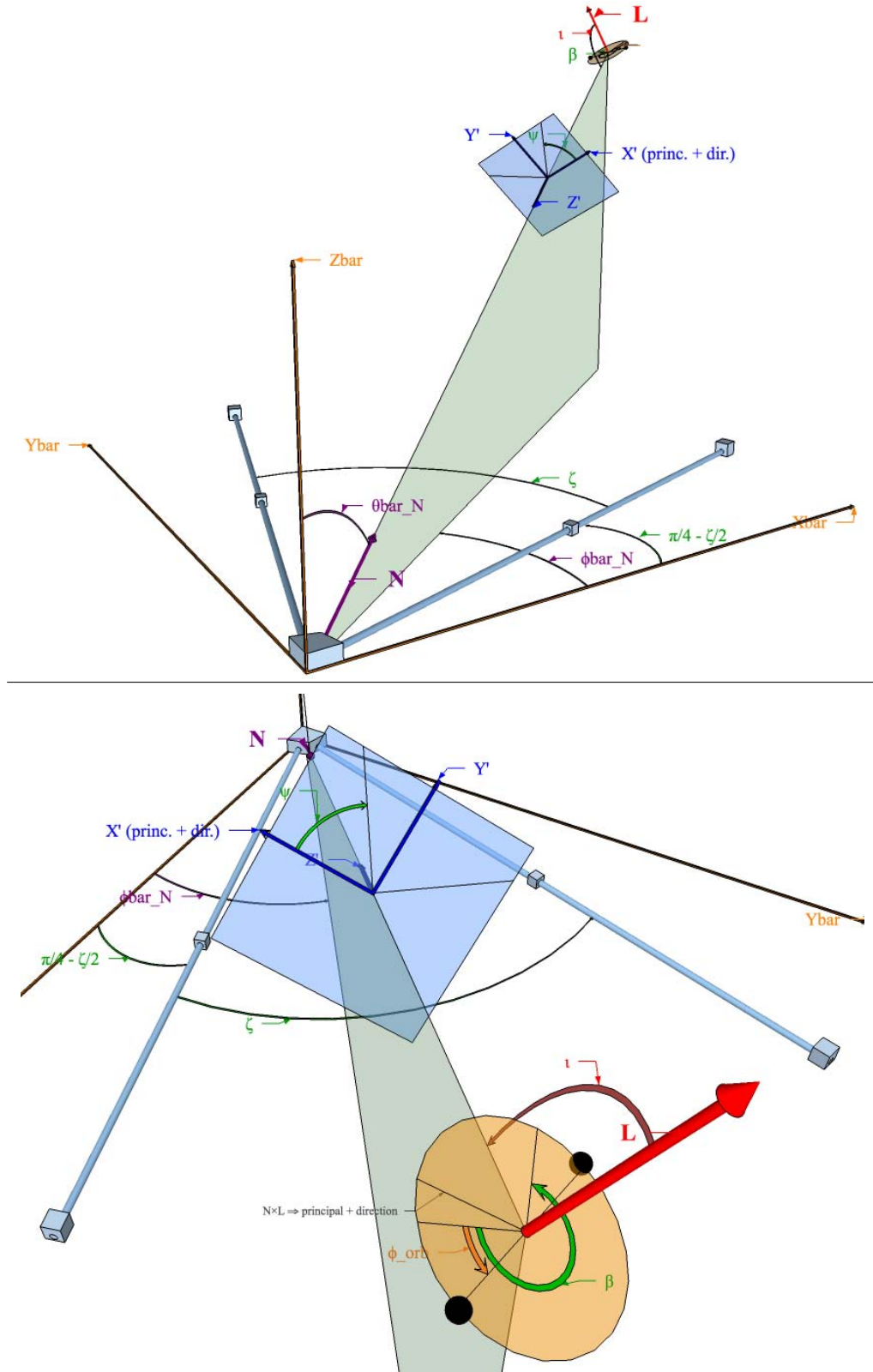
Figure 2.1: Two different perspectives from a 3-dimensional diagram representing the most useful co-ordinates systems and angles to describe the generation *(source coordinate system)*, propagation *(wave Cartesian coordinate system, $\{x', y', z'\}$)* and detection *(frame $\{\overline{x}, \overline{y}, \overline{z}\}$ attached to the GW detector)* of GW signals. [Diagrams: own production]

Eq. (2.31) and, in matrix form

$$H' = \left[\begin{array}{ccc} h_+ & h_\times & 0 \\ h_\times & -h_+ & 0 \\ 0 & 0 & 0 \end{array} \right] . \tag{2.33}$$

- $\{\overline{x}, \overline{y}, \overline{z}\}$ is a reference frame attached to the *GW detector*, having the detector's plane contained inside the $\overline{x} - \overline{y}$ plane and the $\overline{z}$ axis pointing toward zenith. Following Cutler's [3] criterion, the two detector's arms, assumed to form an arbitrary angle ζ; are "symmetrically placed" inside the $\overline{x} - \overline{y}$ axes (see Fig. 2.1), *i.e.* both, detector's arms and $\overline{x} - \overline{y}$ axes, share the angle bisector.

- Finally, $\{x, y, z\}$ is an ecliptic Cartesian coordinates system centered at the SSB and with the $x - y$ plane tied to the ecliptic (*i.e.* the plane of the Earth's motion around the Sun). The x axis points toward an arbitrary but fixed direction in the sky and z is chosen in order to have the Earth's angular momentum around the Sun to be parallel to the $+z$ direction.

2.2.1 Gravitational wave strain in the detector's coordinates frame

In Fig. 2.1 we represent $\{x', y', z'\}$ and $\{\overline{x}, \overline{y}, \overline{z}\}$ frames and the relevant angles that take part in the coordinates transformation. In particular, the 3-dimensional orthogonal matrix of transformation, M, (from the wave Cartesian coordinates $\{x', y', z'\}$ to the Cartesian coordinates $\{\overline{x}, \overline{y}, \overline{z}\}$ in the detector's proper frame) can be expressed as a composition of Euler rotations [14] within the Z-Y-Z form (the most common convention in GW data analysis). Moreover, since z' is parallel to the $-\hat{\mathbf{N}}$ vector, it turns out that the $\{\theta, \phi\}$ Euler angles of transformation from $\{\overline{x}, \overline{y}, \overline{z}\}$ to $\{x', y', z'\}$, coincide (modulo π) with the polar angles, $\{\overline{\theta}_N, \overline{\phi}_N\}$, of the unit vector $\hat{\mathbf{N}}$ in the detector's reference frame. The third Euler angle, ψ, is the *polarization angle* and is the angle (see Ref. [2]) from the principal direction of the '+' polarization: $\pm\hat{\mathbf{N}} \times \hat{\mathbf{L}}$; to the direction of constant azimuth ($\overline{\phi}_N$) over the $x' - y'$ plane: $\pm\hat{\mathbf{N}} \times (\hat{\mathbf{N}} \times \overline{\hat{\mathbf{z}}})$, where $\overline{\hat{\mathbf{z}}}$ is the unit vector parallel to the $\overline{z}$ axis. Since ψ is defined as an angle between two directions, it will be modulo π and we arbitrarily set it to be $\psi \in [0, \pi]$, *i.e.* its sine is positive defined. Making use of the properties of the scalar and vectorial products between vectors in a 3-dimensional Cartesian space, we obtain the following scalar expressions to determine the polarization angle:

$$\cos\psi = \hat{\mathbf{N}} \cdot (\hat{\mathbf{L}} \times \overline{\hat{\mathbf{z}}}) \quad , \quad \sin\psi = |\hat{\mathbf{L}} \cdot \overline{\hat{\mathbf{z}}} - (\hat{\mathbf{L}} \cdot \hat{\mathbf{N}})(\overline{\hat{\mathbf{z}}} \cdot \hat{\mathbf{N}})| . \tag{2.34}$$

With this, the orthogonal matrix that transforms $\{x', y', z'\} \mapsto \{\bar{x}, \bar{y}, \bar{z}\}$, M, can be expressed as the product of three Euler rotation matrices[5] [14]:

$$M = R_z(-\overline{\phi}_N) \cdot R_y(-\overline{\theta}_N + \pi) \cdot R_z(\psi)$$

$$= \left[\begin{array}{ccc} \cos(-\overline{\phi}_N) & -\sin(-\overline{\phi}_N) & 0 \\ \sin(-\overline{\phi}_N) & \cos(-\overline{\phi}_N) & 0 \\ 0 & 0 & 1 \end{array} \right] \cdot \left[\begin{array}{ccc} \cos(-\overline{\theta}_N + \pi) & 0 & \sin(-\overline{\theta}_N + \pi) \\ 0 & 1 & 0 \\ -\sin(-\overline{\theta}_N + \pi) & 0 & \cos(-\overline{\theta}_N + \pi) \end{array} \right] \cdot \left[\begin{array}{ccc} \cos\psi & -\sin\psi & 0 \\ \sin\psi & \cos\psi & 0 \\ 0 & 0 & 1 \end{array} \right]$$

$$= \left[\begin{array}{ccc} -\cos\overline{\phi}_N \cos\overline{\theta}_N \cos\psi + \sin\overline{\phi}_N \sin\psi & \sin\overline{\phi}_N \cos\psi + \cos\overline{\phi}_N \cos\overline{\theta}_N \sin\psi & \cos\overline{\phi}_N \sin\overline{\theta}_N \\ \sin\overline{\phi}_N \cos\overline{\theta}_N \cos\psi + \cos\overline{\phi}_N \sin\psi & \cos\overline{\phi}_N \cos\psi - \sin\overline{\phi}_N \cos\overline{\theta}_N \sin\psi & -\sin\overline{\phi}_N \sin\overline{\theta}_N \\ -\sin\overline{\theta}_N \cos\psi & \sin\overline{\theta}_N \sin\psi & -\cos\overline{\theta}_N \end{array} \right] . \tag{2.35}$$

---

[5]Note that since $\hat{\mathbf{N}} = -\hat{\mathbf{z}}'$, the angles appearing in the rotation matrices are not the trivial ones.

In the *detector's Cartesian coordinate system* $\{\overline{x}, \overline{y}, \overline{z}\}$, the 3-dimensional matrix of the spatial perturbation produced by the wave can be expressed as a coordinates transformation of the GW signal in the wave's frame, H', written in Eq. (2.33):

$$\overline{H} = M \cdot H' \cdot M^T \ , \tag{2.36}$$

and the unit vectors parallel to the arms, $\overline{\hat{\mathbf{n}}}_1$ and $\overline{\hat{\mathbf{n}}}_2$, can be straightforwardly written as

$$\overline{\hat{\mathbf{n}}}_1 = \begin{bmatrix} \cos(\frac{\pi}{4} - \frac{\zeta}{2}) \\ \sin(\frac{\pi}{4} - \frac{\zeta}{2}) \\ 0 \end{bmatrix} \qquad \overline{\hat{\mathbf{n}}}_2 = \begin{bmatrix} \sin(\frac{\pi}{4} - \frac{\zeta}{2}) \\ \cos(\frac{\pi}{4} - \frac{\zeta}{2}) \\ 0 \end{bmatrix} \ . \tag{2.37}$$

With this, we have all the quantities needed to compute the measured scalar GW strain in the interferometer, $h(t)$ [see Eq. (2.32)], expressed in the very same coordinates, $\{\overline{x}, \overline{y}, \overline{z}\}$. Putting Eqs. (2.32)-(2.37) together, we obtain the following final expression for $h(t)$

$$h(t; \boldsymbol{\lambda}_{\mathrm{src}}, \hat{\mathbf{N}}, \iota, \psi, \zeta) = F_+(t; \hat{\mathbf{N}}, \psi, \zeta) \, h_+(\tau(t); \boldsymbol{\lambda}_{\mathrm{src}}, \iota) + F_\times(t; \hat{\mathbf{N}}, \psi, \zeta) \, h_\times(\tau(t); \boldsymbol{\lambda}_{\mathrm{src}}, \iota) \ , \tag{2.38}$$

where we recall that $h_{(+,\times)}$ are the orthogonal polarizations given in Eq. (2.26), and

$$\begin{aligned} F_+(t; \hat{\mathbf{N}}, \psi, \zeta) &= \sin\zeta \left[\tfrac{1}{2}(1 + \cos^2\overline{\theta}_{\mathrm{N}}) \cos(2\overline{\phi}_{\mathrm{N}}) \cos(2\psi) - \cos\overline{\theta}_{\mathrm{N}} \sin(2\overline{\phi}_{\mathrm{N}}) \sin(2\psi) \right] \\ F_\times(t; \hat{\mathbf{N}}, \psi, \zeta) &= -\sin\zeta \left[\tfrac{1}{2}(1 + \cos^2\overline{\theta}_{\mathrm{N}}) \cos(2\overline{\phi}_{\mathrm{N}}) \sin(2\psi) + \cos\overline{\theta}_{\mathrm{N}} \sin(2\overline{\phi}_{\mathrm{N}}) \cos(2\psi) \right] \end{aligned} \tag{2.39}$$

are the so-called *antenna beam patterns* and they depend on the sky position of the GW source $[\overline{\theta}_{\mathrm{N}}(t), \overline{\phi}_{\mathrm{N}}(t)]$, the polarization angle $[\psi(t)]$ and the angle between the two interferometer's arms $[\zeta]$. Notice that having the interferometer's arms with an angle smaller than 90°, *i.e.* $\zeta > 0$, is equivalent as having a 90° arms with an effective length equal to $L\sin\zeta$. In other articles, for instance Ref. [2, 3], the explicit minus sign that we are finding in front of $F_\times$ is absorbed in the definition of $h_\times$, Eqs. (2.17) or (2.26), moving the explicit minus sign from $F_\times$ to $h_\times$; in any case the final expression for measured strain is identical.

Making use of the straightforward properties:

(i) $\quad F_+(\psi' = \frac{\pi}{4} + \psi) = F_\times(\psi) \quad$ and $\quad$ (ii) $\quad F_{+,\times}(\frac{\pi}{2} + \psi) = -F_{+,\times}(\psi) \ \ ;$

we represent in Figs. 2.2 and 2.3 the plots of the *antenna beam pattern* functions (in absolute value) over the sky for a single 90° arms' detector and considering several values of the angle ψ. Notice that, in each hemisphere, there are two [approximated] azimuthal and orthogonal directions where the detector is most sensitive and two directions [rotated $\pi/4$ with respect to the first ones] where the sensitivity is minimum. Indeed, these angles can be obtained analytically; in particular for the $|F_\times|$ function, the maxima for the zenith $[\overline{\theta} = 0]$ and nadir $[\overline{\theta} = \pi]$ are found at $\overline{\phi}_{\overline{\theta}=0} = -\psi + \frac{\pi}{4} + n\frac{\pi}{2}$ and $\overline{\phi}_{\overline{\theta}=\pi} = \psi + \frac{\pi}{4} + n\frac{\pi}{2}$, respectively, n being an integer number. [The minima are rotated $\pi/4$ with respect to these directions.] Notice that the angle difference between the maxima directions at the nadir and the zenith is $(\overline{\phi}_{\overline{\theta}=\pi} - \overline{\phi}_{\overline{\theta}=0}) = \mathrm{mod}_{\frac{\pi}{2}}(2\psi)$; as it can be seen in Figs. 2.2 and 2.3.
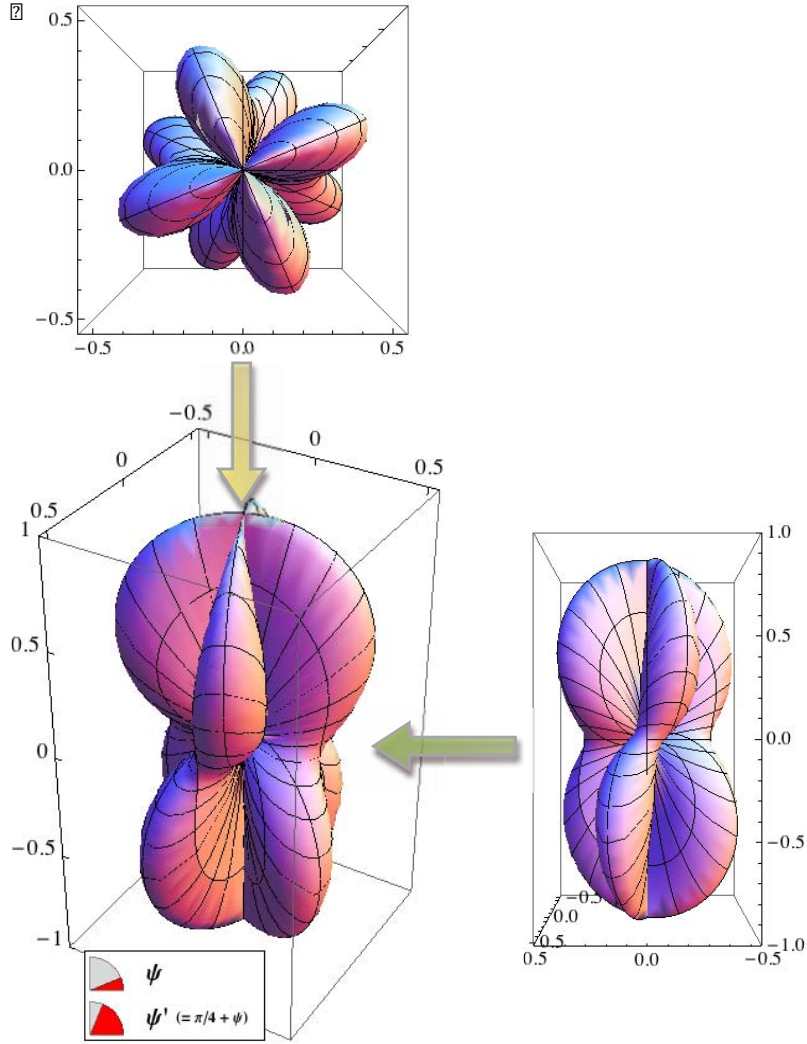
Figure 2.2: Plot of a single detector's *antenna beam pattern* function (in absolute value) over the sky from three different view angles. In particular, we are plotting the following two equivalent functions of the spherical angles: $|F_\times(\bar{\theta},\bar{\phi},\psi = \frac{\pi}{8},\zeta = \frac{\pi}{2})| = |F_+(\bar{\theta},\bar{\phi},\psi' = \frac{3\pi}{8},\zeta = \frac{\pi}{2})|$. [Plot: own production]

| $\psi = 0$ | $\psi = \frac{\pi}{12}$ | $\psi = \frac{\pi}{6}$ | $\psi = \frac{\pi}{4}$ | $\psi = \frac{\pi}{3}$ | $\psi = \frac{5\pi}{12}$ | $\psi = \frac{\pi}{2}$ or 0 |
| $\psi' = \frac{\pi}{4}$ | $\psi' = \frac{\pi}{3}$ | $\psi' = \frac{5\pi}{12}$ | $\psi' = \frac{\pi}{2}$ or 0 | $\psi' = \frac{\pi}{12}$ | $\psi' = \frac{\pi}{6}$ | $\psi' = \frac{\pi}{4}$ |
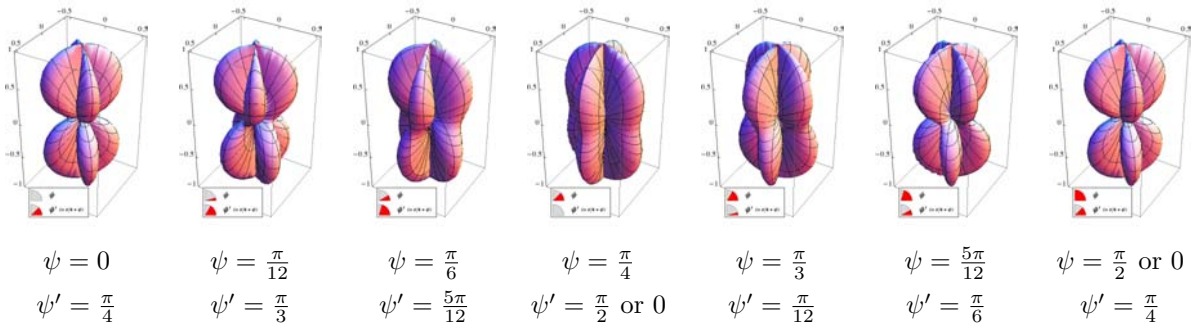
Figure 2.3: Sequence of graphical representations of the *antenna beam patterns* functions (in absolute value) for a single 90° arms' detector, $|F_\times(\psi)| = |F_+(\psi' = \frac{\pi}{4} + \psi)|$ [see Eq. (2.39) and Fig. 2.2], plotted over the sky and for different values of the polarization angle ψ. Since, $F_{+,\times}(\frac{\pi}{2} + \psi) = F_{+,\times}(\psi)$ we just represent the interval $\psi \in [0, \frac{\pi}{2}]$. [Plots: own production]

2.2.2 Change of apparent sky location and polarization due to detector's motion

Equation (2.38) represents the general expression of the measured GW strain in an interferometric detector in the long wavelength approximation (LWA). This result is written in terms of angles measured at the detector's Cartesian coordinate system, which follows the detector's movement around the Sun; thus, the "barred" angles $\{\overline{\theta}_{\rm N}, \overline{\phi}_{\rm N}, \psi\}$ will change over the observation time when this is long enough (ζ is constant). In particular, ground-based detectors are expected to only observe the late inspiral and merger parts of the CBC evolution, which represents, at most, the last ~ 200 cycles of the GW signal. Since the lowest frequency that ground-based detectors can observe is ≈ 20 Hz, this means that the longest[6] CBC signal observed in Earth will last 10 sec, over which the Earth's motion can be completely neglected. Thus, for *ground-based observations of CBC signals*, the antenna beam patterns can be considered as *constant functions in time*, that only depend on the particular interferometer and date time of the observation at hand. For long-lived sources, such as the stochastic background and the gravitational emission of rapidly spinning pulsars, the antenna beam patterns become a time dependent functions that provide information about the sky location of the source. We refer the reader to Ref. [12] for a detailed explanation about how to include the Earth's motion in long-lived GW signals for ground-based detectors.

The LISA case, however, is a completely different story; mainly for two reasons. First, because LISA will observe a much lower frequency window, $[10^{-5}, 0.1]$ Hz, but keeping the same intrinsic orbital period of 1 yr, since LISA is following the Earth in its motion around the Sun; this means that the same 200 GW cycles would last up to ≈ 8 months. Second, because LISA will observe CBC signals coming from supermassive black-hole systems with signal-to-noise ratios of several hundreds, which means that it can observe signals that are still far from the merger (inspiral-only signals), which may span several thousands of cycles [this is the case, for instance, of the inspiral signals that we shall study in Chapters 4 and 5 and the galactic binaries of Chapter 6]. Thus, LISA observations of CBC may last the whole mission life-time and therefore we must consider the detector's motion around the Sun. This problem has been studied in detail by Cutler [3] and here we just quote their main results [making a careful conversion between their and our notation] that explicitly express the time dependence of the "barred" angles $\{\overline{\theta}_{\rm N}, \overline{\phi}_{\rm N}, \psi\}$ in terms of the constant angles measured from the SSB.

$$\cos\overline{\theta}_{\rm N}(t; \hat{\mathbf{N}}, \boldsymbol{\lambda}_{\rm LISA}) = \frac{1}{2}\cos\theta_{\rm N} - \frac{\sqrt{3}}{2}\sin\theta_{\rm N}\,\cos[\phi_{\rm LISA}(t; \boldsymbol{\lambda}_{\rm LISA}) - \phi_{\rm N}]\,,\text{and} \qquad (2.40)$$

$$\overline{\phi}_{\rm N}(t; \hat{\mathbf{N}}, \boldsymbol{\lambda}_{\rm LISA}) = \alpha_0 + \frac{2\pi t}{T_{\rm LISA}} + \arctan\left(\frac{\sqrt{3}\cos\theta_{\rm N} + \sin\theta_{\rm N}\,\cos[\phi_{\rm LISA}(t; \boldsymbol{\lambda}_{\rm LISA}) - \phi_{\rm N}]}{2\sin\theta_{\rm N}\,\sin[\phi_{\rm LISA}(t; \boldsymbol{\lambda}_{\rm LISA}) - \phi_{\rm N}]}\right)\,,$$
$$(2.41)$$

where $T_{\rm LISA} = 1$ yr represents LISA's orbital period, $\phi_{\rm LISA}(t; \boldsymbol{\lambda}_{\rm LISA}) = \phi_{\rm LISA, 0} + \frac{2\pi t}{T_{\rm LISA}}$ is the angular position of LISA over its orbital plane, and $\phi_{\rm LISA, 0}$ and α_0 are just constants specifying, respectively, the detector's location in the orbital plane and the orientation of the arms at time $t = 0$.

---

[6]These are very conservative numbers. In reality typical CBC observations in ground-based GW detectors will last fractions of a second.

Finally, the polarization angle, $\psi(t; \hat{\mathbf{N}}, \hat{\mathbf{L}}, \boldsymbol{\lambda}_{\mathrm{LISA}})$, can be computed from its scalar definition in Eq. (2.34), taking into account that the vectors that appear in there can be expressed in the SSB reference frame as,

$$
\hat{\mathbf{N}} = \begin{bmatrix} \sin\theta_{\mathrm{N}} \cos\phi_{\mathrm{N}} \\ \sin\theta_{\mathrm{N}} \sin\phi_{\mathrm{N}} \\ \cos\theta_{\mathrm{N}} \end{bmatrix} ; \quad \hat{\mathbf{L}} = \begin{bmatrix} \sin\theta_{\mathrm{L}} \cos\phi_{\mathrm{L}} \\ \sin\theta_{\mathrm{L}} \sin\phi_{\mathrm{L}} \\ \cos\theta_{\mathrm{L}} \end{bmatrix} ; \quad \bar{\bar{\mathbf{z}}} = \begin{bmatrix} -\frac{\sqrt{3}}{2} \cos\phi_{\mathrm{LISA}}(t; \boldsymbol{\lambda}_{\mathrm{LISA}}) \\ -\frac{\sqrt{3}}{2} \sin\phi_{\mathrm{LISA}}(t; \boldsymbol{\lambda}_{\mathrm{LISA}}) \\ \frac{1}{2} \end{bmatrix} ,
$$
$$(2.42)$$

where one has used the fact that the normal to the detector plane, $\bar{\bar{\mathbf{z}}}$, is at a constant $60°$ angle to $\hat{\mathbf{z}}$, and $\bar{\bar{\mathbf{z}}}$ precesses around $\hat{\mathbf{z}}$ at a constant rate. The explicit expressions for 'sin ψ' and 'cos ψ' can be found in Eqs. (3.19)-(3.22) of Ref. [3].

2.2.3   Doppler shift due to relativistic effects and relative motion source − detector

All the expressions for the emitted GW signal derived in Sec. 2.1 are given in terms of the proper timing of the source's barycenter reference frame, $\tau \equiv \tau_e$. Thus, we must consider the relativistic effects that link this proper time of emission, τ_e, to the proper time of arrival, τ_a, at the detector's reference frame. In order to do so, we shall make use of the knowledge acquired in the 1980s about 'timing' relations when studying the experimental data from the binary pulsar PSR 1913+16; in particular we shall use as reference the articles [15, 16].

Assuming a system of harmonic coordinates at rest with respect to the SSB, the 'timing formula' linking the proper time of emission, τ_e, to the coordinate time of arrival at the detector, $\bar{t}_a$, can be written as [15, 16]

$$
D \, \tau_e = \bar{t}_a - \Delta_S + \frac{\mathbf{r}_{\mathrm{IFO}} \cdot \hat{\mathbf{N}}}{c} + \Delta_{E,\odot} - \frac{D_L}{c} \ . \tag{2.43}
$$

Here, Δ_S denotes the general-relativistic Shapiro time-delay due to the propagation of the GW signal in a curved space-time caused by any gravitational field in the path between the source and the detector (*e.g.* the Sun); $\mathbf{r}_{\mathrm{IFO}} \cdot \hat{\mathbf{N}}/c$ is the (coordinate) Roemer time-delay, *i.e.* the travel time along $\mathbf{r}_{\mathrm{IFO}} \equiv \mathbf{r}_{\mathrm{IFO}}(t)$, from the SSB to the detector; and $\Delta_{E,\odot}$ is the so-called Einstein time-delay in the solar system, which represents a combined effect of gravitational redshift and time dilation due to motions of the Earth and other bodies [16]. The last term in the expression is just a *constant* distance between the source barycenter and the SSB at a given time, since all the time dependency of the distance separation between the two barycenters is included in the Doppler factor, D, [15]

$$
D \equiv \frac{1 + \frac{\mathbf{v}_{\mathrm{src}} \cdot \hat{\mathbf{N}}}{c}}{\sqrt{1 - \frac{\mathbf{v}_{\mathrm{src}}^2}{c^2}}} = \gamma \left(1 + \frac{\mathbf{v}_{\mathrm{src}} \cdot \hat{\mathbf{N}}}{c}\right) \equiv (1 + z) \ , \tag{2.44}
$$

where z is simply the *redshift*.

The effects of both Shapiro and Einstein time-delays are generally much smaller than the Newtonian Roemer-delay, and therefore the 'timing relation' used in GW data analysis of signals from the High- and Low-Frequency bands is simply

$$
D \, \tau_e = \bar{t}_a + \frac{\mathbf{r}_{\mathrm{IFO}} \cdot \hat{\mathbf{N}}}{c} + \mathrm{const.} \tag{2.45}
$$

This relation has basically two effects on the measured GW signal:

- On one hand, we are measuring *redshifted* time and frequency quantities; *i.e.* the observed measurements will be related to the physical ones (as measured in the source reference frame) as follows:

$$t_{obs} = (1 + z)\, t_{phys} \qquad ; \qquad f_{obs} = \frac{f_{phys}}{1 + z} \, ,$$

where we recall that $(1 + z) \equiv D$. Given the fact that all the CBC dynamics is formulated in terms of the adimensional time and frequency variables, t/M and fM, respectively (see Chapter 3); this redshift effect is normally absorbed by defining *observed redshifted masses*, which are related to the physical ones simply as

$$m_{obs} = (1 + z)\, m_{phys} \, , \tag{2.46}$$

'm' being any dimensionful mass, *i.e.* total mass M, mass difference δm, individual masses $\{m_1, m_2\}$, reduced mass μ, or chirp mass $\mathcal{M}$. Of course, the dimensionless mass quantities, such as the mass ratio q or the symmetric mass ratio ν, are *not* redshifted.

- On the other hand, the Roemer time-delay will produce a *Doppler shift* in the observed GW phase, that generally can be represented as

$$\phi_{\text{GW}}(\tau) = \phi_{\text{GW}}(\tau(\bar{t}_a)) = \phi_{\text{GW}}\left(\tfrac{\bar{t}_a + \mathbf{r}_{\text{IFO}} \cdot \hat{\mathbf{N}}/c}{D}\right) \, . \tag{2.47}$$

  - For *low frequency signals* (such as LISA band), the GW phase does not change very much during the travel time along $\mathbf{r}_{\text{IFO}}$, which makes possible to series expand ϕ_{GW} and represent the Doppler-shift effect as an additive phase:

$$\phi_{\text{GW}}(\tau) = \phi_{\text{GW}}\left(\tfrac{\bar{t}_a}{D}\right) + \frac{\mathbf{r}_{\text{IFO}} \cdot \hat{\mathbf{N}}}{c}\, \dot{\phi}_{\text{GW}}\left(\tfrac{\bar{t}_a}{D}\right) + \mathcal{O}\left[\tfrac{r_{\text{IFO}}}{c}\right]^2 \simeq \phi_{\text{GW}} + \varphi_{\text{D}} \, , \tag{2.48}$$

where we have neglected second-order Doppler corrections since they are of order $(\mathrm{v}_{\text{IFO}}/c)|\varphi_{\text{D}}(t)| \lesssim 3 \times 10^{-4}(f/10^{-3})$ rad [3]. The dot denotes a time-derivative in the detector's reference frame (*i.e.* with respect to $\bar{t}$) and the Doppler phase φ_{D} is defined as

$$\varphi_{\text{D}}(t) = \frac{2\pi F(t)}{c}\, \mathbf{r}_{\text{IFO}} \cdot \hat{\mathbf{N}} \, , \tag{2.49}$$

where $F(t) \equiv \frac{\dot{\phi}_{\text{GW}}(t)}{2\pi}$ is the (redshifted) GW frequency.

Making use of the explicit expression for the position of the LISA detector as a function of time [3],

$$\mathbf{r}_{\text{LISA}}(t) = R_{\text{LISA}} \begin{bmatrix} \cos\phi_{\text{LISA}}(t) \\ \sin\phi_{\text{LISA}}(t) \\ 0 \end{bmatrix} \, , \tag{2.50}$$

where $R_{\text{LISA}} = 1$ AU and $\phi_{\text{LISA}}(t)$ is the angular position of LISA over its orbital plane [see paragraph right after Eq. (2.41)]; one can get an explicit expression for the Doppler phase for LISA [3]:

$$\varphi_{\text{D, LISA}}(t) = \frac{2\pi F(t)}{c}\, R_{\text{LISA}} \sin\theta_{\text{N}}\, \cos(\phi_{\text{LISA}}(t) - \phi_{\text{N}}) \, . \tag{2.51}$$

– For *higher frequency signals* (*e.g.* ground-based detectors band), one can not use the expansion in (2.48), although similar expressions can be obtained when the explicit time dependency of the phase is known; see, for instance, the derivation in Appendix A of [12] for GW signals from spinning NSs.

2.3   Putting all pieces together: measured GW strain as a sum of cosine functions

In this chapter we have gone from the raw output of a numerical simulation, or a PN calculation (the Regge-Wheeler and Zerilli functions, $\Psi_{\ell m}^{(o)}$ and $\Psi_{\ell m}^{(e)}$), to the very 'end product', this is the time series GW strain measured in the detector, $h(t)$. The process can be summarized in two steps; first, an expansion over the spin-weighted spherical harmonics that provide the GW components with the corresponding angular dependency, here is where we have defined the $(\hat{u}, \hat{w})_{(+,\times),m}$ functions that expand h_+ and $h_\times$ in terms of harmonics of the GW phase; and second, a projection of the GW spatial tensor into the detector's frame, which has defined the *antenna beam patterns* and has added the dependency on the sky location and the detector's motion to the measured signal, $h(t)$.

At this point, it is time to place everything in order and to write explicitly the general expression for a time-domain GW signal emitted by a CBC and measured by an interferometric GW detector. This is, indeed, the purpose of this section.

Let us start considering the *restricted PN approximation*, where h_+ and $h_\times$ are given by Eq. (2.17); the former containing just a '$\cos \phi_{\rm GW}$' and the latter with a sine of the same phase. Making use of the general expression for the measured differences between the wave-induced relative length of the two interferometer arms, Eq. (2.38), and basic trigonometric relations, one can write $h(t; \boldsymbol{\lambda}_{\rm src}, \hat{\mathbf{N}}, \iota, \psi, \zeta) \equiv h(t)$ as

$$
\begin{aligned}
h(t) &= \left[\frac{1 + \cos^2 \iota}{2}\right] F_+ \, a_{\rm N} \, \cos(\phi_{\rm GW} + \varphi_{\rm D}) + [\cos \iota] \, F_\times \, a_{\rm N} \sin(\phi_{\rm GW} + \varphi_{\rm D}) \\
&\equiv \mathcal{C}_p \, a_{\rm N} \cos(\phi_{\rm GW} + \varphi_p + \varphi_{\rm D}) \,,
\end{aligned} \tag{2.52}
$$

where

$$
\mathcal{C}_p \equiv \frac{1}{2}\sqrt{(1 + \cos^2 \iota)F_+^2 + 4\cos^2 \iota F_\times^2} \,, \tag{2.53}
$$

$$
\varphi_p \equiv \arctan\left[\frac{-2F_\times \cos \iota}{F_+(1 + \cos^2 \iota)}\right] \,. \tag{2.54}
$$

The subscript 'p' stands for *polarization* and φ_p is called *polarization phase*. If we were considering observations from multiple detectors, the amplitude and phase differences between the various detected strains would involve different $\mathcal{C}_p$ and φ_p values through the antenna beam patterns of each detector, and therefore we could infer the sky location $\{\theta_{\rm N}, \phi_{\rm N}\}$ and polarization angle ψ of the source. Also, if we are observing a GW signal for a long time period (*e.g.* CBCs with LISA), the time dependence of these two values, $\mathcal{C}_p$ and φ_p, can be used to estimate the position of the source. Finally, if one considers short-lived signals detected by a single interferometer, $\mathcal{C}_p$ and φ_p will be numerical constants and absorbed, respectively, into an effective distance, $D_{\rm eff} \equiv D_L/\mathcal{C}_p$ [where D_L is the luminosity distance] and the arbitrary initial phase of the signal, $\phi_0 \equiv \phi_{\rm GW}(t = 0)$.

A similar derivation can be done for the general case, where $h(t)$ is written as the superposition of different harmonics of the orbital phase, see Eq. (2.26). Let us recall that usually, in the data analysis articles, the different harmonics are denoted with the letter j instead of the m used in Sec. 2.1 [see Eq. (2.30)]. In this case, one shall find a different factor $\mathcal{C}_{p,j}$ and polarization phase, $\varphi_{p,j}$, for each harmonic:

$$
\begin{aligned}
h(t) &= a_{\mathrm{N}} \sum_{j=0}^{\infty} \Upsilon_j \left[(F_+ \hat{u}_{+,j} + F_\times \hat{u}_{\times,j}) \cos(\tfrac{j}{2}\phi_{\mathrm{GW}} + \varphi_{\mathrm{D}}) + (F_+ \hat{w}_{+,j} + F_\times \hat{w}_{\times,j}) \sin(\tfrac{j}{2}\phi_{\mathrm{GW}} + \varphi_{\mathrm{D}}) \right] \\
&\equiv a_{\mathrm{N}} \sum_{j=0}^{\infty} \Upsilon_j \, \mathcal{C}_{p,j} \cos(\tfrac{j}{2}\phi_{\mathrm{GW}} + \varphi_{p,j} + \varphi_{\mathrm{D}}) ,
\end{aligned} \tag{2.55}
$$

where

$$
\mathcal{C}_{p,j} \equiv \sqrt{(F_+ \hat{u}_{+,j} + F_\times \hat{u}_{\times,j})^2 + (F_+ \hat{w}_{+,j} + F_\times \hat{w}_{\times,j})^2} , \tag{2.56}
$$

$$
\varphi_{p,j} \equiv \arctan\left[\frac{-(F_+ \hat{w}_{+,j} + F_\times \hat{w}_{\times,j})}{(F_+ \hat{u}_{+,j} + F_\times \hat{u}_{\times,j})} \right] . \tag{2.57}
$$

Here is where the benefits of factorizing the common terms out of $(u,w)_{(+,\times),j}$ become relevant since (i) a_{N} appears in the explicit expression of $h(t)$ carrying the units and order of magnitude of the amplitude and (ii) the Υ_j functions cancel out in the definition of the polarization phase, which shall prevent potential numerical divergencies in cases where δm or ι are close to zero [see Eqs. (2.29)].

Let us notice that, both in Eqs. (2.54) and (2.57), the sign of the fraction inside the 'arctan' function is explicitly written in the numerator in order to remove the $\mathrm{mod}(\pi)$ degeneracy of the polarization phase, by making explicit that the sign of 'sin $\varphi_{p,j}$' is the sign of the numerator, and the same for 'cos $\varphi_{p,j}$' and the denominator. Sometimes, this two-argument 'arctan' function is called "atan2".

2.4 Residual gauge-freedom in the measured GW strain

The measured GW strain depends on a lot of parameters. Some of them, such as $\{\boldsymbol{\lambda}_{\mathrm{IFO}}, \zeta\}$ are fixed by the detector's geometry and motion; others, such as $\boldsymbol{\lambda}_{\mathrm{src}}$ depend only on the physical properties of the source; and finally, $\{\hat{\mathbf{N}}, \phi_0, \iota, \psi\}$ depend on the relative orientation of the detector with respect to angular momentum of the compact binary. It is, precisely, this last set of parameters, the ones that explicitly appear in the relation between the measured $h(t)$ and the emitted spherical harmonics components $h_{\ell m}$, and they contain some residual gauge-freedom (symmetries) that will make the measured GW strain [approximately] invariant under certain transformations of these parameters.

Studying and restricting this residual gauge-freedom in $h(t)$ is essential in order to remove equivalences or degeneracies between different regions of the parameter space. We shall see that some of the symmetries are exact, and therefore we shall be talking about *equivalence* between different regions; whereas some of them will be valid just as a limit case or approximately, in this case, we shall talk about *degeneracies* in the parameter space. The benefits of detecting such symmetries are two-fold; on the one hand, by finding two *equivalent* regions of the parameter space, one shall be able to restrict the range of some the parameters and therefore, to reduce the search volume of parameter space; on the

other hand, knowing before-hand about the existence of *degeneracies* in the parameter spaces will help understanding the results out from a blind search, as well as improving the search method itself.

We shall analyze the symmetries of each of the functions that take part into the calculation of $h(t)$, making always clear whether they are valid in general or simply under certain circumstances. After that, we shall combine these symmetries in order to obtain the different invariant transformations.

- Let us start by the general and formally proven [see Eq. (2.24)] symmetry relation that satisfy h_+ and $h_\times$ with respect to the orientation angle, ι:

$$(1) \qquad \iota \to \pi - \iota \qquad , \qquad h_{\binom{+}{\times}} \to \pm h_{\binom{+}{\times}}$$

- Another symmetry related to the traveling GW signal that still does not involve the projection of the GW tensor in terms of the antenna beam patterns, is related with the arbitrary initial GW phase, ϕ_0,

$$(2) \qquad \phi_0 \to \phi_0 + \pi \qquad , \qquad h_{\binom{+}{\times}} \to -h_{\binom{+}{\times}}$$

However, this property (in the time-domain) is only valid for the $j = 2$ dominant harmonic, which is the only one not involving harmonics of ϕ_{GW}. Since the next dominant harmonics [4] are the $j = \{1, 3\}$ and $j = 4$, with amplitudes smaller than the $j = 2$ one by factors $\propto \mathrm{v}\frac{\delta m}{M}$ and $\propto \mathrm{v}^2$, respectively [$\mathrm{v} \ll 1$ being a PN expansion parameter]; we can consider (2) as a good approximation, although not strictly true.

- Finally, the rest of symmetry relations come from the antenna beam patterns. In particular, we shall write them schematically as two summands and then study how does their sign change for different transformations of the angles $\{\overline{\theta}_{\mathrm{N}}, \overline{\phi}_{\mathrm{N}}, \psi\}$,

$$F_+ = \sin\zeta \left[\tfrac{1}{2}(1 + \cos^2\overline{\theta}_{\mathrm{N}}) \cos(2\overline{\phi}_{\mathrm{N}}) \cos(2\psi) - \cos\overline{\theta}_{\mathrm{N}} \sin(2\overline{\phi}_{\mathrm{N}}) \sin(2\psi)\right] \equiv Ⓐ + Ⓑ \ ,$$
$$F_\times = -\sin\zeta \left[\tfrac{1}{2}(1 + \cos^2\overline{\theta}_{\mathrm{N}}) \cos(2\overline{\phi}_{\mathrm{N}}) \sin(2\psi) + \cos\overline{\theta}_{\mathrm{N}} \sin(2\overline{\phi}_{\mathrm{N}}) \cos(2\psi)\right] \equiv Ⓒ + Ⓓ \ .$$

Now, we consider all possible (but not repeated) angle transformations that change the signs in front of $\{Ⓐ, Ⓑ, Ⓒ, Ⓓ\}$, but do not swap between these terms. They are summarized in the following table:

		Ⓐ	Ⓑ	Ⓒ	Ⓓ
	original	+	+	+	+
(3)	$\psi \to \frac{\pi}{2} - \psi$	−	+	+	−
(4)	$\psi \to \frac{\pi}{2} + \psi$	−	−	−	−
(5)	$\overline{\theta}_{\mathrm{N}} \to \pi - \overline{\theta}_{\mathrm{N}}$	+	−	+	−
(6)	$\overline{\phi}_{\mathrm{N}} \to \frac{\pi}{2} - \overline{\phi}_{\mathrm{N}}$	−	+	−	+
(7)	$\overline{\phi}_{\mathrm{N}} \to \frac{\pi}{2} + \overline{\phi}_{\mathrm{N}}$	−	−	−	−

By combining (3)+(4) we would get that $\psi \to \pi - \psi$ gives $[+ - - +]$ and similar results could be obtained with (6)+(7) and (7)+(7); however we do not consider them in the previous table since they can be obtained from a combination of others already included. Indeed, given the dependency of $F_{+,\times}$ always with $2\overline{\phi}_{\mathrm{N}}$, we have

that the amplitudes are invariant under $\overline{\phi}_\mathrm{N} \to \pi + \overline{\phi}_\mathrm{N}$; this is (7)+(7). The same thing happens with the polarization angle, ψ.

The three angles that we are considering are measured in the time-varying "barred" reference system, which means that the symmetry relations may not be valid when one considers the constant "unbarred" angles, tied to the ecliptic reference frame $\{x, y, z\}$. Moreover, one must take into account that the angles characterizing the sky location of the source, $\hat{\mathbf{N}}$, also affect the signal's Doppler effect, which means there may be angle transformations that leave the amplitudes invariant, but change the phase and frequency of the observed signal. In particular,

- (3) and (4) will be valid when the signal (or most of the SNR) is observed for a short time [*e.g.* CBC observations with ground-based detectors (or signals including the merger with LISA)]; or the normal to the detector's plane, $\overline{\hat{\mathbf{z}}}$, is on average, during T_obs, parallel to the ecliptic's normal direction, $\hat{\mathbf{z}}$; which is the case of LISA. In the former, the symmetry will be valid for the instantaneous $\overline{\psi}$, whereas in the latter it will be for the invariant ψ.

- The dependency of the Doppler phase due to (5) is null if the perpendicular component to the ecliptic of the detector's velocity is zero or can be neglected. This is the case for LISA and a very good approximation for ground-based detectors, where the perpendicular component can only come from the daily spinning motion of the Earth; which, at most, can produce relative frequency changes of $\frac{\Delta f}{f} \sim 10^{-7}$. Thus, (5) will be valid in almost all typical cases considered in GW data analysis.

- (6) and (7), on the other hand, involve transformations on $\overline{\phi}_\mathrm{N}$ that do affect significatively the Doppler phase. This means that although the amplitudes may remain invariant, the observed phase will change unless it is compensated by also changing some of the source physical parameters $\boldsymbol{\lambda}_\mathrm{src}$ that can modify the GW phase, ϕ_GW. Thus, despite being transformations that may add *degeneracies* to the parameter space (as we shall see in practice in the following chapters), we won't consider them here as residual gauge-freedom.

Finally, let us note that there are also transformations that allow one to swap F_+ for $F_\times$; in particular the ones involving $\{\psi \to \frac{\pi}{4} \pm \psi \ ; \ \psi \to \frac{3\pi}{4} \pm \psi\}$. Also, by doing $\{\phi_0 \to \frac{\pi}{2} \pm \phi_0\}$ or $\{\phi_0 \to \frac{3\pi}{2} \pm \phi_0\}$, one can swap the 'sin ϕ_GW's for 'cos ϕ_GW's. However, we are not considering them because we found not possible to then have an equivalent transformation in ι to also swap u_+ for $w_\times$; and w_+ for $u_\times$; *i.e.* $\mathcal{S}^{\ell m}(\iota)$ for $\mathcal{D}^{\ell m}(\iota)$ [here, the pairs are chosen so that they share $h_{\ell m}^R$ or $h_{\ell m}^I$, see Eq. (2.27)].

With this, we find that symmetries (1)-(5), involving transformations on $\{\iota, \phi_0, \psi, \overline{\theta}_\mathrm{N}\}$, are valid in good approximation. We discard the transformations involving $\overline{\phi}_\mathrm{N}$, (6) and (7), because despite being valid for the amplitude terms, they also have a significant impact on the Doppler phase, that then should be compensated by modifying the source physical parameters, $\boldsymbol{\lambda}_\mathrm{src}$.

At the end of the day, those five symmetry relations just can be combined in the following two ways in order to leave the GW signal (2.38) invariant:

$$
\begin{aligned}
(a): & & (2)+(4) & \longrightarrow & \{\phi_0 \to \pi + \phi_0 \ ; \ \psi \to \tfrac{\pi}{2} + \psi\} & \\
(b): & \ (1)+(3)+(4)+(5) & \longrightarrow & \{\iota \to \pi - \iota \quad ; \ \psi \to \pi - \psi \quad ; \ \overline{\theta}_\mathrm{N} \to \pi - \overline{\theta}_\mathrm{N}\}
\end{aligned}
$$
$$(2.58)$$

We recall that the initial phase, ϕ_0, is defined in the $[0, 2\pi)$ range, whereas the other four angles $\{\iota, \psi, \overline{\theta}_{\mathrm{N}}\}$ are $\mathrm{mod}(\pi)$. Each of these two invariant transformations establish a one-to-one mapping between two halves of the parameter space. For instance, in Fig. 2.4 we exemplify the invariant transformation '(a)', involving the angles ϕ_0 and ψ. Any point in the quadrant I has its equivalent [i.e. that produces the same $h(t)$] in the quadrant III and the same happens between quadrants II and IV; thus we can say that quadrants I - III are equivalent and also II - IV. In light of these results, it is obvious that carrying a search over the entire parameter space, $\phi_0 \in [0, 2\pi)$ and $\psi \in [0, \pi]$, would be inefficient, since we would be considering all template waveforms twice.

Therefore, the invariant transformation '(a)' allows us to restrict one of the angles involved to half its original range. This represents reducing the volume of the parameter space [and also the computational time to explore it] by a factor 2. The same argument is applicable for '(b)'.
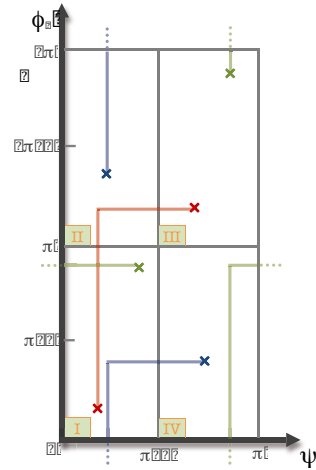
Figure 2.4: Diagram exemplifying how invariant transformation '(a)', $\{\phi_0 \to \pi + \phi_0; \psi \to \frac{\pi}{2} + \psi\}$, is translated into equivalence between different quadrants of the parameter space, in particular I $\leftrightarrow$ III and II $\leftrightarrow$ IV. [Plot: own production]

References

[1] B. Schutz, *A First Course in General Relativity*, Second Edition, (Cambridge University Press, Cambridge, England) (2009).

[2] T. A. Apostolatos *et al.*, Phys. Rev. D **49** 6274-6297 (1994).

[3] C. Cutler, Phys. Rev. D **57** 7089-7102 (1998).

[4] L. E. Kidder, Phys. Rev. D **77** 044016 (2008).

[5] A. Nagar, L. Rezzolla, Class. Quant. Grav. **22** R167 (2005).

[6] K. S. Thorne, Rev. Mod. Phys. **52** 299-339 (1980).

[7] M. Trias, A. M. Sintes, Phys. Rev. D **77** 024030 (2008).

[8] K. G. Arun *et al.*, Phys. Rev. D **76** 104016 (2007).

[9] K. G. Arun *et al.*, Phys. Rev. D **75** 124002 (2007).

[10] E. K. Porter, N. J. Cornish, Phys. Rev. D **78** 064005 (2008).

[11] M. Trias, A. M. Sintes, Class. Quant. Grav. **25** 184032 (2008).

[12] P. Jaranowski, A. Krolak, B. F. Schutz, Phys. Rev. D **58** 063001 (1998).

[13] M. Tinto, S. V. Dhurandhar, Living Rev. Rel. **8** 4 (2005) .

[14] L. D. Landau, E. M. Lifshitz, *Mechanics*, Third Edition, (Butterworth-Heinemann, Oxford, England) (1976)

[15] T. Damour, N. Deruelle, Ann. Inst. Henri Poincaré **44** 263-292 (1986).

[16] J. H. Taylor, J. M. Weisberg, Astrophys. J. **345** 434-450 (1989).

Chapter 3

Gravitational wave data analysis for Compact Binary Coalescences

3.1 Gravitational wave signals buried in noise

The signal described in the previous chapter will be buried in the noise of a detector. Thus, we are faced with the problem of detecting the signal and estimating its parameters from the noisy observed strain. By assuming additive noise, the output strain of a detector, $s(t)$, can be expressed as the sum of the GW signal characterized by the 'true' parameters $\boldsymbol{\lambda}_x$, $h_x(t, \boldsymbol{\lambda}_x)$ (here, and in the following, the subscript x stands for 'exact'), and the noise, $n(t)$;

$$s(t) = n(t) + h_x(t; \boldsymbol{\lambda}_x) . \tag{3.1}$$

The noise is also assumed to be *uncorrelated*, *stationary* and with *zero mean*; and it is characterized by its (one-sided) power spectral density (PSD), $S_n(f)$, which is defined as

$$\overline{\tilde{n}^*(f)\tilde{n}(f')} = \frac{1}{2} S_n(f)\delta(f - f') . \tag{3.2}$$

Here, the overline denotes the ensemble average, the superscript star indicates complex conjugation, $\delta(f)$ represents the Dirac's delta function and the tilde denotes the Fourier transform,

$$\tilde{n}(f) = \int_{-\infty}^{\infty} n(t)e^{-2\pi i f t}\mathrm{d}t . \tag{3.3}$$

Note that we use here the LSC sign convention for the Fourier transform, with a factor $\int \mathrm{d}t\, e^{-2\pi i f t}(...)$. This sign convention is what we shall use in Chapters 6 and 8; but opposite to what we use in our parameter estimation studies including higher harmonics of the inspiral signal (Chapter 4). In the literature, there are also discrepancies between the LSC sign convention and the one used in many early GW papers (such as Refs. [1–3]) which used the (theoretical-physics) convention $\int \mathrm{d}t\, e^{+2\pi i f t}(...)$.

According to this sign convention, the measured GW signal in the Fourier domain is usually represented in the following generic way,

$$\tilde{h}(f) \equiv A(f)e^{-i\psi(f)} , \tag{3.4}$$

where the amplitude $A(f)$ and the phase $\psi(f)$ are real quantities. [Notice that the frequency-domain phase is denoted with the same symbol 'ψ' as the polarization angle; we shall always write the explicit frequency dependency of $\psi(f)$ when referring to the frequency-domain phase.]

The assumed Gaussian and zero-mean properties of the noise, lead one to write that the probability that an individual, n_i, is a sampling of the random process $n(t)$ is given by [4]

$$p(n_i) = [2\pi C_n(0)]^{-1/2} \exp\left[-\frac{1}{2}\frac{(n_i - 0)^2}{C_n(0)}\right] ,$$

where $C_n(\tau)$ is the correlation function of noise. Following the same arguments, the probability that the ordered set $n \equiv \{n_i : i = 1, \ldots, N\}$ is a sampling of $n(t)$ will be

$$p(n) = [(2\pi)^N \det ||C_{n,jk}||]^{-1/2} \exp\left[-\frac{1}{2}\sum_{j,k=1}^{N} C_{n,jk}^{-1} n_j n_k\right]$$

where $C_{n,jk} \equiv C_n[(j-k)\Delta t]$ and $\delta_{jk} \equiv \sum_i C_{n,ji} C_{n,ik}^{-1}$; δ_{jk} being the Kronecker's delta. Taking into account that the previously defined (one-sided) noise PSD, $S_n(f)$, is (twice) the Fourier transform of the correlation function, $C_n(\tau)$; Finn [4] shows that the previous expression for the probability of having the realization of a particular noise series, $n(t)$, in the continuum limit of $\Delta t \to 0$ and $T \to \infty$, can be written as

$$p(n) \propto e^{-\frac{1}{2}(n|n)} , \tag{3.5}$$

where the inner product ('Wiener scalar product') between two (real) time series, namely $a(t)$ and $b(t)$, has been defined as

$$(a|b) \equiv \int_{-\infty}^{\infty} \mathrm{d}f\, \frac{\tilde{a}^*(f)\tilde{b}(f) + \tilde{a}(f)\tilde{b}^*(f)}{S_n(f)} = 2\,\mathrm{Re}\int_{-\infty}^{\infty} \mathrm{d}f\, \frac{\tilde{a}^*(f)\tilde{b}(f)}{S_n(f)} = 4\,\mathrm{Re}\int_{0}^{\infty} \mathrm{d}f\, \frac{\tilde{a}^*(f)\tilde{b}(f)}{S_n(f)} .\tag{3.6}$$

In defining this inner product, we use the fact that the Fourier transform of the *real* time-domain gravitational wave strain $h(t)$ satisfies $\tilde{h}(f) = \tilde{h}^*(-f)$ [also, the one-sided noise PSD satisfies $S_n(-f) = S_n(f)$], thus allowing us to define the inner product as an integral over positive frequencies only. This Wiener scalar product is real and symmetric, and the associated norm, say

$$|a|^2 \equiv (a|a) = 4\,\mathrm{Re}\int_{0}^{\infty} \mathrm{d}f\, \frac{\tilde{a}^*(f)\tilde{a}(f)}{S_n(f)} = 4\int_{0}^{\infty} \mathrm{d}f\, \frac{|\tilde{a}(f)|^2}{S_n(f)} .\tag{3.7}$$

is positive definite, and endows the space of (real) signals with an Euclidean structure. Also notice that the inner product is normalized such that, $\overline{|n|^2} \equiv 1$; and, from the definition of $S_n(f)$ in Eq. (3.2), we get the useful property $\overline{(a|n)(n|b)} = (a|b)$.

In matched-filtering theory [5], the signal-to-noise ratio (SNR), $\rho(\boldsymbol{\lambda})$, is defined as the ratio between the filtered signal and the root-mean-squared (r.m.s.) of the filtered noise. Assuming '$h_m \equiv h_m(\boldsymbol{\lambda})$' to be our best model template and using the definition of the Wiener scalar product,

$$\rho(\boldsymbol{\lambda}) = \frac{(h_m|s)}{\text{r.m.s.}[(h_m|n)]} = \frac{(h_m|s)}{\sqrt{(h_m|n)(n|h_m)}} = \frac{(h_m|s)}{\sqrt{(h_m|h_m)}} \equiv (\hat{h}_m|s) , \tag{3.8}$$

Here, we are using a hat to denote normalized templates $\hat{h} = \frac{h}{(h|h)^{1/2}}$, so that $(\hat{h}|\hat{h}) \equiv 1$. Below, we shall see that, from a frequentist point of view, the optimal test statistics is given by the likelihood ratio (see Eq. (3.14) below); although Echeverria [6] showed that maximizing the likelihood ratio is equivalent to maximizing the SNR function defined above, and therefore $\rho(\boldsymbol{\lambda}) = (\hat{h}_m|s)$ is an optimal search statistic.

We shall use the ensemble average of $\rho(\boldsymbol{\lambda})$ to perform data analysis studies such as parameter estimation, analyze template accuracies, or the computation of expected SNRs,

$$\rho_m \equiv \overline{\rho(\boldsymbol{\lambda})} = \overline{(\hat{h}_m|s)} = \overline{(\hat{h}_m|h_x)} + \overline{(\hat{h}_m|n)}^{\,0} = (\hat{h}_m|h_x) \ . \tag{3.9}$$

The optimal SNR will be obtained when the template used h_m is the exact signal h_x that we want to detect, *i.e.*

$$\rho_{\text{opt}} = (\hat{h}_x|h_x) = \frac{(h_x|h_x)}{(h_x|h_x)^{1/2}} = (h_x|h_x)^{1/2} \ . \tag{3.10}$$

3.2 Detection and parameter estimation

There are two different ways of proceeding from this point, depending on the paradigm of statistics used: *frequentist* or *Bayesian.* These approaches yield sometimes similar-looking answers for detection and parameter estimation (especially in Gaussian noise), but they are based on fundamentally different interpretations and provide different tools in practice. The conceptual difference between the two frameworks lies in the meaning of "probability", while the axioms for *calculating* with those probabilities are the same in both cases.

This section has been written following the guidance of several reference articles in the field; in particular, the paragraphs discussing the parameter measurement accuracy are based on Refs. [4, 7–9], whereas we use Refs. [10–13] for the discussion between frequentist and Bayesian frameworks.

3.2.1 Frequentist framework

The frequentist approach is based in viewing probabilities essentially as the relative frequencies of outcomes in repeated experiments: the probability $p(A)$ of an event A is defined as the limiting fraction of events in a infinite number of "identical"[1] trials.

Given the detector data s, consisting in the sum of the true signal $h_x = h(\boldsymbol{\lambda}_x)$ [where the $\boldsymbol{\lambda}_x$ is the vector of the *true system parameters*] plus additive noise n; we select a *point estimator* $\hat{\boldsymbol{\lambda}}(s)$: that is, a vector function of detector data that (hopefully) approximates the true values of the source parameters, except for the statistical errors due to the presence of noise. We shall see below that an important point estimator is the maximum likelihood (ML) estimator $\hat{\boldsymbol{\lambda}}^{\text{ML}}$, which maximizes the *likelihood ratio* $p(s|h_x)/p(s|0)$. The estimator $\hat{\boldsymbol{\lambda}}$ is usually chosen according to one or more criteria of optimality: for instance, *unbiasedness* requires that $\overline{\hat{\boldsymbol{\lambda}}(s)}$ (the ensemble average of the estimator) to be equal to $\boldsymbol{\lambda}_x$.

---

[1]Obviously, the trials cannot truly be identical or they would always yield the same result.

Also, the statistical errors within the frequentist framework are characterized as the fluctuations of $\hat{\boldsymbol{\lambda}}(s)$ computed over a very long series of independent *experiments* where the source parameters are kept fixed, while the detector noise n is sampled from its assumed probability distribution. Mathematically, this can be represented for a generic parameter, λ_i, as

$$\mathrm{var}\hat{\lambda}_i = \overline{\left(\hat{\lambda}_i(s) - \overline{\hat{\lambda}_i(s)}\right)^2} . \qquad \text{(frequentist)} \tag{3.11}$$

The *frequentist detection problem* is formulated as one of hypothesis testing between H_0 (no signal) or H_1 (there is a signal). Then, a *detection statistic* $\Lambda(s)$ is built and H_0 is accepted if $\Lambda(s) < \Lambda^*$; whereas if $\Lambda(s) \geq \Lambda^*$ we accept H_1. Of course, there may be cases where

- $\Lambda(s) \geq \Lambda^*$, but there is no signal: *false alarm probability*, namely

$$\alpha(\Lambda^*) \equiv \int_{\Lambda^*}^{\infty} p(\Lambda(s)|H_0)\,\mathrm{d}\Lambda , \tag{3.12}$$

  which is the probability of a threshold crossing despite H_0 being true; and

- $\Lambda(s) < \Lambda^*$, but there was actually a signal: *false dismissal probability*,

$$\beta(\Lambda^*|h_x) \equiv \int_{-\infty}^{\Lambda^*} p(\Lambda(s)|H_1)\,\mathrm{d}\Lambda , \tag{3.13}$$

  which is the probability that the threshold is not crossed, even though H_1 is true. The *detection probability* η is simply the complement, namely $\eta(\Lambda^*|h_x) = 1 - \beta$.

The test $\Lambda(s)$ should maximize the detection probability, η, at a given false alarm rate, α. According to the Neyman-Pearson lemma, this optimal test is the so-called *likelihood ratio*, which is defined as

$$\Lambda(s; h_x) = \frac{p(s|H_1)}{p(s|H_0)} = \frac{p(s|h_x)}{p(s|0)} \tag{3.14}$$

Since $p(n) \propto \exp[-\frac{1}{2}(n|n)]$ and $n = s - h_x$, we have that

$$p(s|h_x) \propto e^{-\frac{1}{2}(s-h_x|s-h_x)} \qquad \text{and} \qquad p(s|0) \propto e^{-\frac{1}{2}(s|s)}$$

and therefore, the optimal test within the frequentist framework can be written in terms of the inner product as

$$\log \Lambda(s; h_x) = (s|h_x) - \tfrac{1}{2}(h_x|h_x) , \tag{3.15}$$

which is the well-known expression for the matched-filtering amplitude. Given a measured data set s and the exact waveform model $h_x(\boldsymbol{\lambda})$ with unknown parameters, one has to find the *maximum* of the log-likelihood function, $\log \Lambda$, as function of the unknown parameters. With this, one has defined the maximum likelihood (ML) estimator, $\hat{\boldsymbol{\lambda}}^{\mathrm{ML}}$.

The exploration of the parameter space searching for the maximum of the likelihood ratio is at the very heart of every GW search within the frequentist framework. When the

dimensionality of the parameter space is low and the computation of the likelihood ratio (3.15) is not very expensive in computational terms, one normally uses a uniform grid to place the templates to be explored. When the problem is computationally more demanding (usually because of the high number of dimensions in the parameter space), different techniques have been explored in order to place the finite number of templates in the most 'interesting'[2] parts of the parameter space, such as defining curved metric spaces [14–17], 'stochastic template banks' [18–20], or using random template bank strategies [21].

As it has been previously mentioned, Echeverria [6] showed that maximizing the likelihood ratio (3.15) is *equivalent* to maximizing the SNR function (3.8), so both functionals can be used as optimal search statistics.

It is needless to say that the threshold Λ^* to determine whether a signal has been detected or not, will be set, for each particular problem, by fixing the maximum allowed values given a false alarm and false dismissal probabilities, see Eqs. (3.12) and (3.13).

3.2.2   Bayesian framework

Bayesian statistics is built on a different concept of probability, quantifying the degree of certainty ('degree of belief') of a statement being true. So, one can assign probabilities $p(A|\mathcal{M}) \in [0, 1]$ to any statement A given a certain model $\mathcal{M}$, quantifying one's (possibly incomplete) knowledge about the truth of A. In particular, for GW data analysis problems in the Bayesian approach, we simply compute the posterior probability distribution function $p(h|s, \mathcal{M})$ for the waveforms h of the model hypothesis $\mathcal{M}$, and the associated model evidence $p(s|\mathcal{M})$. These are related by Bayes' theorem to the likelihood $p(s|h, \mathcal{M})$ of our observed strain s with our model waveform and the prior information $p(h|\mathcal{M})$ as

$$p(h|s, \mathcal{M}) = \frac{p(h|\mathcal{M})\, p(s|h, \mathcal{M})}{p(s|\mathcal{M})} \, , \tag{3.16}$$

the model evidence being

$$p(s|\mathcal{M}) = \int p(h|\mathcal{M})\, p(s|h, \mathcal{M}) \mathrm{d}h \, . \tag{3.17}$$

Here, the likelihood function $p(s|h, \mathcal{M})$ is the same as in the previous section, which [making use of the Gaussianity of the noise] is $p(s|h, \mathcal{M}_x) \equiv p(s|h_x) \propto \exp[-\frac{1}{2}(s - h_x|s - h_x)]$ if one assumes that has access to the exact model. In reality, we only know an approximation to the exact templates, and therefore the likelihood will be simply computed as $p(s|h, \mathcal{M}) \propto \exp[-\frac{1}{2}(s - h_m|s - h_m)]$.

Everything we want to know about the waveform model h_m is contained in the posterior distribution, while the evidence allows for comparisons to be made between alternative models (*e.g.* whether a GW signal is present or not; models with different number or kind of sources...). It is important to emphasize that in the Bayesian approach, the output is only as good as the inputs, in the sense that we are converting a *prior* knowledge about any statement into a *posterior* one throughout the likelihood of the measure s and our template waveforms h; but if the waveform model or the likelihood function is flawed, then the conclusion will also be flawed. The hope or expectation, both at the parameter

---

[2]With higher likelihood ratio values.

level and model level, is that data will be obtained of sufficient quality to overturn incorrect prior hypotheses.

The Bayesian evidence (3.17) sets up a tension between the ability of a model to fit the data and the prior *predictiveness*[3] of the model, in a quantitative implementation of Occam's razor [22]. The models that do best are the ones that make specific predictions that later turn out to fit the data well. Less predictive models, even if they can fit the data as well, score more poorly.

Any waveform model is characterized by a set of parameters $(h|\mathcal{M}) \equiv h_m \equiv h_m(\boldsymbol{\lambda})$, thus in Bayesian inference all the probability density functions (PDFs) shall be written as PDFs of the model parameters, which are taken as random variables: the priors $p(h|\mathcal{M}) \equiv p(\boldsymbol{\lambda})$; the likelihood function $p(s|h, \mathcal{M}) \equiv p(s|h_m(\boldsymbol{\lambda}))$; and the posterior $p(h|s, \mathcal{M}) \equiv p(\boldsymbol{\lambda}|s)$. Also, the integrals over h are, indeed, multidimensional integrals over all the parameters set, for instance the evidence (3.17) is computed as

$$p(s|\mathcal{M}) = \int p(\boldsymbol{\lambda}) \, p(s|h_m(\boldsymbol{\lambda})) \mathrm{d}\boldsymbol{\lambda} \; . \tag{3.18}$$

The output of the Bayes' theorem is the *joint* PDF of all the parameters that characterize our model $\boldsymbol{\lambda} = \{\lambda_1, \ldots, \lambda_N\}$, but one can easily obtain the posterior PDF of a given subset of parameters, say $\lambda_1, \ldots, \lambda_n$ with $n < N$, by *marginalizing* the original joint posterior probability

$$p(\lambda_1, \ldots, \lambda_n|s) = \int \mathrm{d}\lambda_{n+1} \ldots \int \mathrm{d}\lambda_N \frac{p(\boldsymbol{\lambda}) \, p(s|h_m(\boldsymbol{\lambda}))}{p(s|\mathcal{M})} \; . \tag{3.19}$$

With this, we can obtain the posterior PDF of any parameter or set of parameters and consequently, compute the posterior mean of a given parameter λ_i [we recall that in Bayesian inference, model parameters are taken as random variables],

$$\langle \lambda_i \rangle_p \equiv \int \lambda_i p(\lambda_i|s) \mathrm{d}\lambda_i \bigg/ \int p(\boldsymbol{\lambda}|s) \mathrm{d}\boldsymbol{\lambda} \tag{3.20}$$

and the quadratic moment

$$\langle \lambda_i \lambda_j \rangle_p \equiv \int \lambda_i \lambda_j \, p(\lambda_i, \lambda_j|s) \, \mathrm{d}\lambda_i \mathrm{d}\lambda_j \bigg/ \int p(\boldsymbol{\lambda}|s) \mathrm{d}\boldsymbol{\lambda} \tag{3.21}$$

where "$\langle \cdot \rangle_p$" denotes integration over the posterior PDF, $p(\boldsymbol{\lambda}|s)$. The variance $\mathrm{var}\lambda_i = \sigma_i^2$ in the estimation of the parameter λ_i [σ_i being the root-mean-square of λ_i] can then be calculated as

$$\mathrm{var}\lambda_i = \sigma_i^2 = \langle (\Delta\lambda_i)^2 \rangle_p = \langle (\lambda_i - \langle\lambda_i\rangle_p)^2 \rangle_p = \langle \lambda_i^2 \rangle_p - \langle\lambda_i\rangle_p^2 \; , \qquad \text{(Bayesian)} \tag{3.22}$$

and the correlation coefficients c_{ij} between two parameters λ_i and λ_j are given by

$$c_{ij} = \frac{\langle \Delta\lambda_i \Delta\lambda_j \rangle_p}{\sigma_i \sigma_j} = \frac{\langle \lambda_i \lambda_j \rangle_p - \langle\lambda_i\rangle_p \langle\lambda_j\rangle_p}{\sigma_i \sigma_j} \; . \qquad \text{(Bayesian)} \tag{3.23}$$

---

[3]Which is not necessarily directly related to, for instance, the number of parameters.

Of course, equivalent expressions could be written for any higher moment. In case we are always considering the same model $\mathcal{M}$, the associated model evidence will play the simple role of a normalization constant in Eq. (3.16), and the same thing happens with the integrals in the denominator of the previous equations: (3.20) and (3.21). Thus, we can see how Bayesian *parameter estimation* can be naturally performed directly from the posterior PDFs, either by directly quoting them, or by computing parameter ranges within a certain confidence level, or just by computing variances.

The Bayesian *detection problem* turns out to be a simple model selection problem: we compare the odds of the data being more consistent with our model of the gravitational signal and instrument noise, or our model of the instrument noise alone. This forces us to explicitly define an instrumental noise model and, if our particular model is poor – for instance, not allowing for occasional glitches if they may happen – then the odds may favor the detection hypothesis even when no signal is present in the data [12]. Again, Bayes' theorem can be applied to update a prior model probability by the *evidence* (3.18) and obtain the probability of the model $\mathcal{M}$ given the data s. In particular, since computing actual probability values for a certain model over all its competing models would require a prior knowledge of *all possible models* testable by our experiment, which is impractical; what we compute is the odds ratio for one model over another:

$$\mathcal{O}_{10} \equiv \frac{p(\mathcal{M}_1|s)}{p(\mathcal{M}_0|s)} = \frac{p(\mathcal{M}_1)}{p(\mathcal{M}_0)} \frac{p(s|\mathcal{M}_1)}{p(s|\mathcal{M}_0)} \equiv \mathcal{P}_{10}\,\mathcal{B}_{10}\;. \tag{3.24}$$

$\mathcal{O}_{10}$ is the odds ratio for models $\mathcal{M}_1$ and $\mathcal{M}_0$; an odds ratio $\gtrsim 3$ favors $\mathcal{M}_1$ [23]. The odds ratio has been written as the product of the prior odds $\mathcal{P}_{10}$ and the Bayes factor $\mathcal{B}_{10}$ (also known as the evidence ratio or marginal likelihood ratio). The former reflect any preference between the models before the experiment is conducted, thus if we are to adopt one model over the other, the Bayes factor must overwhelm the prior odds, signaling the data are sufficiently informative to distinguish between competing hypotheses.

Littenberg and Cornish [12] point out an important note of caution here, which is that a Bayesian analysis is *not* answering the question "Is there a gravitational wave signal present in the data, or is it just instrument noise?", but rather, "Are the data most consistent with our model of the gravitational wave signal and instrument noise, or our model of the instrument noise alone?".

Markov chain Monte Carlo

In typical GW data analysis applications the number of parameters needed to describe the signal and noise models can be very large (ranging from tens to hundreds of thousands), and the regions of significant posterior weight generally occupy a minute fraction of the total prior volume. Resolving the peaks in the posterior distribution function requires a very fine sampling of the parameter space, but if this sampling is extended over the entire prior volume, the total number of samples can become astronomically large, *discarding* any possibility to sample posterior PDFs using *grid-based methods*.

The Markov chain Monte Carlo (MCMC) approach encompasses a powerful set of techniques for producing *gridless* samples from the posterior distribution, focussing their attention on regions of high posterior weight, and neatly avoiding the problem of computing

model evidence. The latter feature becomes less desirable when one is interested in model selection and therefore, in computing Bayes factors. One solution is to generalize the transitions between steps in the Markov chain (see below for a definition) to include "transdimensional" moves between different models, resulting in what are termed reversible jump Markov chain Monte Carlo (RJMCMC) algorithms. All the results presented in this thesis (see, in particular, Chapter 6) consider a single model, though the next step for future work is to implement RJMCMC in the search for an unknown number of galactic binary signals with LISA.

In general, MCMC methods are based on constructing a Markov chain that has the desired distribution (*target distribution*, π) as its *equilibrium distribution*. The state of the chain (or value of the parameters $\boldsymbol{\lambda}$ describing the problem at hand) after a large number of steps is then used as a sample from the desired distribution and, in particular, it can be used to compute marginalization integrals such as the ones represented above [see *e.g.* Eqs. (3.17)-(3.21)] via Monte Carlo integration [24], when one fixes the target distribution to be the joint posterior PDF of all parameters, $\pi(\boldsymbol{\lambda}) \equiv p(\boldsymbol{\lambda}|s)$.

Metropolis-Hastings (MH) algorithms are employed in the overwhelming majority of the practical implementations of MCMC methods in order to construct a Markov chain with the desired properties. In MH updates, given a state of the Markov chain $\boldsymbol{\lambda}$, one proposes a new state $\boldsymbol{\lambda}'$ drawn from a *proposal distribution* (or transition kernel) $q(\boldsymbol{\lambda}, \boldsymbol{\lambda}')$. This new state is accepted with probability

$$\alpha(\boldsymbol{\lambda}, \boldsymbol{\lambda}') = 1 \wedge \left\{ \frac{\pi(\boldsymbol{\lambda}') \, q(\boldsymbol{\lambda}', \boldsymbol{\lambda})}{\pi(\boldsymbol{\lambda}) \, q(\boldsymbol{\lambda}, \boldsymbol{\lambda}')} \right\} \, , \tag{3.25}$$

and the chain remains at $\boldsymbol{\lambda}$ with probability $1 - \alpha(\boldsymbol{\lambda}, \boldsymbol{\lambda}')$. In the previous equation, the notation $a \wedge b$ (for any real numbers a and b) stands for the minimum between a and b, and as a consequence the acceptance probability is limited to unity in the case where the ratio is > 1. The iteration of this process constitutes the core for constructing a Markov chain whose equilibrium distribution, after an initial 'burn-in' period that is discarded in the generation of the resulting PDFs, coincides with the target distribution, π; in our case being the joint posterior PDFs of all the parameters. A (renormalized) *histogram* of some of the parameter values characterizing the elements of the resulting chain represents their posterior PDF, and an *average along the sample path of the Markov chain* of a function f of the parameters, will be an asymptotically unbiased estimator of $\int f(\boldsymbol{\lambda})\pi(\boldsymbol{\lambda})\mathrm{d}\boldsymbol{\lambda}$. Let us notice that MCMC algorithms prevent us to compute the model *evidence* since, for a fixed model, it only plays of a normalization constant. As we said, in case one were interested in computing evidence ratios, then they should consider "transdimensional" moves and RJMCMC.

The convergence to the target distribution π is guaranteed through the acceptance probability (3.25), but the convergence rate or efficiency of the chain is highly dependent on the choice of the transition kernel q; indeed, its choice is one of the most critical stages in actually implementing a MH-MCMC algorithm. If the proposed jumps are too short, the simulation moves very slowly through the target distribution; whereas if we jumps are too big, most of the new proposed states lie into low-probability areas of the target distribution, causing the Markov chain to stand still most of the time. In a very interesting work, Gelman *et al.* [25] study what are the most efficient [having defined 'efficiency' as the relative variance of an estimator from the MH-MCMC output compared to independent sampling] symmetric jumping kernels for simulating a normal target distribution using

the Metropolis algorithm. For a d-dimensional spherical multivariate normal problem, the optimal symmetric jumping kernel has its scale $\approx 2.4/\sqrt{d}$ times the scale of the target distribution and the acceptance rate of the associated Metropolis algorithm is approximately 44% for $d = 1$ and declines to 23% as $d \to \infty$ [the efficiency of the Metropolis algorithm, compared to independent samples from the target distribution, is approximately $0.3/d$].

In Chapter 6, we shall implement an algorithm based on MCMC in order to search for, first single and then multiple, galactic binary signals buried in LISA noise. On the way, we shall face the problem of a dramatic reduction in the convergence rate of the standard MH-MCMC implementation, due to the presence of multiple secondary maxima in the target distribution along several dimensions of the parameter space. This is an extended issue present in many MCMC applications. The solution proposed in Chapter 7 is a completely Markovian and fully general algorithm based on a technique called Delayed Rejection.

3.2.3 Fisher information matrix formalism

Over the last two decades, in the absence of confirmed GW detections, the prevailing attitude in the GW source-modeling community has been on exploring which astrophysical systems, and which of their properties, would become accessible to GW observations with the sensitivities afforded by planned future experiments, with the purpose of committing theoretical effort to the most promising sources, and of directing public advocacy to the most promising detectors. In this context, the *expected accuracy* of GW source parameters is often employed as a proxy for the amount of physical information that could be obtained from GW observations. Currently, these kind of studies are being performed for the third generation ground-based detectors (*e.g.* the european Einstein Telescope), as well as the future interferometer space-based antenna, LISA.

Predicting the parameter-estimation performance of future observations is a complex matter, mainly because there are a few analytical tools that can be applied generally to the problem. In the source-modeling community, the analytical tool of choice has been the Fisher information matrix (FIM), defined in terms of the Wiener scalar product as follows,

$$F_{ij}[h] \equiv \left(\frac{\partial h}{\partial \lambda_i} \bigg| \frac{\partial h}{\partial \lambda_j} \right) \ . \tag{3.26}$$

The FIM formalism has been extensively used in GW data analysis providing very useful information about the expected physics that shall be obtained from GW observations; however, as Vallisneri points out in Ref. [10], one must be aware to not "abuse" of the FIM which could lead to misinterpretations. Vallisneri provides three different interpretations (all correct) of the meaning of the FIM and, in particular, of its inverse matrix $F_{ij}^{-1}[h_x]$, that we quote here:

1. The inverse Fisher matrix $F_{ij}^{-1}[h_x]$ is a lower bound (generally known as the *Cramér-Rao bound*) for the error covariance of any *unbiased estimator* of the true source parameters; thus it is a *frequentist error*.

2. The inverse Fisher matrix $F_{ij}^{-1}[h_x]$ is the frequentist error covariance for the *maximum likelihood (ML)* parameter estimator $\hat{\lambda}^{\mathrm{ML}}$, assuming Gaussian noise, in the limit of strong signals (*i.e.* high SNR) or, equivalently, in the limit in which the

waveforms can be considered as linear functions of source parameters [sometimes called *linearized-signal approximation (LSA)*].

3. The inverse Fisher matrix $F_{ij}^{-1}[h_x]$ represents the covariance (*i.e.* the multidimensional spread around the mode) of the *posterior probability distribution* $p(\boldsymbol{\lambda}_x|s)$ for the true source parameters $\boldsymbol{\lambda}_x$, as inferred (within the Bayesian framework) from a *single* experiment with true signal h_x, assuming Gaussian noise, in the high SNR limit (or in the LSA), and in the case where any *prior probabilities* for the parameters are constant over the parameter range of interest. Properly speaking, in this case the inverse Fisher matrix would be a measure of uncertainty rather than error, since in any experiment the mode will be displaced from the true parameters by an unknown amount due to noise.

As pointed out by Jaynes [26], while the numerical identity of these three different error-like quantities has given rise to much confusion, it arises almost trivially from the fact that in a neighborhood of its maximum, the signal likelihood $p(s|\boldsymbol{\lambda}_x)$ is approximated by a normal PDF with covariance $\Sigma_{ij} = F_{ij}^{-1}$. Let us recall that, given the covariance matrix Σ_{ij}, the root-mean-square error σ_k in the estimation of the parameter λ_k can then be calculated by taking the square root of the diagonal elements of the covariance matrix,

$$\sigma_k = \langle (\Delta\lambda_k)^2 \rangle^{1/2} = \sqrt{\Sigma_{kk}} \, , \tag{3.27}$$

and the correlation coefficients c_{jk} between two parameters λ_j and λ_k are given by

$$c_{jk} = \frac{\langle \Delta\lambda_j \Delta\lambda_k \rangle}{\sigma_j \sigma_k} = \frac{\Sigma_{jk}}{\sqrt{\Sigma_{jj}\Sigma_{kk}}} \, . \tag{3.28}$$

Here, the angle brackets denote an average either over noise realizations $\langle \cdot \rangle_n$ if one considers the frequentist interpretation, or over the posterior PDF $\langle \cdot \rangle_p$ in the Bayesian framework.

In some cases, the Fisher matrix can be *singular*, so that the attempts to invert it numerically yield warnings that it is badly conditioned. In this case, the solution relies in removing the eigenvectors with null eigenvalues from the Fisher information matrix, as they represent combinations of parameters that leave the waveform unaltered. What is more common in practice, is to have high correlations between parameters (without being exact degeneracies) that give rise to *ill-conditioned* Fisher matrices, which inverse can be computed, but may be difficult to. In particular, one can find an extreme sensitivity of the inverse Fisher matrix results to the small numerical errors in the input; which is why one must be very cautious when computing the elements of the Fisher matrix: always trying to do as much of analytical calculations as possible, simplifying the expressions if possible and adopting higher-precision arithmetics. In particular, Fisher matrices computed from CBCs waveforms are frequently ill-conditioned[4] and therefore one must be extremely careful in the calculations (see Chapter 4). One way to check whether one is obtaining reliable results is to add small random perturbations, Monte Carlo-style, to the Fisher-matrix elements and then verify the change in the covariance matrix.

In particular, in this thesis (Chapter 4) we have used the FIM formalism to study the *impact in the parameter estimation of adding the higher harmonics to the inspiral CBC*

---

[4]Waveforms are characterized by a number of parameters which, in some places of the parameter space, can become degenerated.

waveform observed with LISA. We also use these results to estimate the *precision in measuring the dark energy equation of state* with single LISA observations of SMBHs coalescence events (Chapter 5), *i.e.* we explore the repercussions of LISA observations in cosmology. In all these studies, several actions have been carried out in order to prevent the possible effects from having ill-conditioned Fisher matrices and ensure the reliability of the FIM output results; in particular,

- the analytical expressions of the waveforms have been factorized in order to identify common factors and facilitate the derivation;

- all the waveform derivatives have been computed analytically; simplifying and factorizing the final expressions in order to eliminate possible numerical divergences;

- all the variables in the numerical code are "double precision" and the inversion process is done using the Cholesky decomposition implemented in `gsl`;

- the covariance matrix results have been generated over a grid in the parameter space and the output results present a smooth variation rather than strong oscillations;

- our results have been validated by the LISA Performance Evaluation (Taskforce) (LISA PE) [27].

Finally, let us recall that the FIM represents a fast and analytical tool to estimate the covariance matrix under certain assumptions (high SNR or LSA) and it can be very useful to obtain first approximations or to compare results when using different waveform models. However, results of posterior PDFs obtained within the Bayesian framework, despite being much more expensive to obtain in terms of CPU time, will always be more faithful and realistic than FIM. For extensive parameter estimation studies, normally what it is done is to use the FIM formalism to explore all the parameter space and just compute Bayesian posterior PDFs for a very limited number of cases in order to check the validity of FIM results.

Another important application of the FIM formalism is precisely to build the proposal jumps in MH-MCMC algorithms that sample posterior PDFs. As it is said in Sec. 3.2.2, for a d-dimensional spherical multivariate normal problem, the optimal symmetric jumping kernel has its scale $\approx 2.4/\sqrt{d}$ times the scale of the target distribution. The inverse Fisher matrix can indeed provide an estimation of this scale beforehand.

3.3   Modeling gravitational waveforms from Compact Binary Coalescences

During the last 5-10 years our knowledge of the dynamics of coalescing binary black hole (BBH) systems and their gravitational emission has experienced a huge progress, both with the improvement of analytical methods, namely PN expansions and EOB approaches, and the breakthroughs that occurred in Numerical Relativity (NR). The purpose of this section is to describe the main features and properties of such methods and to give references for further information. Since all the topics worked out in this thesis are focussed on data analysis (we have not contributed to the development of CBC waveforms), we shall present

here the different waveform models basically from an "end-user" perspective, without entering too much into details.

According to their validity range, work domain and method used to solve the dynamics; we can classify the different currently available model waveforms into several categories:

- time-domain PN models (either using closed-form expressions or integrating ordinary differential equations (ODEs)), which consist in expanding Einstein's equations in Taylor series of some PN expansion parameter (usually a characteristic velocity, v) and solving them term by term. They provide a faithful description of the dynamics in the inspiral part of the evolution, where the motion is still adiabatic. However, they fail describing the late-inspiral, merger and ring-down parts, where the velocities become highly relativistic;

- closed-form, frequency-domain models which are only accurate in a limited range of the evolution. Into this category would fit either the analytically Fourier transformed PN models (using the Stationary Phase Approximation, see Sec. 3.3.1) and the (NR-fitted) phenomenological models, which try to extend their validity range by combining information coming from closed-form PN (for the inspiral part) and ringdown models, and some NR simulations (for the merger part and in order to link late-inspiral and ring-down);

- EOB models, which incorporate information from both PN theory and NR simulations into an accurate description of the full dynamics of a CBC, from the early inspiral up to the end of the merger. They are defined in the time-domain by integrating ODEs;

- full NR simulations, which are necessary for describing the nonperturbative physics around the merger, but can only cover a limited number of orbits ($\lesssim 15$) because they are very time consuming in terms of computational costs;

- various types of *hybrid* models, joining together (either in the time-domain, or in the frequency-domain) early PN-type waveforms to later NR waveforms, so as to cover the whole evolution.

The time needed to generate a waveform in one of these categories varies by many orders of magnitude between, say, a closed-form frequency-domain waveform (a fraction of a second on a single CPU); an EOB waveform (several seconds, also, on a single CPU); or, a full NR simulation ($\sim$ a month on a computer cluster with several hundreds of CPUs). Also, of course, the accuracy of the waveforms produced by each of these models varies inversely; having the NR waveforms to be the most accurate (one could indeed think that the *exact* waveform would be contained within the numerical errors), then the EOB ones, and finally the less accurate are the closed-form waveforms (either PN or phenomenological). From the data-analysis point of view, it would be quite useful to be able to generate waveforms as fast as possible, though the real issue is to be able to *access* a dense bank of them very fast. Thus, though some trade off between fastness and accuracy can be allowed for, there are minimal accuracy requirements that waveforms have to satisfy. In Chapter 8 we perform a detailed analysis of the accuracy of the fastest existing waveforms, namely the closed-form, frequency-domain ones.

Let us now summarize the recent progress made on the different approaches and point out some references for further information. Finally, in Sec. 3.3.1, we shall describe an analytical (and approximated) procedure to obtain Fourier transformed expressions of time-domain chirping signals [such as the inspiral part of CBC waveforms], called Stationary Phase Approximation (SPA).

Post-Newtonian models

The post-Newtonian approximation computes the evolution of the GW phase $\phi_{\text{GW}}(t)$ (twice the *orbital* phase ϕ_{orb}, see Chapter 2) of a compact binary as a perturbative expansion in a small parameter, typically taken as the characteristic velocity in the binary, $\text{v} = (\pi MF)^{1/3}$, or $x \equiv \text{v}^2$, although other variants exist. We recall that $M = m_1 + m_2$ is the total mass of the binary and $F = \dot{\phi}_{\text{GW}}/(2\pi)$ is the GW frequency. PN evolution is based on the so-called adiabatic approximation, according to which the fractional change in the orbital frequency over each orbital period is negligibly small, *i.e.* $\dot{F}_{\text{orb}}/F_{\text{orb}}^2 = \dot{F}_{\text{GW}}/(2F_{\text{GW}}^2) \ll 1$. This assumption is valid during most of the evolution, but starts to fail as the system approaches the *last stable orbit (LSO)*, where $\text{v}_{\text{LSO}} = 1/\sqrt{6}$.

Given PN expansions of the motion of, and gravitational radiation from, a binary system, one needs to compute the "*phasing formula*" for $\phi_{\text{GW}}(t; \boldsymbol{\lambda}_{\text{src}})$. In the adiabatic approximation, the phasing formula is easily derived from the energy and flux functions by a pair of differential equations,

$$\dot{\phi}_{\text{GW}}(t) = 2\text{v}^3/M \qquad \text{and} \qquad \dot{\text{v}} = -\mathcal{F}(\text{v})/E'(\text{v}) \;,$$

where $\mathcal{F}(\text{v})$ is the GW luminosity and $E'(\text{v})$ is the derivative of the binding energy with respect to v. *Different PN families* arise because one can choose to treat the ratio $\mathcal{F}(\text{v})/E'(\text{v})$ differently starting formally from the same PN order inputs [3]. For instance, one can retain the PN expansions of the luminosity $\mathcal{F}(\text{v})$ and $E'(\text{v})$ as they appear (the so-called TaylorT1 model), or expand the rational polynomial $\mathcal{F}(\text{v})/E'(\text{v})$ in v to consistent PN order (the TaylorT4 model [28]), recast as a pair of parametric equations $\phi_{\text{GW}}(t)$ and $t(\text{v})$ (the TaylorT2 model), or the phasing could be written as an explicit function of time $\phi(t)$ (the TaylorT3 model). These different representations are made possible because one is dealing with a perturbative series. Therefore, one is at liberty to "resum" or "re-expand" the series in any way one wishes (as long as one keeps terms to the correct order in the perturbation expansions), or even retain the expression as the quotient of two polynomials and treat them numerically. There is also the freedom of writing the series in a different variable, say (suitably dimensional) E (the so-called TaylorEt model [29–31]).

The description of CBCs through PN expansions theory has been developed for many years and currently, the evolution of the orbital phase is known up to 3.5PN order (*i.e.* up to $\mathcal{O}(\text{v}^7)$ in the PN expansion) for non-spinning systems in circular orbits [3, 32–39]; see, in particular, Ref. [3] for a complete summary of useful expressions. Moreover, the amplitude of the dominant $(2, 2)$ mode can be computed up to 3PN order [40], whereas the remaining components (up to $\ell = 8$) are also known up to lower PN orders (see also Ref. [40] for explicit expressions). Also, a lot of work has been done describing the spin effects within the PN approximation [32–34, 41–48]; in particular, we know the leading and next-to-leading order *spin-orbit* effects [42–44] and the *spin-spin* effects that appear at relative 2PN order [44–46], these latter only valid when the compact objects are BHs. The amplitude corrections for spinning objects are presented in Ref. [47, 48].

By combining PN expansions with an approximated way to compute the Fourier transform (FT) of a chirping signal, namely the SPA (see below, Sec. 3.3.1), one can obtain closed-form expressions directly in the Fourier domain. Here too, there are many inequivalent ways in which the phasing $\psi(f)$ [see Eq. (3.4)] can be worked out; the most popular ones consist either in substituting for the energy and flux functions their PN expansions without doing any re-expansion or resummation (the TaylorF1 model), or in using the PN expansions of energy and flux but re-expand the ratio $\mathcal{F}(v)/E'(v)$ (the so-called TaylorF2 model) in which case the integral can be solved explicitly, leading to an explicit, Taylor-like, Fourier domain phasing formula: $\psi(f) = 2\pi f t_{\rm ref} - \phi_{\rm ref} + \frac{3}{128\eta v^5} \sum_{k=0}^{N} \alpha_k v^k$ [see Ref. [49] for the explicit expression of the α_k coefficients up to 3.5PN order]. The terms $t_{\rm ref}$ and $\phi_{\rm ref}$ are simple reference time and phase values.

Numerical Relativity simulations

Since the initial breakthroughs in 2005 [50–52], there has been dramatic progress in NR simulations for GW astronomy, including many more orbits before merger, greater accuracy and a growing sampling of the BH binary parameter space. There are now several groups around the world with codes capable of performing BBH simulations [51–62]. There are two analytic forms of the Einstein equations (BSSN [63–65] and the Generalized Harmonic [51, 66, 67]), and various numerical methods (high order finite differencing, pseudo-spectral, adaptive mesh refinement, multi-block) in use in the community. A summary of the published "long" waveforms is given in the review [68], and a complete catalog of waveforms is being compiled in [69]; more recent work is summarized in [70]. NR results are now accurate enough for GW astronomy applications over the next few years [71], and have started playing a role in GW searches [72, 73].

Accurate NR simulations will produce the most accurate and faithful results of any of the methods we summarize here. However, the computational cost to perform a single NR simulation is about a month on a computer cluster with several hundred of CPUs (this is a factor $\sim 10^8$ longer [in actual CPU time] than EOB; and much more compared to closed-form frequency domain waveforms) and the longest NR BBH waveform produced so far lasts for 15 orbits, includes the merger and ringdown phases and corresponds to an equal-mass case [74, 75]. Moreover, for a 3D NR code, one of the most challenging problems is the simulation of BHs of very different masses, and the reason is that, for a fixed total mass $M = m_1 + m_2$, the gravitational wavelength remains approximately constant with varying the mass ratio q, but the length and time scales required to resolve the smaller hole scales approximately with q. Indeed, the highest mass ratio that has been simulated is $q = 10$ [70].

Thus, there are several practical limitations that avoid NR waveforms to be extensively used for GW astronomy, namely *(i)* the extremely high computational cost, *(ii)* number of orbits $\lesssim 15$ and *(iii)* mass ratios $q \leq 10$. For this reason, different groups are working on several approaches to make use of the information from NR simulations in order to build approximated, but much faster, models (see below).

Effective-One-Body approach

The EOB formalism [76–78] has the unique feature of being able to incorporate information coming both from PN theory and NR simulations into an accurate description of the full dynamics and GW radiation of a CBC, from the early inspiral up to the end of the merger. In particular, besides incorporating the full PN information available, the EOB formalism goes beyond PN theory, even during inspiral, in several ways: *(i)* it replaces the PN-expanded results by *resummed* expressions that have shown to be more accurate in various cases; *(ii)* it includes more physical effects, notably those associated with the *non adiabatic* aspects of the inspiral. We recall that all the PN models presently considered in the literature make the approximation that the GW phase can be computed in an adiabatic manner, by simply using the balance between the GW energy flux, $\mathcal{F}(v)$, and the adiabatic loss of binding energy of the binary system, $E(v)$, (see above). In addition to improving any PN model (even in the inspiral part), the EOB formalism naturally introduces the leading order of the unknown parameters to be calibrated using a very reduced number of NR simulations. All these improvements have made the currently most accurate version of the EOB waveforms [79] to agree, within the numerical error bars, with the currently most accurate NR waveform [74, 75, 80].

Originally, the EOB formalism was introduced by Buonanno and Damour in Ref. [76] as an extension to the non-adiabatic regime of the inspiral and right after, they were able to add the ring-down phase [77] and therefore to have a representation of the full dynamics, from the early inspiral up to the end of the merger. The extension of the EOB Hamiltonian to spinning systems was first done in Ref. [46], which then was enhanced by including next-to-leading order spin-orbit coupling effects [81].

Over the last years, it has become possible to improve the EOB waveform by comparing it to the results of accurate NR simulations and by using the natural 'flexibility' of the EOB formalism to 'calibrate' some EOB parameters representing either higher-order perturbative effects that have not yet been analytically calculated, or non-perturbative effects that can only be accessed by NR simulations [79, 80, 82–85]. A similar work has recently been done using some spinning, non-precessing and equal-mass NR simulations [86]. In addition, several theoretical improvements have been brought in the EOB formalism, notably concerning new ways of resumming the GW waveform [83, 87], and the GW radiation reaction [79].

Phenomenological models

The coalescing process of a compact binary system is divided into three consecutive phases: inspiral, merger and ringdown. We have seen that *PN models* are accurate describing the adiabatic inspiral phase of the evolution which covers the major part of the coalescence: from the beginning of the inspiraling process up to several orbits before the merger. However, it is during these very last orbits (late inspiral – merger – ringdown phases) where most of the (GW) luminosity is emitted and therefore, they play a crucial role for GW detection. An accurate description of these very last, highly relativistic orbits in the coalescence process is obtained from *NR simulations*, which provide the most faithful description of the actual dynamics but they just can cover a limited number of simulated orbits.

When there exists a frequency range in the late inspiral phase, where *(i)* PN models are still accurate enough and *(ii)* it is close enough to the merger so that NR simulations already cover it; then one can build *hybrid waveforms* and obtain a waveform valid in all the stages of the evolution. [These hybrid waveforms are also build even when one is working with EOB and wants to have access to the very low frequency part of the waveform, in the deep inspiral, where the evolution is so slow and adiabatic that there is absolutely no need to use anything else than PN (see Chapter 8).]

Given the computational cost of producing NR simulations, the number of hybrid wave-forms that one has access to is finite. What Ajith *et al.* [88, 89] and Santamaria *et al.* [90] propose is to take a discrete sample of these hybrid waveforms in the frequency domain and build closed-form *phenomenological* waveform models, *i.e.* using the known functional forms that better represent the different stages (*e.g.* a PN expansion for the GW phase and inspiral part of the GW amplitude, or a Lorentzian function for the amplitude during the ring-down), but considering the phenomenological coefficients that best matched each of the original hybrid waveforms. A simple polynomial fitting of each coefficient along the different dimensions of the parameter space completes the construction of the closed-form phenomenological model. At the end, $A(f)$ and $\psi(f)$ are functions of the phenomenological parameters, which at the same time are given in terms of the physical parameters (mass ratio, spins, ...).

3.3.1   Stationary Phase Approximation

Einstein's equations are usually solved in the *time domain* and so are expressed the re-sulting waveforms. However, data analysts normally work in the *frequency domain* as the reader must have noticed from all the derivations made above in Secs. 3.1 and 3.2 [the reason relies in that most of the GW signals are quasi-monochromatic and so they can be expressed in a more compact way in the frequency domain]. Thus, the first step in any data analysis study will consist in Fourier transforming the time-domain waveforms. Normally, this can be done very fast using the Fast Fourier Transform (FFT) [91], which is an efficient numerical algorithm to compute the discrete version of the FT expressed in Eq. (3.3) in $\mathcal{O}(N \log N)$ instead of the $\mathcal{O}(N^2)$ arithmetical operations that would be required by making use of its raw definition,

$$\tilde{x}_k = \sum_{j=0}^{N-1} x_j \, e^{-i2\pi \frac{jk}{N}} \qquad \text{where} \begin{cases} x_i \equiv x(t_i) \\ t_i = i \, \Delta t \end{cases} \text{and} \begin{cases} \tilde{x}_k \equiv \frac{1}{\Delta t} \tilde{x}(f_k) \\ f_k = \frac{k}{T_{\text{obs}}} \equiv \frac{k}{N\Delta t} \equiv k \, \Delta f \end{cases} . \tag{3.29}$$

Indeed, the FFT is what shall be used to obtain EOB or NR waveforms in the frequency domain, because the integration process to obtain the time-domain waveforms is much longer than the FFT, and also because these models are normally used to simulate the late-inspiral, merger and ringdown parts of the evolution, where the dynamics are highly relativistic. However, PN waveforms are a whole different story: *(a)* they can be written as closed-form Taylor series, making their evaluation process extremely fast; *(b)* they are valid from $t \to -\infty$ up to a certain point before the last stable orbit, which means that *(i)* the dynamics are in an adiabatic regime and *(ii)* one can generate extremely long PN waveforms starting from the deep-inspiral that will require a huge number of data points to proper sample them in the time-domain. These two reasons make the FFT (for

PN waveforms) a slow process in comparison to the waveform's evaluation time and it is highly recommended to look for an analytical alternative.

The Stationary Phase Approximation (SPA) is a simple, explicit, analytic approximation to the FT of a highly oscillating time-domain signal, such as a chirp. More precisely the SPA is valid when the amplitude and frequency of the signal evolve on time scales much longer than the orbital period: $\epsilon_a = \dot{a}(t)/(a(t)\dot{\phi}(t)) \ll 1$ and $\epsilon_f = \ddot{\phi}(t)/\dot{\phi}^2(t) \ll 1$. For a coalescing binary system, the time scale of evolution of the GW amplitude and frequency is the radiation-reaction time scale so that $\epsilon_a \sim \epsilon_f \sim \nu v^5$ stays much smaller than 1 essentially up to the end of the inspiral.

The SPA is as follows. Let us consider a generic time-domain oscillating signal,

$$h(t) = a(t)\cos\phi(t) = \frac{1}{2}a(t)(e^{i\phi(t)} + e^{-i\phi(t)}) , \tag{3.30}$$

where $\phi(t)$ changes in a time scale much shorter than $a(t)$ and $\dot{\phi}(t) \equiv 2\pi F(t)$. Then, its FT can be computed as [see Eq. (3.3)]

$$\tilde{h}(f) \equiv \int_{-\infty}^{\infty} dt\, h(t)e^{-i2\pi ft} = \int_{-\infty}^{\infty} dt\, \frac{a(t)}{2}\left(e^{i(\phi(t)-2\pi ft)} + e^{-i(\phi(t)+2\pi ft)}\right) . \tag{3.31}$$

The integrands of $\tilde{h}(f)$ are violently oscillating and therefore, their dominant contributions come from the vicinity of the stationary points of their phase (when such points exist). When $F(t) = \frac{\dot{\phi}(t)}{2\pi} > 0$ (which we shall henceforth assume), only the $e^{i(\phi(t)-2\pi ft)} \equiv e^{i\xi(t)}$ term has such saddle point,

$$\frac{d}{dt}(\phi(t) + 2\pi ft) = 0 \;\Rightarrow\; \dot{\phi} = -2\pi f \;\Rightarrow\; 2\pi F(t) = -2\pi f \;\Rightarrow\; F(t) = -f \quad \left[\begin{smallmatrix} \text{not possible} \\ F(t)>0 \end{smallmatrix}\right] ,$$

$$\frac{d}{dt}(\phi(t) - 2\pi ft) = 0 \;\Rightarrow\; \dot{\phi} = 2\pi f \;\;\Rightarrow\; 2\pi F(t) = 2\pi f \;\;\Rightarrow\; F(t) = f \quad [\to t_f] .$$

By expanding $a(t)$ and $\xi(t) \equiv \phi(t) - 2\pi ft$ around the saddle point, t_f [with $\dot{\xi}(t_f) \equiv 0$],

$$a(t) = a(t_f) + \dot{a}(t_f)(t - t_f) + \cdots , \tag{3.32}$$

$$\xi(t) = \xi(t_f) + \cancel{\dot{\xi}(t_f)(t - t_f)} + \tfrac{1}{2}\ddot{\xi}(t_f)(t - t_f)^2 + \cdots , \tag{3.33}$$

we can finally write the well-known expression for the usual SPA:

$$
\begin{aligned}
\tilde{h}(f) &\approx \int_{-\infty}^{\infty} dt\, \tfrac{1}{2}\left[a(t_f) + \dot{a}(t_f)(t - t_f)\right] e^{i[\xi(t_f) + \frac{1}{2}\ddot{\xi}(t_f)(t-t_f)^2]} \quad {}^{[t-t_f\equiv t]} \\
&= \frac{1}{2}e^{i\xi(t_f)}a(t_f)\int_{-\infty}^{\infty} dt\, e^{i\frac{1}{2}\ddot{\xi}(t_f)t^2} + \frac{1}{2}e^{i\xi(t_f)}\dot{a}(t_f)\cancelto{0}{\int_{-\infty}^{\infty} dt\, t\, e^{i\frac{1}{2}\ddot{\xi}(t_f)t^2}} \\
&= \frac{1}{2}e^{i\xi(t_f)}a(t_f)\sqrt{\frac{\pi}{|2\pi\dot{F}|}}\,(1+i) \quad {}^{[\xi=\phi-2\pi ft]} \\
&= \frac{1}{2\sqrt{\dot{F}(t_f)}}\,a(t_f)e^{-i\left(2\pi ft_f - \frac{\pi}{4} - \phi(t_f)\right)} , \qquad (\text{SPA}) \tag{3.34}
\end{aligned}
$$

where we recall that t_f is defined as the saddle point where $F(t_f) = f$.

For GW signals emitted by CBCs, the signal's phase consists in the sum of the GW phase ϕ_{GW}, plus the Doppler φ_{D} and polarization φ_p phases [see Eq. (2.52)]. This also means, that $F(t)$ shall have contributions from the time derivatives of the three components.

The generalization of Eq. (3.34) to a time-domain signal consisting in the sum of several harmonics is straightforward. Let us write the generic time-domain expression as in (2.55), *i.e.* in terms of a signal's phase $\phi(t)$ twice the orbital phase [also the signal's frequency is $F(t) = \frac{\dot{\phi}}{2\pi} = 2f_{\mathrm{orb}}$]; hence the signal $h(t)$ shall be written as

$$h(t) = \sum_j a_j(t) \cos \tfrac{j}{2}\phi(t) \ . \tag{3.35}$$

By applying the same arguments as before, the generic SPA expression for a time-domain signal with multiple harmonics can be written as

$$\tilde{h}(f) \approx \sum_j \left[\frac{1}{2\sqrt{\tfrac{j}{2}\dot{F}(t_f^{(j)})}} a_j(t_f^{(j)}) \, e^{-i\left(2\pi f t_f^{(j)} - \frac{\pi}{4} - \frac{j}{2}\phi(t_f^{(j)}) \right)} \right] \ , \qquad \text{(SPA)} \qquad \tag{3.36}$$

where it is important to note that $t_f^{(j)}$ is different for each harmonic, j, and can be computed as $F(t_f^{(j)}) = 2f/j$. Also notice that in Eq. (3.35) we have included all the phase contributions into $\frac{j}{2}\phi(t)$; by comparison to Eq. (2.55) of a CBC gravitational waveform, we have that

$$\phi(t) \equiv \phi_{\mathrm{GW}} + \tfrac{2}{j}\varphi_{p,j} + \tfrac{2}{j}\varphi_{\mathrm{D}} \ . \tag{3.37}$$

From the definition of $F(t) = \frac{\dot{\phi}}{2\pi}$ we could also obtain its dependency in terms of the physical quantities defined in Chapter 2.

Finally, let us emphasize that this derivations correspond to the SPA just *up to the leading order*, which is more than enough for all the practical purposes that we shall consider in this thesis. However, Damour *et al.* in Ref. [2] [also Droz *et al.* [92]] go beyond the leading order and show that by keeping *two more terms* in both Taylor expansion of Eqs. (3.32) and (3.33), the new SPA expression is simply the same as in (3.34) with a phase correcting factor $e^{i\delta}$, where

$$\delta \equiv \frac{1}{2\pi\dot{F}(t_f)} \left[-\frac{1}{2}\frac{\ddot{a}}{a} + \frac{1}{2}\frac{\dot{a}}{a}\frac{\ddot{F}}{\dot{F}} + \frac{1}{8}\frac{\dddot{F}}{\dot{F}} - \frac{5}{24}\left(\frac{\ddot{F}}{\dot{F}} \right)^2 \right]_{t=t_f} \ . \tag{3.38}$$

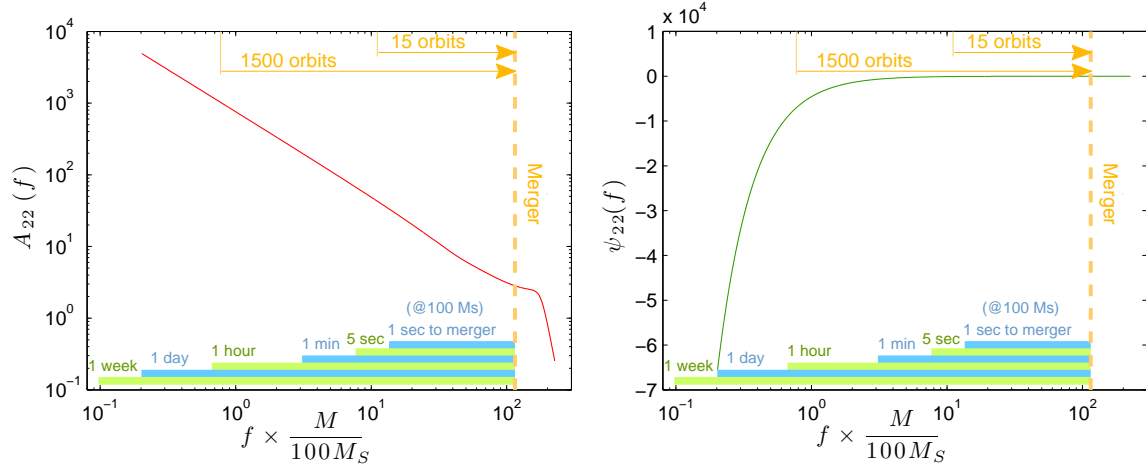## 3.4   Visualizing gravitational waveforms from CBCs

The coalescing process of a compact binary system, when it is still far away from the merger consists in a slow, adiabatic rotation of each of the compact objects around the center of mass of the system. As they approach each other due to the energy emission [mainly in form of GWs], the orbital frequency increases as well as the amplitude of the emitted gravitational signal. Finally, the two compact objects merge to form a single excited Kerr black hole (if their total mass is high enough), which shall still be emitting GWs in a form of quasi-normal modes until it reaches the fundamental state of a Kerr BH. The resulting gravitational waveform emitted in the overall process can be described by a highly oscillating 'chirping' signal [the signal of the dominant mode oscillates with a frequency twice the orbital frequency], *i.e.* whose amplitude and frequency increase with time.
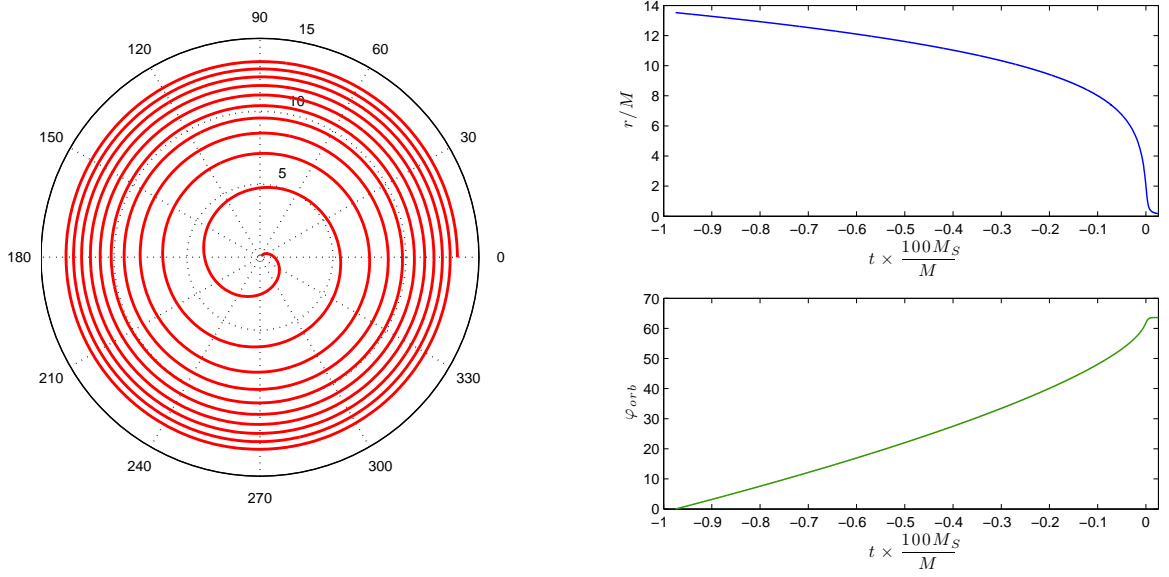
Figure 3.1: Trajectory of the last 10 orbits of an equal-mass, non-spinning BBH system in polar co-ordinates obtained from an EOB simulation. The right panels represent the time evolution of the two polar coordinates (r, φ_{orb}). [Plots: own production, using an EOB simulation courtesy of A. Nagar and T. Damour]
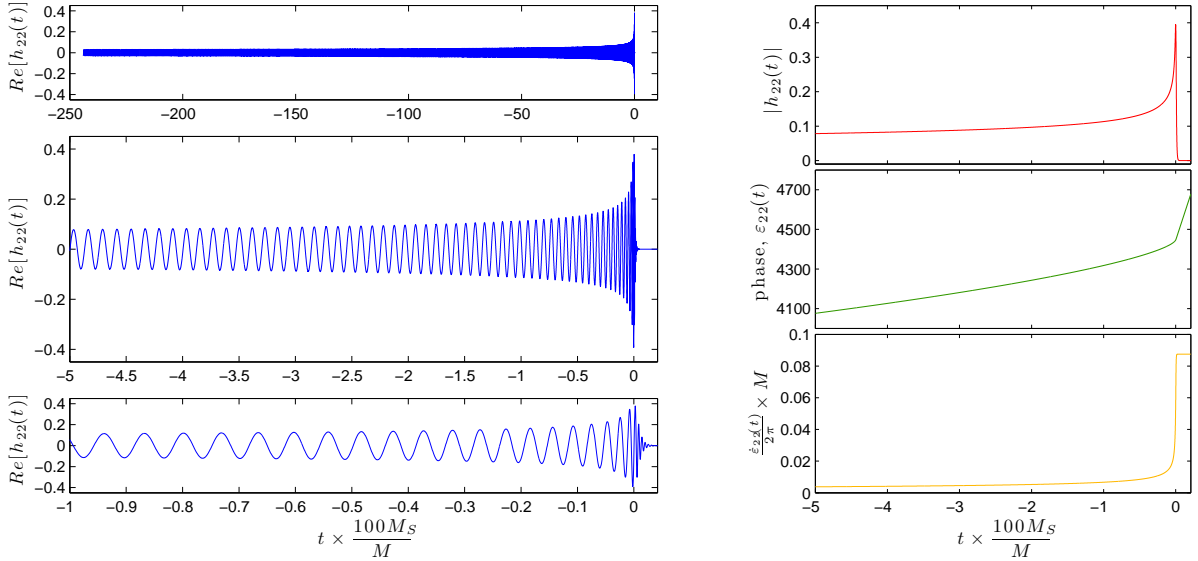
Figure 3.2: Time-domain gravitational waveform emitted by an equal-mass, non-spinning BBH system (see also Fig. 3.1). Left panels represent snapshots of the real part of $h_{22}(t)$ [see Eqs. (2.2) and (2.10)] at three different time range levels; whereas the right panels show the amplitude, phase [see Eq. (2.12) for definition and discussion of $\varepsilon_{\ell m}(t)$] and phase derivative of its $(2,2)$ mode as a function of time. [Plots: own production, using an EOB simulation courtesy of A. Nagar and T. Damour]

Figure 3.3: Frequency-domain gravitational waveform emitted by an equal-mass, non-spinning BBH system (see also Figs. 3.1 and 3.2); in particular, we write $\tilde{h}_{22}(f) \equiv A_{22}(f)e^{-i\psi_{22}(f)}$ [see Eq. (3.4)]. The overprinted segments should help visualizing how 'time' (for $M = 100M_\odot$) and 'number of orbits' ranges translate into the frequency-domain. [Plots: own production, using an EOB simulation courtesy of A. Nagar and T. Damour]

$100M_\odot$	1s	1min	1h	1d	7d	10^{-1} Hz	10^2 Hz
$10M_\odot$	0.1s	6s	6min	2h 24min	16h 48min	1 Hz	1000 Hz
$10^3M_\odot$	10s	10min	10h	10d	2m 9d	0.01 Hz	10 Hz
$10^5M_\odot$	16min 40s	16h 40min	1m 11d	2yr 9m	19yr 2m	10^{-4} Hz	0.1 Hz
$10^7M_\odot$	1d 4h	2m 8d	11yr 5m	275yr	1.9kyr	10^{-6} Hz	10^{-3} Hz
$10^9M_\odot$	3m 24d	19yr	1.15kyr	27kyr	192kyr	10^{-8} Hz	10^{-5} Hz

Table 3.1: All the plots included in Figs. 3.1, 3.2 and 3.3 use the $M = 100M_\odot$ system as reference, *i.e.* we plot $t \times \frac{100M_\odot}{M}$ and $f \times \frac{M}{100M_\odot}$. This table "translates" some of those 'time' and 'frequency' values for different M, keeping t/M and fM fixed. Note that heavier systems have longer time scales and lower emission frequency.

In general, the intrinsic parameters that characterize a BBH coalescence are the total mass of the system M, the mass ratio q and the two spins of the BHs $\mathbf{S_1}$ and $\mathbf{S_2}$. In case of considering NSs or other compact objects with presence of matter, then one has to also consider some extra parameters characterizing its equation of state. In this thesis, we only consider non-spinning BHs (or NSs far away from the merger, where the equation of state parameters are irrelevant) and therefore, the two only intrinsic parameters will be $\{M, q\}$. Moreover, it turns out that after writing Einstein's equations in their adimensional form, the total mass M only plays the role of a *scale factor*, and therefore one considers[5] an *adimensional time*, t/M, an *adimensional frequency*, fM, etc. This means that a certain process that happens in a given amount of (adimensional) time t/M, will be slower in actual 'seconds' as the total mass of the system increases. The opposite happens for the (adimensional) frequency; this is, heavier systems emit at lower frequencies (see Tab. 3.1 and the explanation below for further details).

Figures 3.1, 3.2 and 3.3 graphically represent all the relevant quantities of a CBC process, both, in the time and frequency domains. The results have been generated for a non-spinning, equal-mass system; using the EOB approach [87] to generate the last 1500 orbits prior the merger, plus the merger and ring-down phases [the simulation took ≈ 500 sec running on a single core of a 2.40 GHz Intel Core 2 Duo desktop machine with 2 Gb of RAM]; and joining[6] in front of it the PN-SPA result, which is perfectly valid ~ 1000 orbits before the merger. Assuming a fiducial $M = 100 M_\odot$, the last 10 orbits plotted in Fig. 3.1 would last 1 sec and, as it can be seen in Fig. 3.3, the merger would be emitted at around 100 Hz. Taking into account the fact that the total mass M simply plays the role of a scale factor in Einstein's equations, this time and frequency values can be easily converted to other M values, and this is indeed what has been done in Tab. 3.1. Notice that observable mergers (say, from 15 orbits before merger up to the end) in the LIGO frequency band $(10 - 10^4$ Hz) will correspond to systems with a total mass $M \in [2, 100] M_\odot$ and they will last less than 1 second; considering the LISA band $(10^{-5} - 10^{-1}$ Hz), on the other hand, the systems will have a mass $M \in [2 \times 10^5, 10^8] M_\odot$ and the events will last at least 30 minutes and typically more than a day. These numbers are important to understand some of the approximations made in the previous sections, such as assuming the ground-based detectors antenna patterns (whose variation is due to the Earth's motion) to be constant during the observation time of a merger (see Sec. 2.2.2).

The dependency of the emitted waveforms with the mass ratio q is not straightforward, and one has to run a new simulation every time that changes q. Qualitatively, given a certain separation distance between the compact objects, the evolution is slower [and so is larger the number of orbits before merger] as the mass ratio increases. Figure 3 of Chapter 8 shows an example of amplitudes and phases in the frequency domain of EOB waveforms for $q = \{1, 2, 4, 10\}$ cases.

Also notice, in the right panels of Fig. 3.2, that the most important changes both in frequency and amplitude are produced in the last instants before merger, however the evolution of these two quantities during the whole inspiral stage up to several orbits before merger remains very slow. This slow chirping of the signal during most of the time of the evolution makes the *frequency domain* representation very useful, especially because of its compactness: note, for instance, the simple behavior of $A_{22}(f)$ and $\psi_{22}(f)$ in Fig. 3.3 at

---

[5]We recall that we are always working with units such that $G = c = 1$.
[6]See Section IV of Chapter 8 for further details.

low frequencies and the high number of orbits (and time) that this part represents. Indeed, for data analysis purposes one usually works in the frequency domain.

Although the time-domain amplitude of a chirping signal increases with time, this is not necessarily the case in the frequency domain (see left panel of Fig. 3.3). The reason is because the frequency-domain amplitude represents the amount of energy accumulated in a certain frequency bin; thus, even if one has lower amplitude values in the deep inspiral stage, since the frequency evolution is also much slower, the system remains in that frequency bin for many more orbits, accumulating more energy and therefore having higher frequency-domain amplitudes.

3.5   Effective/characteristic amplitudes and observable sources

In the previous section we have represented and analyzed all the relevant quantities characterizing the gravitational waveform emitted by a CBC (see Figs. 3.1-3.3). We have observed how the frequency-domain representation of the waveform is a much more compact and simpler way to visualize the emission, although one always have to have in mind the highly non-linear relation that exists between the time and frequency. Thus, for instance, a $M = 100 M_\odot$ system needs just 1 second (15 orbits) to increase their emission frequency by an order of magnitude (from 10 Hz to 100 Hz) when it is close to the merger, but it needed ≈ 1 hour (1500 orbits) to go from 1 Hz to 10 Hz. These facts become important when one considers *finite observation times*. The aim of this section is to discuss about the best way to represent the signals' amplitudes together with the detector's sensitivity curves, and quickly get an idea of the expected SNR that a certain signal observed with a given interferometer would have; this is, we shall talk about *effective and characteristic amplitudes*.

This topic was addressed many years ago [2, 93] and several authors proposed different definitions for the effective amplitude depending on the nature of the signal; or, in particular, depending whether the signal is observed as a continuous wave (*i.e.* $T_{\rm obs} \ll$ signal's duration) or a burst-like signal (*i.e.* $T_{\rm obs} \gg$ signal's duration). Since signals from CBCs can be seen in either ways depending on the total mass, luminosity distance and detector, we shall consider here a combination of the various "effective" amplitudes defined in the literature.

The main purpose in defining *effective* quantities is that they have to provide *intuitive information* about the *observed SNR*. Let us start recalling which is the definition of the optimal SNR (squared) given a certain waveform, h, in terms of the frequency domain signal and the noise PSD [see Eq. (3.10)],

$$\rho_{\rm opt}^2 = (h|h) = 4 \int_{F(t_0)}^{F(t_0+T_{\rm obs})} {\rm d}f \, \frac{|\tilde{h}(f)|^2}{S_n(f)} = \int_{F(t_0)}^{F(t_0+T_{\rm obs})} \frac{{\rm d}f}{f} \, \frac{f^2|\tilde{h}(f)|^2}{\frac{f}{4}S_n(f)} \; . \qquad (3.39)$$

Here, we have explicitly written the integration intervals for a given finite observational time, $T_{\rm obs}$, starting the observation at t_0, and $F(t)$ being the GW frequency [here we only consider the $(2, 2)$ mode, though the extension to higher harmonics would be straightforward]. Moreover, on the r.h.s. of Eq. (3.39) we have rewritten the integral expression of the optimal SNR so that each of the terms are adimensional:

- First, we have written the integral over the (adimensional) logarithmic frequency, $\frac{\mathrm{d}f}{f} = \mathrm{d}\log f$, so that in the usually represented *log-scale plots*, integrals shall be intuitively computed as the '*area below the integrand*'.

- Despite the time-domain GW amplitude, $h(t)$, being adimensional [as it represents the relative length changes of the two interferometer arms, see Eq. (2.32)]; the definition of the Fourier transform, Eq. (3.3), adds units of time to the frequency-domain signal, $\tilde{h}(f)$. Hence, $f^2|\tilde{h}(f)|^2$ is adimensional and we shall define it as the (squared) *effective gravitational signal* [2],

$$h_s^2(f) \equiv f^2|\tilde{h}(f)|^2 \ . \qquad (\textit{effective signal}) \qquad (3.40)$$

- Finally, the detector noise PSD, $S_n(f)$, has also units of time, which will cancel out when it is multiplied by f. The factor $\frac{1}{4}$ comes from the fact that we are considering *one-sided* noise PSDs [the two-sided noise PSD would have just a factor $\frac{1}{2}$]. Thus, we define the *effective GW noise* [2] (or, also called *characteristic noise amplitude* [93]) as

$$h_n(f) \equiv \sqrt{\tfrac{f}{4}S_n(f)} \ . \qquad (\textit{effective noise} \text{ or } \textit{characteristic noise}) \qquad (3.41)$$

With these definitions, the optimal SNR (squared), given in Eq. (3.39), can be written simply as the logarithmic frequency integral of the squared ratio of the (adimensional) effective signal and noise,

$$\rho_{\mathrm{opt}}^2 = \int_{F(t_0)}^{F(t_0+T_{\mathrm{obs}})} \frac{\mathrm{d}f}{f} \ \frac{h_s^2(f)}{h_n^2(f)} \ . \qquad (3.42)$$

Now, the usefulness of the ratio $\frac{h_s}{h_n}$ as indicator of the SNR will depend of the frequency variation during the observational time. If one considers a *CBC signal in the last stages of the evolution* (with a significant frequency variation) and observed for a sufficient long time so that the frequency changes by, at least, one of order of magnitude, then the ratio of effective signal and noise will provide an intuitive idea of the optimal SNR. However, if one considers a *quasi-monochromatic signal* (*e.g.* a CBC in the deep inspiral phase), then the frequency variation during T_{obs} will be negligible, so the integrand will be almost constant and the result of the integral in Eq. (3.42) will basically be $\Delta(\log F) \times (\frac{h_s}{h_n})^2$ with $\Delta(\log F) \equiv \log\frac{F_{\mathrm{end}}}{F_0} \ll 1$ and therefore $(\frac{h_s}{h_n})^2 \gg \rho_{\mathrm{opt}}^2$.

For cases like the latter, namely $\Delta(\log F) \ll 1$; it is far more useful to work with *characteristic* quantities [93], rather than the effective ones defined in (3.40). In particular, the *characteristic noise* is equal to the effective noise [see Eq. (3.41) above] and since we are integrating it in a narrow frequency band, it can be taken as constant and factorized out of the integral. The remaining part is defined as the (squared) *characteristic signal amplitude*,

$$h_c^2(f) \equiv \int_{F(t_0)}^{F(t_0+T_{\mathrm{obs}})} \frac{\mathrm{d}f}{f} h_s^2(f) = \int_{F(t_0)}^{F(t_0+T_{\mathrm{obs}})} \frac{\mathrm{d}f}{f} f^2|\tilde{h}(f)|^2 \ . \qquad (\textit{characteristic signal})$$

$$(3.43)$$

Then, the *characteristic frequency* can be computed as

$$f_c \equiv \frac{\int_{F(t_0)}^{F(t_0+T_{\mathrm{obs}})} \frac{\mathrm{d}f}{f} f^2|\tilde{h}(f)|^2 f}{\int_{F(t_0)}^{F(t_0+T_{\mathrm{obs}})} \frac{\mathrm{d}f}{f} f^2|\tilde{h}(f)|^2} \ . \qquad (3.44)$$

Characteristic:	$h_c^2(F_0) \equiv \int_{F_0}^{F_{\text{end}}} \frac{df}{f} f^2 |\tilde{h}(f)|^2$	;	$(F_{\text{end}} \approx F_0)$;	$\rho_{\text{opt}}^2(F_0) \approx \left[\frac{h_c(F_0)}{h_n(F_0)} \right]^2$
Effective:	$h_s^2(f) \equiv f^2 |\tilde{h}(f)|^2$	;	$(F_{\text{end}} \gg F_0)$;	$\rho_{\text{opt}}^2(F_0) \approx \int_{F_0}^{\infty} \frac{df}{f} \left[\frac{h_s(f)}{h_n(f)} \right]^2$

Table 3.2: Summary of the *characteristic* and *effective signals*: definition, range of applicability and relation to the optimal SNR. See discussion in Sec. 3.5 for further details; we recall that the effective (or characteristic) noise amplitude is defined in (3.41): $h_n(f) \equiv \sqrt{\frac{f}{4} S_n(f)}$.

Under these assumptions of narrow frequency band, the optimal SNR is simply the ratio of characteristic signal and noise,

$$\rho_{\text{opt}}^2 = \frac{h_c^2(f_c)}{h_n^2(f_c)} \ . \qquad \text{(when } \Delta(\log F) \ll 1) \qquad (3.45)$$

In conclusion, effective and characteristic signals and noise consist in a more useful way to (graphically) represent amplitudes and noise levels, respectively; first, because they are adimensional and second, because their ratio is directly related with the observed optimal SNR.

- When we are considering signals whose frequency evolution during the observational time can be actually appreciated in a log-scale plot spanning several orders of magnitude (for instance, Fig. 3.3), then we shall plot the *effective signal amplitude* (3.40) together with the effective noise, h_n^2 (3.41) and their squared ratio will represent the integrand [over the log-frequency] of ρ_{opt}^2 (3.42); the integral can be estimated as the area below the curve, assuming the $\log f$ variable as the base.

- On the other hand, when the frequency evolution (during a given observational time) is too small to be appreciated in a '$\log f$' plot, then we shall compute the SNR integral beforehand (assuming the effective noise level to be constant during that interval), resulting into the *characteristic signal amplitude* (3.43); then, the optimal SNR will be just the ratio between the characteristic signal and the effective noise (3.45).

When considering GW signals from CBCs, it turns out that the same gravitational signal can be in either of the two regimes, depending on the observational time and, mainly, on the stage of the evolution that is being observed. Moreover, given the "abrupt" transition in the frequency evolution close to the merger (see, for instance, bottom-right panel of Fig. 3.2), the transition zone between the two regimes will be very narrow. Hence, we shall normally be observing either [Table 3.2 provides a summary of this discussion]

1. inspiral, quasi-monochromatic signals with $F_0 \equiv F(t_0) \approx F(t_0 + T_{\text{obs}}) \approx f_c$ and that will be represented by their characteristic signal, $h_c(F_0)$; or

2. the late-inspiral *and* the whole merger and ringdown stages of the coalescence, in which case, the frequency can vary by several orders of magnitude and hence, the effective signal, $h_s(f)$, is providing a better representation of the signal (in terms of relating it to the SNR). In this case, since the coalescences are observed until the end, the upper limit of integration in Eq. (3.42), $F(t_0 + T_{\text{obs}}) \equiv F_{\text{end}}$, can be replaced by infinity.

In the intermediate (and narrow) zone where $\Delta(\log F) > 1$ but not by too much [in CBCs, when $t_0 + T_{\text{obs}} \approx t_{\text{merger}}$ and $F(t_0 + T_{\text{obs}}) \not\to \infty$], the two representations (effective and characteristic) will still be valid within their definitions, *i.e.* the (squared) ratio of effective quantities as integrand and the (squared) ratio of characteristic amplitudes as integral expressions of the SNR^2. Of course, they are not going to numerically coincide, as they represent different quantities[7], besides that each of them will have its own limitations in that zone: *(i)* for characteristic amplitudes, as we go to higher frequencies, $h_c(F_0)$ will represent an integral between a wide interval $[F_0, F_{\text{end}}]$ and the factorization of noise level out of the integral as $h_n(F_0)$ will start being no longer valid; and *(ii)* for effective amplitudes, as we go to lower frequency values, the upper limit of the integral will not be infinity anymore, and $\Delta(\log f)$ will start being sufficiently small to make computation of the (now, very narrow) area below the curve less intuitive. The point where $h_c = h_s$, despite not having any special meaning, will be in this intermediate zone and it will represent the frequency F_0 value where the 'effective' $\Delta \log F = 1$, *i.e.* $F_{\text{end}}/F_0 \sim e$.

3.5.1 Analytical calculations within the Newtonian approximation

Before analyzing the effective and characteristic amplitudes obtained from the full EOB waveforms already plotted in Figs. 3.1, 3.2 and 3.3, it is very interesting to start analyzing what kind of behavior do we expect. This can be easily (and analytically) done by just taking the solution of the CBC dynamics to the leading Newtonian order [3]. This is,

$$|\tilde{h}(f)| = \sqrt{\frac{5\pi}{24}}\frac{\nu^{1/2}M^2}{D_{\text{eff}}}(\pi f M)^{-7/6} \equiv |A|f^{-7/6} ; \tag{3.46}$$

$$F(t) = \frac{\theta^3}{8\pi M} , \qquad \text{where} \quad \theta = \left[\frac{\nu}{5M}(t_{\text{ref}} - t)\right]^{-1/8} ; \tag{3.47}$$

$$t(F) = t_{\text{ref}} - \frac{5M}{256\nu \text{v}^8} , \qquad \text{where} \quad \text{v} = (\pi F M)^{1/3} . \tag{3.48}$$

In the previous equations, F is the GW frequency, M the total mass, $\nu = \frac{m_1 m_2}{M^2}$ the symmetric mass ratio and t_{ref} represents the (reference) time such that the PN GW frequency diverges; of course this divergence does not occur when one considers full Einstein's equations, hence the PN validity range always ends well before t_{ref}.

Effective and characteristic amplitudes

The *effective* amplitude signal, h_s, is simply $|\tilde{h}(f)|$ times f, so

$$h_s^2(f) = f^2|\tilde{h}(f)|^2 = f^2|A|^2 f^{-7/3} = |A|^2 f^{-1/3} . \qquad (Newtonian) \tag{3.49}$$

The computation of the *characteristic* signal, h_c, actually involves an integral (3.43). We shall consider two limit cases. On the one hand, we assume that we are close enough to the merger so that $F_{\text{end}} \equiv F(t_0 + T_{\text{obs}}) > F_{\text{merg}}$ and it can be considered as infinite,

$$h_c^2(F_0) = \int_{F_0}^{\infty} \frac{\mathrm{d}f}{f}|A|^2 f^{-1/3} = 3|A|^2 F_0^{-1/3} = 3h_s^2(F_0) . \qquad (Newtonian; F_{\text{end}} \to \infty) \tag{3.50}$$

---

[7]In fact, we shall see that in the Newtonian limit and assuming $F(t_0 + T_{\text{obs}}) \to \infty$, the two signal amplitudes are related as $h_c^2 = 3h_s^2$; see Eq. (3.50).

On the other hand, we can consider a system in the inspiral stage of the evolution, with small frequency variations, $\Delta(\log F) \ll 1$,

$$
\begin{aligned}
h_c^2(F_0) &= \int_{F(t_0)}^{F(t_0+T_{\mathrm{obs}})} \frac{\mathrm{d}f}{f} |A|^2 f^{-1/3} \\
&= 3|A|^2 \left[F(t_0)^{-1/3} - F(t_0+T_{\mathrm{obs}})^{-1/3} \right] \\
&= 3|A|^2 (8\pi M)^{1/3} \left(\frac{\nu}{5M} \right)^{1/8} (t_{\mathrm{ref}}-t_0)^{1/8} \left[1 - \left(1 - \frac{T_{\mathrm{obs}}}{t_{\mathrm{ref}}-t_0} \right)^{1/8} \right] \\
&\approx 3|A|^2 (8\pi M)^{1/3} \left(\frac{\nu}{5M} \right)^{1/8} (t_{\mathrm{ref}}-t_0)^{1/8} \frac{1}{8} \frac{T_{\mathrm{obs}}}{t_{\mathrm{ref}}-t_0} \\
&= [\cdots] = \frac{4\nu^2}{D_{\mathrm{eff}}^2} \frac{MT_{\mathrm{obs}}}{\pi} (\pi F_0 M)^{7/3} \ ;
\end{aligned}
$$

finally,

$$
h_c(F_0) = \frac{2\nu}{D_{\mathrm{eff}}} \left(\frac{MT_{\mathrm{obs}}}{\pi} \right)^{1/2} (\pi F_0 M)^{7/6} \ . \qquad (\textit{Newtonian}; \ \Delta(\log F) \ll 1) \qquad (3.51)
$$

To summarize, the effective signal, $h_s(F_0) \overset{\mathrm{NWT}}{\propto} F_0^{-1/6}$, provides intuitive information in cases where there is a significant frequency change (in CBCs, when the observational time includes the merger and ringdown, $F_{\mathrm{end}} > F_{\mathrm{merg}}$), whereas the characteristic signal amplitude, $h_c(F_0) \overset{\mathrm{NWT}}{\propto} F_0^{7/6}$, shall be used to represent quasi-monochromatic signals in the (deep) inspiral regime. In the transition zone, where $F(t_0+T_{\mathrm{obs}}) \approx F_{\mathrm{merg}}$, both representations [with their respective meanings] will be valid and indeed, in Eq. (3.50) we see how h_c^2 will end up being $3h_s^2$.

Transition and Last-Stable-Orbit zones

Given a certain observational time, T_{obs}, we shall start observing the merger stage of the evolution when $F(t_0+T_{\mathrm{obs}}) = F_{\mathrm{merg}}$. The $F_0 \equiv F(t_0)$ value associated with this condition, let us call it $\tilde{F}_0$, will define the "transition zone" between considering quasi-monochromatic signals [and therefore, using h_c] to considering observations up to the end of the ring-down [and using h_s]. We can compute these $\tilde{F}_0$ values within the Newtonian approximation by using Eq. (3.47) and assuming the PN merge to occur at t_{ref},

$$
\tilde{F}_0 \equiv F(t_{\mathrm{ref}} - T_{\mathrm{obs}}) = \frac{1}{8\pi M} \left(\frac{\nu}{5M} T_{\mathrm{obs}} \right)^{-3/8} = \frac{1}{8\pi M^{5/8}} \left(\frac{5}{\nu \, T_{\mathrm{obs}}} \right)^{3/8} \ . \qquad (3.52)
$$

The effective amplitude associated to these $\tilde{F}_0$ values, will be

$$
h_s(\tilde{F}_0) = \frac{5}{32\pi^2 D_{\mathrm{eff}}} \frac{1}{\sqrt{6T_{\mathrm{obs}}}} \tilde{F}_0^{-3/2} \ . \qquad (\textit{Newtonian}) \qquad (3.53)
$$

Notice that all the dependency on M and ν remains implicit within $\tilde{F}_0$, so we shall be getting the same 'transition curves' for all (ν, M) values (see Fig. 3.4).

Also, we can obtain the effective amplitude associated to the (test-mass particle) LSO, which is given by $v_{\mathrm{LSO}} = 1/\sqrt{6}$ or, in other words, $F_{\mathrm{LSO}} = 1/(6^{3/2}\pi M)$,

$$h_s(F_{\mathrm{LSO}}) = \sqrt{\frac{5\nu}{\pi^3}} \frac{1}{6^{3/4}} \frac{1}{12 D_{\mathrm{eff}}} F_{\mathrm{LSO}}^{-1} . \qquad (Newtonian) \qquad (3.54)$$

The previous expression has already been written explicitly in terms of F_{LSO}, but there still remains a dependency on ν that will give different 'LSO curves' depending on the mass ratio. We also considered the possibility of using the mass-ratio-dependent expression for the LSO given in Ref. [1], but the results we were obtaining were too complicated.

3.5.2 Plotting the effective/characteristic amplitudes

After defining which are the most appropriate quantities to intuitively represent signal and noise amplitudes, let us now take the frequency-domain amplitude of the gravitational waveform plotted in Fig. 3.3 [corresponding to an EOB simulation of an equal-mass, non-spinning BBH system including all stages of the evolution], and compute its associated effective and characteristic amplitudes. Results considering a fiducial effective distance of $D_{\mathrm{eff}} = 1$ Gpc, an observational time of $T_{\mathrm{obs}} = 1$ year and several total mass values, are plotted in Fig. 3.4.

In particular, we consider twelve different total mass values, $M/M_\odot = \{3, 15, 50, 200, 1000, 10^4, 5 \times 10^4, 3 \times 10^5, 2 \times 10^6, 10^7, 5 \times 10^7, 3 \times 10^8\}$; which basically respond to a log-scale uniform grid from stellar-mass systems up to supermassive ones. However, there are some of the intermediate values that correspond to systems that have never been observed in the Universe: from stellar evolution we know that BHs up to $20 M_\odot$ [94] can exist and also, there are strong evidences to accept the presence of SMBHs in the center of every Galaxy with individual masses above $\sim 10^4 M_\odot$. Hence, for equal-mass CBCs there is a total mass range $M \in (40 M_\odot, 2 \times 10^4 M_\odot)$, where it is unknown whether these systems can actually exist; we denote them as lighter blue curves in Fig. 3.4.

The evolution of the amplitude curves with the total mass of the system M, that can be observed in Fig. 3.4, can be easily understood as a combination of two effects: on one hand, the signal's amplitude increases with M, as $|\tilde{h}(f)| \propto M^{5/6}$ [see Eq. (3.46)]; on the other hand, the amplitude curves shift to lower frequencies as M increases, since the solution to Einstein's equations is generally obtained in terms of the adimensional frequency, fM.

The orange thick lines plotted in the same figure represent the transition zone from where $F_{\mathrm{end}} = F(t_0 + T_{\mathrm{obs}}) > F_{\mathrm{merg}}$, i.e. if the observation starts at some point in the right hand side of the orange line, it means that one shall observe the whole coalescing process up to merger within T_{obs}. The green thick line, on the other hand, represents the merger position (defined as the instant where the time-domain amplitude becomes maximum). Both loci have been numerically computed using the EOB waveform, but we observe that their general behavior is consistent with the analytical calculations done within the Newtonian approximation in the previous section: Eqs. (3.53) and (3.54), respectively. Also, the general trends of the effective and characteristic amplitudes, h_s and h_c, during the inspiral stage of the evolution are in concordance with the Newtonian predictions, Eq. (3.49) and (3.51), respectively. In particular, we recall that the effective amplitude, h_s, consists simply in an adimensionalization of the original amplitude and it still decreases
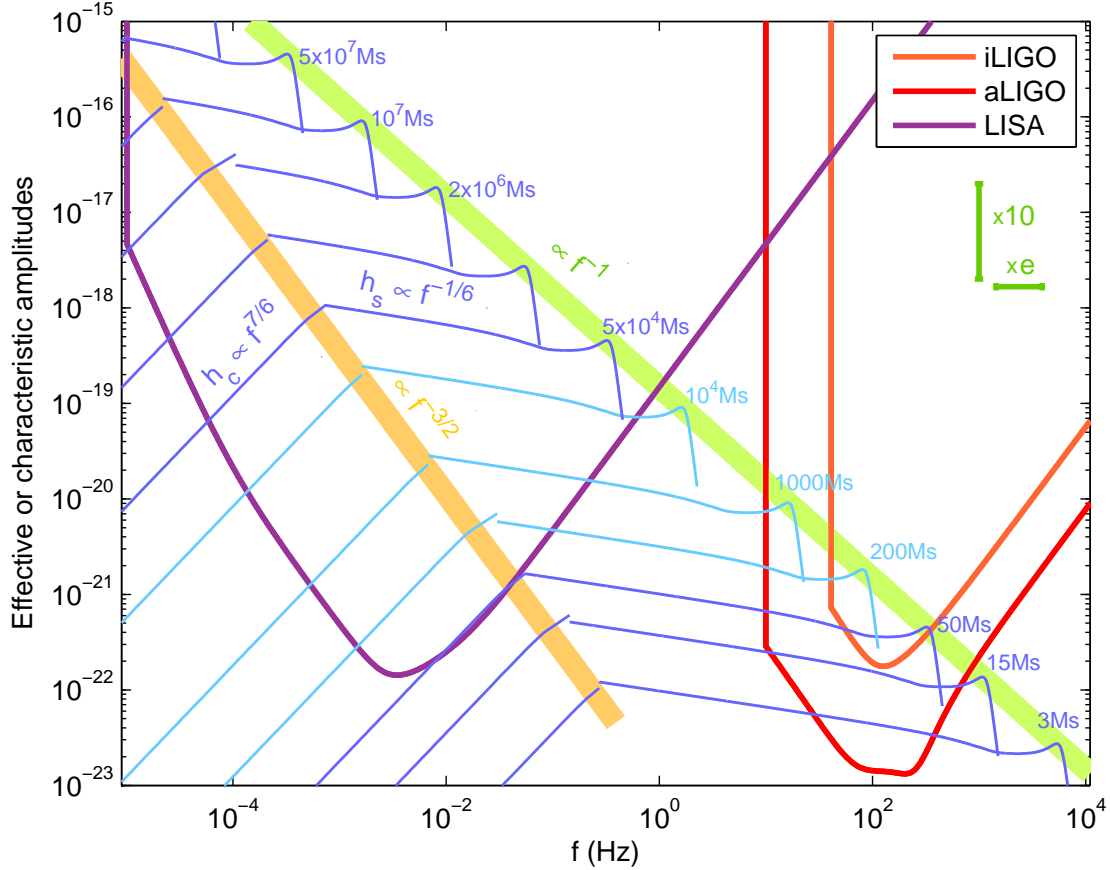
Figure 3.4: Summary plot of the detectability of (equal-mass) CBCs (of any total mass) with current and future interferometric GW detectors. The thick green line represents the locus where the merger (defined as the instant where the time-domain amplitude is maximum) occurs, for different total mass values; whereas the thick orange line represents the frequency and amplitude values such that $F(t_0 + T_{\text{obs}}) = F_{\text{merg}}$, assuming $T_{\text{obs}} = 1$ yr; in other words, it represents the transition zone of usefulness of the characteristic and effective signals definitions (see discussion and further details in the main text). In particular, the blue lines (both light and dark blue) represent characteristic signal amplitudes, h_c, in the left hand side of the thick orange line and effective amplitudes, h_s, in the right hand side; always considering equal-mass systems at a fiducial effective distance of $D_{\text{eff}} = 1$ Gpc and twelve different total mass values, $M/M_\odot = \{3, 15, 50, 200, 1000, 10^4, 5 \times 10^4, 3 \times 10^5, 2 \times 10^6, 10^7, 5 \times 10^7, 3 \times 10^8\}$. The darkness level of the blue lines gives an idea of the odds of finding this kind of systems in the Universe. We also overprint the effective noise amplitude, h_n, of both ground- and space-based interferometric GW detectors. Finally, the green segments on the top-right corner give an idea of what a factor 10 and e are in the 'y' and 'x' axis, respectively. [Plot: own production, using an EOB simulation courtesy of A. Nagar and T. Damour]

(a) $D_{\text{eff}} = 0.15$ Mpc
[Galactic realm]

(b) $D_{\text{eff}} = 30$ Mpc
[Virgo supercluster]

(c) $D_{\text{eff}} = 6.3$ Gpc; ($z = 1$)
['cosmological' distances]
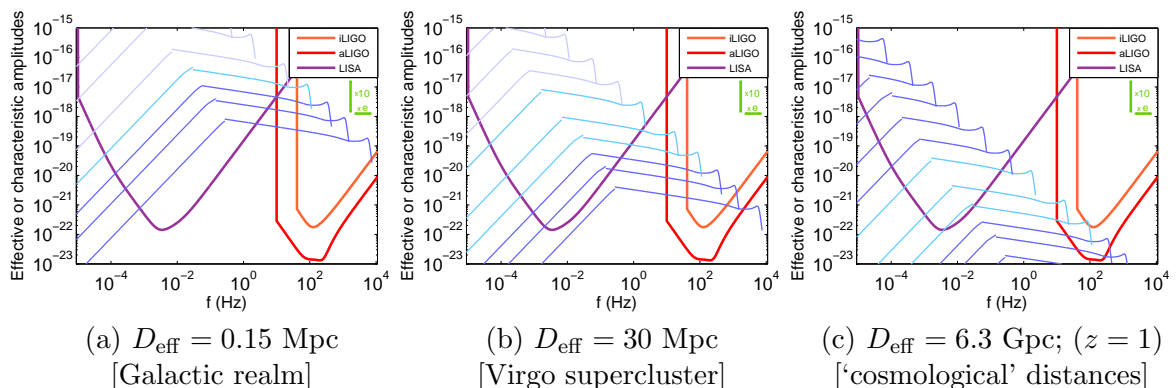
Figure 3.5: Similar plots to Fig. 3.4, but considering three particular effective distance values, D_{eff}, that represent the typical size of astronomical structures that contain the Solar System within. We use three different darkness levels for the (blue) signal's amplitude curves, in order to represent (in an approximate and qualitative way) the odds of having CBCs of such total mass, M, within the different volumes. We consider the same twelve M values as in Fig. 3.4. [Plots: own production, using an EOB simulation courtesy of A. Nagar and T. Damour]

with frequency; however, the characteristic amplitude h_c represents already an integrated quantity over a fixed T_{obs}. So, despite the fact that the original amplitude in the frequency-domain was higher at lower frequencies, the frequency variation (for a fixed T_{obs}) becomes smaller as one moves to smaller frequency values, making the integral expression, h_c, to decrease as we move to lower frequencies.

As we have seen in Sec. 3.4, the emission frequency of a CBC is monotonically increasing, but not at a constant rate, very slowly in the early stages of the evolution and much faster as one gets close to the merger. In terms of the amplitude curves represented in Fig. 3.4, this one-to-one relation between frequency and time means that *any coalescing binary system* (with a fixed total mass[8], M) *moves along a single line during its lifetime*: the higher the frequency is, the closer to the merger. Furthermore, the increase on the frequency derivative as the system approaches the merger, translates into a changing velocity of how the system moves along the amplitude curves. For instance, by definition any system spends $T_{\text{obs}} = 1$ yr to go from the orange line up to merger, but during this very same time, when the system is at some point at the l.h.s. of the orange line, one can not even notice the frequency variation. Indeed, at the l.h.s. of the orange line we can find systems that are from millions of years, up to one year, prior their merger; whereas at the r.h.s. all systems have less than one year left of life time. This is very important in order to understand the population distribution of sources along the amplitude curves: *if we assume a uniform distribution of CBC ages, we shall expect millions of times more sources at the l.h.s. of the orange thick line than at the r.h.s.*

In the same plot in Fig. 3.4, we also show the effective (or characteristic) noise amplitudes of both ground and space based GW interferometric detectors, in particular *initial LIGO* [95], *advanced LIGO* [95] and *LISA* [96].

With all the information presented in a figure like Fig. 3.4 and undestanding the meaning of effective and characteristic amplitudes (see Tab. 3.2 for a summary), one can easily obtain

---

[8]If we assume that the emitted energy is small compared with the total mass of the system; which is not true in reality.

very useful information about *(i)* the systems that will be observable in each detector, *(ii)* which parts of the coalescing process will be visible and *(iii)* the typical SNR values at a given effective distance. Given the inverse proportional relation between $\tilde{h}(f)$ and D_{eff}, an increase of an order of magnitude in the effective luminosity distance would represent a decrease on both effective and characteristic signals by the same factor. In particular, assuming a fiducial effective distance of 1 Gpc as it is done in Fig. 3.4 [which represents a volume $\sim 10^4$ larger than the size of the Virgo supercluster]; we see that Adv. LIGO could observe the late inspiral of a system with $M = 15 M_{\odot}$ and the merger would become visible for higher mass systems, such as $M = 50 M_{\odot}$ and $M = 200 M_{\odot}$. LISA, on the other hand, would be able to observe the quasi-monochromatic signals from the deep inspiral regime of systems with $M \in (200 M_{\odot}, 10^7 M_{\odot})$ and the actual mergers of systems with $M > 5 \times 10^4$. Moreover, the expected SNRs observed by LISA would be much higher that what we expect in ground-based detectors.

The effective distance considered in Fig. 3.4 is arbitrarily chosen. In fact, we think that somehow one can obtain even more useful information when one considers astronomically motivated D_{eff} values and also total mass ranges according to the expected population. Indeed, this study is what it is done in Fig. 3.5, considering three different scenarios: *(a)* the Galactic realm [$D_{\text{eff}} = 0.15$ Mpc], *(b)* the Local (Virgo) supercluster [$D_{\text{eff}} = 30$ Mpc] and *(c)* 'cosmological' distances [$D_{\text{eff}} = 6.3$ Gpc]. With these plots and some astronomical arguments, we shall be able to predict which are the gravitational signals generated from (similar-mass) CBCs that are expected to be observed in the ground-based or space-based frequency bands, and also their properties and origin.

- *Galactic realm.* Massive BHs are located at the center of galaxies [97–99] (for instance, we know that there is a $4.5 \times 10^6 M_{\odot}$ SMBH at the center of our galaxy, see *e.g.* [100]), so massive events will be related to galaxy mergers [101] and we do not expect such events at distances of the order of the Milky Way scale and neither in the Local supercluster [thus, in Fig. 3.5a-b we shall represent these systems with the lightest blue color]. What we do expect is to have an important population of stellar-mass BHs generated as the end product of massive stars evolutions. An small fraction of these BHs can be in binary systems and therefore emit GWs.

  In principle, we see that the same systems could be observed by LISA in their deep-inspiral stage (with SNRs from tens up to hundreds) and also by LIGO when they are close to the merger (SNR $\sim 100 - 1000$). The coalescence rate of BBH systems is 0.4 Myr^{-1} per Milky Way Equivalent Galaxy [95], so we do not expect to observe any BBH merger from our galaxy; however LISA will observe such systems (indeed, millions of them) in an early stage of their evolution, where they remain for a very long time and therefore, they have a much greater population.

  Thus, the only (similar-mass) CBCs that we expect to observe from our galaxy are stellar-mass objects in their deep inspiral stage of the evolution, emitting quasi-monochromatic signals; we shall refer to them as *galactic binaries*. Despite being a CBC, they are too far away from merger that their gravitational waveform for $T_{\text{obs}} = 1$ yr, can be modeled as a monochromatic signal plus an spin-up parameter representing the first frequency derivative. Galactic binaries are by far the most numerous among LISA sources, and indeed most of them will be unresolvable becoming an extra source of noise, so-called *confusion noise*. Trying to resolve them represents one of the major challenges for LISA data analysis, not only in order to obtain individual information from them, but also to remove them from the data and therefore

reduce the confusion noise that also affects other LISA sources. We expect to be able to identify several thousands of such systems during LISA's mission life time.

In this thesis, we have developed MCMC-based methods to search for a fixed number of galactic binary signals buried in LISA noise, and also we have participated in the Mock LISA Data Challenges (MLDC) [102, 103]. (see Chapters 6 and 7 for further details).

- *Local (Virgo) supercluster.* We don't expect to observe any SMBH binary merger event coming from the Local supercluster neither, but having increased the volume by a factor 8×10^6 compared to the Galactic realm increases the chances to observe stellar-mass BBH mergers. Indeed, the expected CBC signals to be observed by ground-based detectors will be located within the Local supercluster and even a bit beyond. We observe in Fig. 3.5b how the expected SNR is still high enough to make observations and the CBC rates start being close to 1 yr^{-1}. In particular, recently in Ref. [95] the LIGO and Virgo Collaborations have revisited the issue of predictions for the rates of CBC observable by ground-based detectors, assuming horizon distances of 161 Mpc/2187 Mpc for BH-BH inspirals in the Initial/Advanced LIGO-Virgo networks, and obtaining detection rates of 0.007 yr^{-1}/20 yr^{-1}, respectively. Notice that for very low mass systems ($M \lesssim 10 M_\odot$) only the late inspiral part of the waveform will be observable, but as we increase a little bit the total mass, the merger part becomes relevant. Indeed, this has been the main motivation for scientists working on Numerical and Analytical Relativity problems over the last years in order to obtain an accurate description of the dynamics of CBC systems around the merger. Indeed, part of the work done during this thesis has been devoted to study the performance (in terms of accuracy and effectualness) of the (fast) closed-form, frequency domain waveform models in comparison to the slower, but more accurate, EOB templates, see Chapter 8; with this study we get to know the range of applicability of the fastest waveform models, either for detection or measurement purposes.

  Part of the extragalactic stellar-mass compact systems in the deep-inspiral regime are still visible in the LISA band and indeed, there is also an extragalactic component of *confusion noise*. However, looking at Fig. 3.5b, at these distances, one has to consider somehow high M values in order to obtain 'observable' (> 10) SNR values, and the LISA noise curve plotted here does not contain the contribution from confusion noise. In conclusion, there is an extragalactic component to the confusion noise, but we do not expect to individually resolve any extragalactic stellar-mass binary.

- *'Cosmological distances'.* Assuming a spatially flat Friedman-Lemaître-Robertson-Walker (FLRW) universe with $H_0 = 75$ km $\mathrm{s}^{-1}\mathrm{Mpc}^{-1}$, $\Omega_M = 0.27$, $\Omega_{DE} = 0.73$, and $w = -1$, a luminosity distance of $D_{\mathrm{eff}} = 6.3$ Gpc corresponds to a redshift $z = 1$; and we could even consider longer distances, such as $D_{\mathrm{eff}} = 15$ Gpc ($z = 2$), $D_{\mathrm{eff}} = 45$ Gpc ($z = 5$) or $D_{\mathrm{eff}} = 100$ Gpc ($z = 10$). In Fig. 3.5c, we see that LISA will be able to observe massive and supermassive BBHs coalescences from any mass within $M \in (10^4 M_\odot, 10^8 M_\odot)$, at almost any distance, with SNRs of hundreds and even thousands. In most of the systems, the merger part can have a significant contribution to the SNR (if T_{obs} is long enough), so it will be also important to include information from either EOB or NR simulations. Given the fact that the detection problem of SMBHs signals with LISA is relatively easy [because of the high SNR values]; during the past years, data analysts have focussed on parameter estimation

studies. In particular, one of the main topics of this thesis (Chapter 4) have been to study the impact on parameter estimation of adding the higher harmonics of the orbital frequency to the inspiral PN signal, finding significant improvements on relevant parameters.

With long observational times ($\sim$ months), one of the parameters that LISA can directly measure is the luminosity distance. This is not normally the case with other (electromagnetic) astronomical measurements, where one obtains accurate measurements of the redshift by looking at the emitted spectra, but it is very hard to directly measure luminosity distances. This LISA's feature, combined with the fact that it will observe SMBHs coalescence events from anywhere in the Universe, makes the spaced-based detector a powerful tool to do cosmography. In particular, during the thesis, we have studied LISA's performance in measuring the dark energy equation of state from a single SMBHs inspiral event at $z \leq 1$ (Chapter 5).

Advanced ground-based detectors and, specially, the planned third generation of interferometers, might also observe some merger events at 'cosmological distances', $D_{\mathrm{eff}} \sim$ Gpc. We can see in Fig. 3.5c how the late inspiral, merger and ringdown parts of the waveform will have a key role in these observations; thus, the better our understanding of the signals emitted in that regime is (including higher harmonics, spins, precession, etc.), the better the cosmological outstanding of the advanced ground-based detectors will be.

In conclusion, LISA will observe thousands of stellar-mass BBHs coalescences from our galaxy when they are still in the deep-inspiral stage of the evolution (galactic binaries), *i.e.* emitting quasi-monochromatic signals; also it will observe SMBHs inspirals and mergers from almost any place of the Universe [up to $z = 10 - 15$]. Ground-based detectors, on the other hand, will observe the late inspiral, merger and ringdown phases of stellar-mass and up to several hundreds of solar masses CBCs produced within ~ 150 Mpc (2000 Mpc), when one considers Initial (Advanced) detectors; this represents a volume ~ 100 (10^5) times larger than the Virgo supercluster.

References

[1] T. Damour, B. R. Iyer, B. S. Sathyaprakash, Phys. Rev. D **57** 885-907 (1998).

[2] T. Damour, B. R. Iyer, B. S. Sathyaprakash, Phys. Rev. D **62**, 084036 (2000).

[3] T. Damour, B. R. Iyer, B. S. Sathyaprakash, Phys. Rev. D **63** 044023 (2001) [Erratum-ibid. D **72** 029902 (2005)] and its update Phys. Rev. D **66** 027502 (2002). [Erratum-ibid. D **72** 029901 (2005)]

[4] L. S. Finn, Phys. Rev. D **46** 5236-5249 (1992).

[5] L. A. Wainstein, V. D. Zubakov, *Extraction of signals from noise*, (Prentice-Hall, Englewood Cliffs, NJ) (1962).

[6] F. Echeverria, Ph.D. thesis, California Institute of Technology (1993), addendum to Chapter 2.

[7] L. S. Finn, D. F. Chernoff, Phys. Rev. D **47** 2198-2219 (1993).

[8] C. Cutler, E. E. Flanagan, Phys. Rev. D **49** 2658-2697 (1994).

[9] L. Lindblom, B. J. Owen, D. A. Brown, Phys. Rev. D **78** 124020 (2008).

[10] M. Vallisneri, Phys. Rev. D **77** 042001 (2008).

[11] R. Prix [for the LIGO Scientific Collaboration], in *Neutron Stars and Pulsars*, edited by W. Becker (Springer-Verlag Berlin, Heidelberg, Germany) (2009), p. 651.

[12] T. B. Littenberg, N. J. Cornish, Phys. Rev. D **80** 063007 (2009).

[13] T. B. Littenberg, N. J. Cornish, "Separating Gravitational Wave Signals from Instrument Artifacts," [arXiv:1008.1577].

[14] R. Balasubramanian, B. S. Sathyaprakash, S. V. Dhurandhar, Phys. Rev. D **53** 3033-3055 (1996).

[15] B. J. Owen, Phys. Rev. D **53** 6749-6761 (1996).

[16] B. J. Owen, B. S. Sathyaprakash, Phys. Rev. D **60** 022002 (1999).

[17] P. R. Brady *et al.*, Phys. Rev. D **57** 2101-2116 (1998).

[18] S. Babak, Class. Quant. Grav. **25** 195011 (2008).

[19] I. W. Harry, S. Fairhurst, B. S. Sathyaprakash, Class. Quant. Grav. **25** 184027 (2008).

[20] I. W. Harry, B. Allen, B. S. Sathyaprakash, Phys. Rev. D **80** 104014 (2009).

[21] C. Messenger, R. Prix, M. A. Papa, Phys. Rev. D **79** 104017 (2009).

[22] A. R. Liddle *et al.*, "Comment on 'Tainted evidence: cosmological model selection versus fitting', by Eric V. Linder and Ramon Miquel (astro-ph/0702542v2) ", [astro-ph/0703285].

[23] A. E. Raftery, *Practical Markov Chain Monte Carlo*, (Chapman and Hall, London) (1996).

[24] D. Gamerman, *Markov Chain Monte Carlo: Stochastic Simulation of Bayesian Inference*, (Chapman and Hall, London) (1997).

[25] A. Gelman, G. O. Roberts, W. R. Gilks, *Efficient Metropolis Jumping Rules* in: Bayesian Statistics 5, pp. 599-607 (Clarendon Press, Oxford, England) (1996)

[26] E. T. Jaynes, G. L. Bretthorst, *Probability Theory: The Logic of Science*, (Cambridge University Press, Cambridge, England) (2003).

[27] LISA Science Performance Evaluation (by Parameter Estimation), wikipage http://www.tapir.caltech.edu/dokuwiki/lisape:home.

[28] A. Buonanno, Y. Chen, M. Vallisneri, Phys. Rev. D **67** 104025 (2003).

[29] A. Gopakumar, "New class of gravitational wave templates for inspiralling compact binaries," [arXiv:0712.3236].

[30] A. Gopakumar *et al.*, Phys. Rev. D **78** 064026 (2008).

[31] M. Tessmer, A. Gopakumar, "On the ability of various circular inspiral templates to that incorporate radiation reaction effects at the second post-Newtonian order to capture inspiral gravitational waves from compact binaries having tiny orbital eccentricities," [arXiv:0812.0549].

[32] L. Blanchet *et al.*, Phys. Rev. Lett. **74** 3515 (1995).

[33] L. Blanchet, T. Damour, B. R. Iyer, Phys. Rev. D **51** 5360 (1995) [Erratum-ibid. D **54** 1860 (1996)] [Phys. Rev. D **54** 1860 (1996)].

[34] C. M. Will, A. G. Wiseman, Phys. Rev. D **54** 4813 (1996).

[35] L. Blanchet, Phys. Rev. D **54** 1417 (1996) [Erratum-ibid. D **71** 129904 (2005)].

[36] L. Blanchet *et al.*, Class. Quant. Grav. **13** 575 (1996).

[37] L. Blanchet, Class. Quant. Grav. **15** 113 (1998) [Erratum-ibid. **22** 3381 (2005)].

[38] L. Blanchet *et al.*, Phys. Rev. D **65** 061501 (2002) [Erratum-ibid. D **71** 129902 (2005)].

[39] L. Blanchet, B. R. Iyer, B. Joguet, Phys. Rev. D **65** 064005 (2002) [Erratum-ibid. D **71** 129903 (2005)].

[40] L. E. Kidder, Phys. Rev. D **77** 044016 (2008).

[41] L. E. Kidder, C. M. Will, A. G. Wiseman, Phys. Rev. D **47** 3281 (1993).

[42] T. A. Apostolatos *et al.*, Phys. Rev. D **49** 6274 (1994).

[43] L. Blanchet, A. Buonanno, G. Faye, Phys. Rev. D **74** 104034 (2006) [Erratum-ibid. D **75** 049903 (2007)] [Erratum-ibid. D **81** 089901 (2010)].

[44] L. E. Kidder, Phys. Rev. D **52** 821 (1995).

[45] E. Poisson, Phys. Rev. D **57** 5287 (1998).

[46] T. Damour, Phys. Rev. D **64** 124013 (2001).

[47] E. Berti *et al.*, Class. Quant. Grav. **25** 114035 (2008).

[48] K. G. Arun *et al.*, Phys. Rev. D **79** 104023 (2009).

[49] K. G. Arun *et al.*, Phys. Rev. D **71** 084008 (2005) [Erratum-ibid. D **72** 069903 (2005)].

[50] J. G. Baker *et al.*, Phys. Rev. Lett. **96** 111102 (2006).

[51] F. Pretorius, Phys. Rev. Lett. **95** 121101 (2005).

[52] M. Campanelli *et al.*, Phys. Rev. Lett. **96** 111101 (2006).

[53] B. Imbiriba *et al.*, Phys. Rev. D **70**, 124025 (2004).

[54] B. Vaishnav *et al.*, "Matched Filtering of Numerical Relativity Templates of Spinning Binary Phys. Rev. D **76**, 084020 (2007).

[55] U. Sperhake, Phys. Rev. D **76**, 104015 (2007).

[56] B. Bruegmann *et al.*, Phys. Rev. D **77**, 024027 (2008).

[57] M. A. Scheel *et al.*, Phys. Rev. D **74**, 104006 (2006).

[58] D. Pollney *et al.*, Phys. Rev. D **76**, 124002 (2007).

[59] J. A. Faber *et al.*, Phys. Rev. D **76**, 104021 (2007).

[60] T. Yamamoto, M. Shibata, K. Taniguchi, Phys. Rev. D **78**, 064054 (2008).

[61] Z. J. Cao, H. J. Yo, J. P. Yu, Phys. Rev. D **78**, 124011 (2008).

[62] S. L. Liebling, Phys. Rev. D **66**, 041703 (2002).

[63] T. Nakamura, K. Oohara, Y. Kojima, "General Relativistic Collapse To Black Holes And Gravitational Waves From Prog. Theor. Phys. Suppl. **90**, 1 (1987).

[64] M. Shibata, T. Nakamura, "Evolution of three-dimensional gravitational waves: Harmonic slicing Phys. Rev. D **52**, 5428 (1995).

[65] T. W. Baumgarte, S. L. Shapiro, Phys. Rev. D **59**, 024007 (1999).

[66] F. Pretorius, Class. Quant. Grav. **22**, 425 (2005).

[67] L. Lindblom *et al.*, Class. Quant. Grav. **23**, S447 (2006).

[68] M. Hannam, Class. Quant. Grav. **26** 114001 (2009).

[69] "Numerical INJection Analysis project", `http://www.ninja-project.org`.

[70] I. Hinder, Class. Quant. Grav. **27** 114004 (2010).

[71] M. Hannam *et al.*, Phys. Rev. D **79** 084025 (2009).

[72] B. Aylott *et al.*, Class. Quant. Grav. **26** 114008 (2009).

[73] B. Aylott *et al.*, Class. Quant. Grav. **26** 165008 (2009).

[74] M. Boyle *et al.*, Phys. Rev. D **76**, 124038 (2007).

[75] M. A. Scheel *et al.*, Phys. Rev. D **79**, 024003 (2009).

[76] A. Buonanno, T. Damour, Phys. Rev. D **59** 084006 (1999).

[77] A. Buonanno, T. Damour, Phys. Rev. D **62** 064015 (2000).

[78] T. Damour, P. Jaranowski, G. Schaefer, Phys. Rev. D **62** 084011 (2000).

[79] T. Damour, A. Nagar, Phys. Rev. D **79**, 081503 (2009).

[80] T. Damour *et al.*, Phys. Rev. D **78**, 044039 (2008).

[81] T. Damour, P. Jaranowski, G. Schaefer, Phys. Rev. D **78** 024009 (2008).

[82] A. Buonanno *et al.*, Phys. Rev. D **76**, 104049 (2007).

[83] T. Damour, A. Nagar, Phys. Rev. D **77**, 024043 (2008).

[84] T. Damour *et al.*, Phys. Rev. D **77**, 084017 (2008).

[85] A. Buonanno *et al.*, Phys. Rev. D **79**, 124028 (2009).

[86] Y. Pan *et al.*, Phys. Rev. D **81** 084041 (2010).

[87] T. Damour, B. R. Iyer, A. Nagar, Phys. Rev. D **79** 064004 (2009).

[88] P. Ajith *et al.*, Phys. Rev. D **77** 104017 (2008). [Erratum-ibid. D **79** 129901 (2009)].

[89] P. Ajith *et al.*, "'Complete' gravitational waveforms for black-hole binaries with non-precessing spins," [arXiv:0909.2867].

[90] L. Santamaria *et al.*, Phys. Rev. D **82** 064016 (2010).

[91] W. H. Press *et al.*, *Numerical Recipes 3rd Edition: The Art of Scientific Computing* (Cambridge University Press, Cambridge, England) (2007).

[92] S. Droz *et al.*, Phys. Rev. D **59**, 124016 (1999).

[93] K. S. Thorne, in *300 Years of Gravitation*, edited by S. W. Hawking and W. Israel (Cambridge University Press, Cambridge, England) (1987), p. 330.

[94] I. Mandel, R. O'Shaughnessy, Class. Quant. Grav. **27** 114007 (2010).

[95] J. Abadie *et al.* [LIGO Scientific and Virgo Collaborations], Class. Quant. Grav. **27** 173001 (2010).

[96] K. G. Arun *et al.*, Class. Quant. Grav. **26** 094027 (2009).

[97] J. Kormendy, D. Richstone, Ann. Rev. Astron. Astrophys. **33** 581 (1995).

[98] J. Magorrian *et al.*, Astron. J. **115** 2285 (1998).

[99] R. Narayan, New J. Phys. **7** 199 (2005).

[100] A. M. Ghez *et al.*, Astrophys. J. **689** 1044-1062 (2008).

[101] A. Sesana, M. Volonteri, F. Haardt, Mon. Not. Roy. Astron. Soc. **377** 1711-1716 (2007).

[102] S. Babak *et al.* [MLDC Task Force Collaboration], Class. Quant. Grav. **25** 184026 (2008).

[103] S. Babak *et al.* [MLDC Task Force Collaboration], Class. Quant. Grav. **27** 084009 (2010).

Part II

Original scientific results

Impact of higher harmonics on parameter estimation of SMBHs inspiral signals

The following published articles were included in this chapter of the thesis:

- **M. Trias** and A.M. Sintes, *LISA observations of supermassive black holes: parameter estimation using full PN inspiral waveforms*, Physical Review D **77**, 024030 (2008) [19 pages]

- **M. Trias** and A.M. Sintes, *LISA parameter estimation of supermassive black holes*, Classical and Quantum Gravity **25**, 184032 (2008) [9 pages]

- K.G. Arun et al. (including **M. Trias**), *Massive Black Hole Binary Inspirals: Results from the LISA Parameter Estimation Taskforce*, Classical and Quantum Gravity **26**, 094027 (2009) [14 pages]

Chapter 5

Measuring the dark energy equation of state with LISA

The following published article was included in this chapter of the thesis:

- C. Van Den Broeck, **M. Trias**, B.S. Sathyaprakash and A.M. Sintes, *Weak lensing effects in the measurement of the dark energy EOS with LISA*, Physical Review D **81**, 124031 (2010) [15 pages]

Chapter 6

Searching for galactic binary systems with LISA using MCMC

The following published articles were included in this chapter of the thesis:

- **M. Trias**, A. Vecchio and J. Veitch, *MCMC searches for galactic binaries in MLDC 1B data sets*, Classical and Quantum Gravity **25**, 184028 (2008) [10 pages]

- **M. Trias**, A. Vecchio and J. Veitch, *Studying stellar binary systems with LISA using DR-MCMC methods*, Classical and Quantum Gravity **26**, 204024 (2009) [11 pages]

Chapter 7

Delayed Rejection Markov chain Monte Carlo

The following article was included in this chapter of the thesis:

- **M. Trias**, A. Vecchio and J. Veitch, *DR schemes for efficient MCMC sampling of multimodal distributions*, `arXiv: 0904.2207` [31 pages]

Addendum to Chapter 7. Toy examples to illustrate and quantify the efficiency of DR MCMC chains

The benefit of DR is that it increases the efficiency of sampling by delaying a possible a rejection, at the same time that it allows us to propose a new candidate that can be drawn using the information of the past stages. Indeed, Mira *et al.* [1, 2] demonstrate from a formal point of view that DR increases the transition probability of the states of the chain within the different parts of the parameter space, improving the mixing of the chain and leading to a reduction [3] of the asymptotic variance of any estimator, say $\bar{\lambda}$.

The purpose of this addendum is to 'illustrate' this efficiency increase in some toy examples, by estimating and comparing the variance of chains generated with and without DR. We are fully aware that all the results that we shall obtain in this addendum are *merely tests of validity*, applied to simple examples, *of the general result formally demonstrated by Mira et al. [1, 2]* and therefore the conclusions we shall obtain here, are not new. However, we think that it may be useful to observe the benefits of DR in some actual examples, at the same time that we obtain a *quantitative measurement* of this efficiency increase in terms of the variances of the resulting chains.

Intuitively, it may be difficult to see that DR actually increases the efficiency of the chain *at a given computational cost*[1] because, on the one hand, it reduces the number of repeated elements of a chain by delaying a possible rejection; but on the other hand, the number of elements of the resulting chain (for a fixed computational cost, *i.e.* number of new proposed states[2]) will be smaller. Since the variance of the chain involves the ratio between the correlation function and the number of elements of the chain [see Eq. (7.8) below], it is not clear which of the two effects shall dominate, or whether this can depend on the particular problem at hand. Thus, the question that we want to answer in this addendum is: *"Is there a benefit (in terms of reducing the variance of the estimate) from removing some repeated elements of a chain?"*.

Preliminary considerations

Suppose we wish to estimate the expectation

$$I \equiv \langle f \rangle_\pi = \sum_{i=0}^{s} f(i)\pi_i \ , \tag{7.1}$$

where $\boldsymbol{\pi} = (\pi_0, \pi_1, \ldots, \pi_s)$ is a positive probability distribution, *i.e.* $\pi_i > 0$ for all i, and $f(\cdot)$ is a non-constant function defined on the states $\{0, 1, \ldots, s\}$ of an irreducible Markov chain determined by the transition matrix $\mathbf{P} = \{p_{ij}\}$. If $\mathbf{P}$ is chosen so that $\boldsymbol{\pi}$ is its unique stationary distribution, then after simulating the Markov chain for times $t = 1, \ldots, N$, an estimate of the expectation I is given by

$$\bar{I} = \sum_{t=1}^{N} f\{\boldsymbol{\lambda}(t)\}/N \ , \tag{7.2}$$

---

[1]We assume that evaluating the likelihood function is the most demanding calculation in terms of computational time, and therefore we shall estimate 'computational costs' directly as the *number of likelihood evaluations*.

[2]Each new proposed state requires a likelihood evaluation.

where $\boldsymbol{\lambda}(t)$ denotes the state occupied by the chain at time t.

The performance in the MCMC sampling can be measured through two quantities: *(i)* the *bias* of the estimate $\bar{I}$, defined as $\lim_{N\to\infty}\left[E(\bar{I})-I\right]$, represents the accuracy of the sampling; and *(ii)* the *variance* of the estimate, which represents its precision. As Peskun [3] points out, since $\mathrm{var}(\bar{I})$ is $\mathcal{O}(N^{-1})$ and the bias squared is $\mathcal{O}(N^{-2})$, for an appropriate distribution of the initial state $\boldsymbol{\lambda}(0)$, the bias has a negligible effect (at least, it decreases faster) on the accuracy of the estimate $\bar{I}$. Moreover, we can highly reduce the bias by neglecting the points from the 'burn-in' period. We shall thus confine our discussions to the precision (variance), rather than the accuracy (bias), of the estimate $\bar{I}$.

In particular, the variance of the estimate $\bar{I}$ can be computed in terms of the autocorrelation function of the Markov chain [4–6] as

$$\mathrm{var}(\bar{I}) = \frac{1}{N^2}\sum_{r,s=1}^{N} C_{ff}(r-s)\ , \tag{7.3}$$

where $C_{ff}(t)$ is the *(unnormalized) autocorrelation function* of the function $f\{\boldsymbol{\lambda}\}$ at lag t, defined as

$$C_{ff}(t) \equiv \langle f_s f_{s+t}\rangle - \bar{I}^2 = \langle f\{\boldsymbol{\lambda}(s)\}f\{\boldsymbol{\lambda}(s+t)\}\rangle - \bar{I}^2\ . \tag{7.4}$$

The *normalized autocorrelation function* is then

$$\rho_{ff}(t) \equiv C_{ff}(t)/C_{ff}(0)\ . \tag{7.5}$$

Typically, $\rho_{ff}(t)$ decays exponentially for large t; this defines the *exponential autocorrelation time*, τ_{exp}, [4]

$$\rho_{ff}(t) \sim e^{-|t|/\tau_{exp}}\ . \tag{7.6}$$

When the number of elements of the Markov chain, N, is large enough; the variance of the estimate $\bar{I}$ given by equation (7.3) can be rewritten in terms of the *integrated autocorrelation time* [4],

$$\tau_{int} \equiv \frac{1}{2}\sum_{n=-N}^{N} \rho_{ff}(n) = \frac{1}{2} + \sum_{n=1}^{N}\rho_{ff}(n)\ , \tag{7.7}$$

as

$$\mathrm{var}(\bar{I}) \simeq \frac{2\,\tau_{int}\,C_{ff}(0)}{N}\ . \tag{7.8}$$

The factor of $\frac{1}{2}$ in the definition of the integrated autocorrelation time (7.7) is purely a matter of convention; it is inserted so that $\tau_{int}\approx\tau_{exp}$ for $\tau\gg 1$.

In what follows, we shall consider several toy examples in which we shall assume to have a hypothetical Markov chain with a certain number of repeated elements (namely, *chain A*) that could be removed by using DR, resulting into a shorter, but less correlated, chain (let us call it *chain B*). Given the simplicity (and periodicity) of the Markov chains considered in these toy examples, we shall be able to compute, in a theoretical way and using Eqs. (7.7) and (7.8), the variance of an arbitrary estimate $\bar{I}$ from the chain B, $\mathrm{var}_B(\bar{I})$, in terms of the variance of the same estimate from the chain A, $\mathrm{var}_A(\bar{I})$. Despite being just toy examples, we aim to provide a quantitative illustration of the benefits of using DR.

Chain A (duplicated elements): ①①②②③③④④⑤⑤⑥⑥⑦⑦⑧⑧⑨⑨⑩⑩ ⋯

Chain B: ① ② ③ ④ ⑤ ⑥ ⑦ ⑧ ⑨ ⑩ ⋯

Figure 7.1: Case I. Example of two Markov chains, one of them with all its elements duplicated.

Case I: Duplicate all elements of a chain

We shall start considering a very simple scenario, which consists in assuming that only one every second proposed state is accepted, resulting into a Markov chain with all its elements duplicated, as every time one proposal is rejected the chain remains at the original state. In this case, a two-stages DR algorithm could be used in order to remove all the repeated elements of the chain. Fig. 7.1 provides an schematic representation of the two chains, using repeated circled numbers to denote repeated elements of the chain.

Without loss of generality, we shall assume a zero-mean estimator, *i.e.* $\bar{I} = 0$, so that the autocorrelation function at lag t, Eq. (7.4), is simply $C_{ff}(t) = \langle f_s f_{s+t} \rangle = \frac{1}{N-t} \sum_{s=1}^{N-t} f_s f_{s+t}$.

From Fig. 7.1, and assuming that the chains only have the finite number of elements explicitly shown in the figure, we can explicitly compute the autocorrelation function of the two different chains and look for a relation between the different values.

$$C_B(0) = \frac{1}{10} \left(①^2 + ②^2 + ③^2 + ④^2 + \cdots + ⑩^2 \right) \tag{7.9}$$

$$C_A(0) = \frac{1}{20} \left(2①^2 + 2②^2 + 2③^2 + 2④^2 + \cdots + 2⑩^2 \right) = C_B(0)$$

$$C_B(1) = \frac{1}{9} \left(①② + ②③ + ③④ + ④⑤ + \cdots + ⑨⑩ \right) \tag{7.10}$$

$$C_A(1) = \frac{1}{19} \left(①^2 + ①② + ②^2 + ②③ + \cdots + ⑨⑩ + ⑩^2 \right) = \frac{1}{19} \left[10\,C_B(0) + 9\,C_B(1) \right]$$

$$C_B(2) = \frac{1}{8} \left(①③ + ②④ + ③⑤ + ④⑥ + \cdots + ⑧⑩ \right) \tag{7.11}$$

$$C_A(2) = \frac{1}{18} \left(①② + ①② + ②③ + ②③ + \cdots + ⑨⑩ + ⑨⑩ \right) = C_B(1)$$

$$C_B(3) = \frac{1}{7} \left(①④ + ②⑤ + ③⑥ + ④⑦ + \cdots + ⑦⑩ \right) \tag{7.12}$$

$$C_A(3) = \frac{1}{17} \left(①② + ①③ + ②③ + ②④ + \cdots + ⑧⑩ + ⑨⑩ \right) = \frac{1}{17} \left[9\,C_B(1) + 8\,C_B(2) \right]$$

$$C_B(4) = \frac{1}{6} \left(①⑤ + ②⑥ + ③⑦ + ④⑧ + \cdots + ⑥⑩ \right) \tag{7.13}$$

$$C_A(4) = \frac{1}{16} \left(①③ + ①③ + ②④ + ②④ + \cdots + ⑧⑩ + ⑧⑩ \right) = C_B(2)$$

$$C_B(5) = \frac{1}{5} \left(①⑥ + ②⑦ + ③⑧ + ④⑨ + ⑤⑩ \right) \tag{7.14}$$

$$C_A(5) = \frac{1}{15} \left(①③ + ①④ + ②④ + ②⑤ + \cdots + ⑦⑩ + ⑧⑩ \right) = \frac{1}{15} \left[8\,C_B(2) + 7\,C_B(3) \right]$$

$\cdots$

Chain A (duplicated elements):   ① ②② ③ ④④ ⑤ ⑥⑥ ⑦ ⑧⑧ ⑨ ⑩⑩ ⋯

Chain B: ① ② ③ ④ ⑤ ⑥ ⑦ ⑧ ⑨ ⑩ ⋯

Figure 7.2: Case II. Example of two Markov chains, one of them with its even elements duplicated.

From these explicit expressions, one can infer the general relation between $C_A(n)$ and $C_B(n)$ for all n:

$$
\begin{aligned}
C_A(0) &= C_B(0)\,, \\
C_A(2n) &= C_B(n)\,, \\
C_A(2n+1) &= \frac{1}{2N-2n-1}\left[(N-n)\,C_B(n) + (N-n-1)\,C_B(n+1)\right].
\end{aligned}
\tag{7.15}
$$

Finally, we use Eq. (7.7) to compute the integrated autocorrelation time, that is directly related to the variance of the estimate.

$$
\begin{aligned}
\tau_{int,\,B} &= \frac{1}{2} + \frac{1}{C_B(0)}\sum_{n=1}^{N} C_B(n)\,; \tag{7.16}\\[2mm]
\tau_{int,\,A} &= \frac{1}{2} + \frac{1}{C_A(0)}\sum_{n=1}^{2N} C_A(n) \\[2mm]
&= \frac{1}{2} + \frac{1}{C_B(0)}\left(\sum_{n=1}^{N} C_A(2n) + \sum_{n=0}^{N-1} C_A(2n+1)\right)\\[2mm]
&= \frac{1}{2} + \frac{1}{C_B(0)}\left(\sum_{n=1}^{N} C_B(n) + \sum_{n=0}^{N-1}\frac{N-n}{2N-2n-1}C_B(n) + \sum_{n=0}^{N-1}\frac{N-n-1}{2N-2n-1}C_B(n+1)\right)\\[2mm]
&\approx \frac{1}{2} + \frac{1}{C_B(0)}\left(\sum_{n=1}^{N} C_B(n) + \frac{1}{2}\sum_{n=0}^{N-1} C_B(n) + \frac{1}{2}\sum_{n=0}^{N-1} C_B(n+1)\right)\\[2mm]
&\approx \frac{1}{2} + \frac{1}{C_B(0)}\left(\sum_{n=1}^{N} C_B(n) + \sum_{n=1}^{N} C_B(n) + \frac{1}{2}C_B(0)\right)\\[2mm]
&= 2\,\tau_{int,\,B}\,; \tag{7.17}
\end{aligned}
$$

where we only have assumed $N\to\infty$, and that $C_B(n)\to 0$ as $n\to N$.

Thus, in this case we obtain that by duplicating N; τ also doubles, keeping the variance (7.8) constant: $\mathrm{var}_A(\bar{I}) = \mathrm{var}_B(\bar{I})$. Hence, in this extremely simple example the use of DR does not really increase the efficiency of the Markov chain since the effect of reducing its correlations is compensated by the decrease on the number of elements of the chain (for the same computational cost). We shall see in the following examples, that this is *not* the general case and that normally, the use DR does increase the efficiency of the resulting chains.

Case II: Duplicate one element every second

In this case, we go one step further and consider a chain that only its even elements are duplicated (see Fig. 7.2). This case could exemplify a canonical situation where a proposal is accepted twice every three iterations. With this, the explicit autocorrelation functions

take the form,

$$C_B(0) \;=\; \frac{1}{10}\left(①^2 + ②^2 + ③^2 + ④^2 + \cdots + ⑩^2\right) \tag{7.18}$$

$$C_A(0) \;=\; \frac{1}{15}\left(①^2 + ②^2 + ②^2 + ③^2 + ④^2 + ④^2 + \cdots + ⑨^2 + ⑩^2 + ⑩^2\right) \overset{\text{avg.}}{\approx} C_B(0)$$

$$C_B(1) \;=\; \frac{1}{9}\left(①\,② + ②\,③ + ③\,④ + ④\,⑤ + \cdots + ⑨\,⑩\right) \tag{7.19}$$

$$C_A(1) \;=\; \frac{1}{14}\left(①\,② + ②^2 + ②\,③ + ③\,④ + ④^2 + \cdots + ⑨\,⑩ + ⑩^2\right) \overset{\text{avg.}}{\approx} \frac{1}{14}\left[9\,C_B(1) + 5\,C_B(0)\right]$$

$$C_B(2) \;=\; \frac{1}{8}\left(①\,③ + ②\,④ + ③\,⑤ + ④\,⑥ + \cdots + ⑧\,⑩\right) \tag{7.20}$$

$$C_A(2) \;=\; \frac{1}{13}\left(①\,② + ②\,③ + ②\,④ + ③\,④ + ④\,⑤ + ④\,⑥ + \cdots\right) \overset{\text{avg.}}{\approx} \frac{1}{13}\left[9\,C_B(1) + 4\,C_B(2)\right]$$

$$C_B(3) \;=\; \frac{1}{7}\left(①\,④ + ②\,⑤ + ③\,⑥ + ④\,⑦ + \cdots + ⑦\,⑩\right) \tag{7.21}$$

$$C_A(3) \;=\; \frac{1}{12}\left(①\,③ + ②\,④ + ②\,④ + ③\,⑤ + ④\,⑥ + ④\,⑥ + \cdots\right) \overset{\text{avg.}}{\approx} C_B(2)$$

$$C_B(4) \;=\; \frac{1}{6}\left(①\,⑤ + ②\,⑥ + ③\,⑦ + ④\,⑧ + \cdots + ⑥\,⑩\right) \tag{7.22}$$

$$C_A(4) \;=\; \frac{1}{11}\left(①\,④ + ②\,④ + ②\,⑤ + ③\,⑥ + \cdots + ⑦\,⑩ + ⑧\,⑩\right) \overset{\text{avg.}}{\approx} \frac{1}{11}\left[7\,C_B(3) + 4\,C_B(2)\right]$$

$$C_B(5) \;=\; \frac{1}{5}\left(①\,⑥ + ②\,⑦ + ③\,⑧ + ④\,⑨ + ⑤\,⑩\right) \tag{7.23}$$

$$C_A(5) \;=\; \frac{1}{10}\left(①\,④ + ②\,⑤ + ②\,⑥ + ③\,⑥ + \cdots\right) \overset{\text{avg.}}{\approx} \frac{1}{10}\left[7\,C_B(3) + 3\,C_B(4)\right]$$

$$C_B(6) \;=\; \frac{1}{4}\left(①\,⑦ + ②\,⑧ + ③\,⑨ + ④\,⑩\right) \tag{7.24}$$

$$C_A(6) \;=\; \frac{1}{9}\left(①\,⑤ + ②\,⑥ + ②\,⑥ + ③\,⑦ + \cdots + ⑥\,⑩\right) \overset{\text{avg.}}{\approx} C_B(4)$$

$$\cdots$$

Here, in order to obtain the relations after the $\overset{\text{avg.}}{\approx}$ symbol, we have used the fact that the Markov chain samples an stationary distribution.

From these explicit expressions, one can infer the general relations between $C_A(n)$ and $C_B(n)$ for all n:

$$
\begin{aligned}
C_A(0) \;&=\; C_B(0)\,, \\
C_A(3n) \;&=\; C_B(2n)\,, \\
C_A(3n+1) \;&=\; \frac{1}{\frac{3}{2}N - 3n - 1}\left[(N - 2n - 1)\,C_B(2n+1) + \left(\tfrac{N}{2} - n\right)C_B(2n)\right], \\
C_A(3n+2) \;&=\; \frac{1}{\frac{3}{2}N - 3n - 2}\left[(N - 2n - 1)\,C_B(2n+1) + \left(\tfrac{N}{2} - n - 1\right)C_B(2n+2)\right].
\end{aligned}
\tag{7.25}
$$

Then, the general expressions for the integrated autocorrelation times will be given by

$$
\tau_{int,B} \;=\; \frac{1}{2} + \frac{1}{C_B(0)}\sum_{n=1}^{N} C_B(n) \tag{7.26}
$$

$$
\tau_{int,A} \;=\; \frac{1}{2} + \frac{1}{C_A(0)}\sum_{n=1}^{3N/2} C_A(n)
$$

$$
=\; \frac{1}{2} + \frac{1}{C_B(0)}\left(\sum_{n=1}^{N/2} C_A(3n) + \sum_{n=0}^{\frac{N}{2}-1} C_A(3n+1) + \sum_{n=0}^{\frac{N}{2}-1} C_A(3n+2)\right)
$$

$$
=\; \frac{1}{2} + \frac{1}{C_B(0)}\left(\sum_{n=1}^{N/2} C_B(2n) + \sum_{n=0}^{\frac{N}{2}-1}\left[\frac{N-2n-1}{\frac{3}{2}N-3n-1}C_B(2n+1) + \frac{\frac{N}{2}-n}{\frac{3}{2}N-3n-1}C_B(2n)\right.\right.
$$

$$
\left.\left. + \frac{N-2n-1}{\frac{3}{2}N-3n-2}C_B(2n+1) + \frac{\frac{N}{2}-2n-1}{\frac{3}{2}N-3n-2}C_B(2n+2)\right]\right)
$$

$$
\approx\; \frac{1}{2} + \frac{1}{C_B(0)}\left(\sum_{n=1}^{N/2} C_B(2n) + \frac{1}{3}\sum_{n=0}^{\frac{N}{2}-1}\left[2\,C_B(2n+1) + C_B(2n) + 2\,C_B(2n+1) + C_B(2n+2)\right]\right)
$$

$$
=\; \frac{1}{2} + \frac{1}{C_B(0)}\left(\sum_{n=1}^{N/2} C_B(2n) + \frac{4}{3}\sum_{n=0}^{\frac{N}{2}-1} C_B(2n+1) + \frac{1}{3}C_B(0) + \frac{2}{3}\sum_{n=0}^{\frac{N}{2}-1} C_B(2n+2)\right)
$$

$$
=\; \frac{1}{2} + \frac{1}{C_B(0)}\left(\frac{4}{3}\sum_{n=1}^{N} C_B(n) + \frac{1}{3}\left[C_B(0) + \sum_{n=1}^{N/2} C_B(2n)\right]\right)
$$

$$
=\; \frac{4}{3}\tau_{int,B} + \frac{1}{3}\left(\frac{1}{2} + \sum_{n=1}^{N/2}\frac{C_B(2n)}{C_B(0)}\right) \tag{7.27}
$$

Making use of the definition of the exponential autocorrelation time in Equation (7.6), we can rewrite $\tau_{int,B}$ and the sum that appears in the final result of (7.27), in a more convenient way [here we shall define $\tau_{exp,B} \equiv \tau$ and assume $N \gg \tau$]:

$$
\tau_{int,B} \;=\; \frac{1}{2} + \sum_{n=1}^{N}\frac{C_B(n)}{C_B(0)} = \frac{1}{2} + \sum_{n=1}^{N} e^{-n/\tau} = \frac{1}{2} + \frac{1}{e^{1/\tau}-1} = \frac{1}{2}\coth\left[\frac{1}{2\tau}\right]\,, \quad (7.28)
$$

$$
(\cdot)\text{ in }(7.27) \;=\; \frac{1}{2} + \sum_{n=1}^{N/2}\frac{C_B(2n)}{C_B(0)} = \frac{1}{2} + \sum_{n=1}^{N/2} e^{-2n/\tau} = \frac{1}{2} + \frac{1}{e^{2/\tau}-1} = \frac{1}{2}\coth\left[\frac{2}{2\tau}\right]\,. (7.29)
$$

Finally, we can put together all the results from Eqs. (7.26)-(7.29) into the definition of the variance of the estimate $\bar{I}$, Eq. (7.8), in order to obtain by how much the variance is

reduced because of removing the repeated elements of the chain [we recall that $N_A = \frac{3}{2}N_B$],

$$
\begin{aligned}
\frac{\text{var}_A(\bar{I}) - \text{var}_B(\bar{I})}{\text{var}_B(\bar{I})} \quad &= \quad \frac{\tau_{int,A} - \frac{N_A}{N_B}\,\tau_{int,B}}{\frac{N_A}{N_B}\,\tau_{int,B}} \\[2mm]
&= \quad \frac{\frac{4}{3}\,\tau_{int\,B} + \frac{1}{3}\left(\frac{1}{2} + \sum_{n=1}^{N/2}\frac{C_B(2n)}{C_B(0)}\right) - \frac{3}{2}\tau_{int\,B}}{\frac{3}{2}\,\tau_{int\,B}} \\[2mm]
&= \quad \frac{2}{9}\,\frac{\left(\frac{1}{2} + \sum_{n=1}^{N/2}\frac{C_B(2n)}{C_B(0)}\right)}{\tau_{int,B}} - \frac{1}{9} \\[2mm]
&= \quad \frac{1}{9}\left(2\,\text{coth}\left[\frac{2}{2\tau}\right]\,\text{tanh}\left[\frac{1}{2\tau}\right] - 1\right) \geq 0 \qquad (7.30)
\end{aligned}
$$

The main consequence of this result is that $\text{var}_B(\bar{I}) \leq \text{var}_A(\bar{I})$ or, in other words, we have just showed that DR always increases the efficiency of the resulting Markov chain in terms of reducing the variance of any estimate. Moreover, the previous result allows us to obtain quantitative measures of such improvement; in particular, we would obtain a 2.4% reduction if $\tau = 1$; 0.7% when $\tau = 2$; 0.3% when $\tau = 3$; ... These are indeed moderate improvements, but as we shall see below in Fig. 7.4, DR performance becomes important when the needed number of stages within a DR sub-chain is much greater than the autocorrelation time of the (main) chain.

## Case III: Repeat M_2 times one element every M_1-th

Finally, let us consider a generalization of the two previous examples, where we shall assume a chain consisting in a set of M_2 repeated elements every M_1-th, M_1 and M_2 being integers. We see this toy model as a basic representation of a situation in which a Markov chain is generated from two different proposals, P_1 and P_2, and one of them, say P_2, has a much lower acceptance probability (see Fig. 7.3). Then, as far as one is proposing from P_1, a chain is being built with a given autocorrelation time τ; and once every M_1 of these proposals, one attempts P_2 until it is accepted, which we assume that it is M_2 times. The resulting chain (A) will contain M_2 completely correlated (repeated) elements every $M_1 + M_2$ iterations, whose efficiency could be improved by grouping all these M_2 elements into a single one, using the DR algorithm (chain B in Fig. 7.3).

This particular example tries to emulate, in a sense, the situation described in the article previously included in the current chapter; where P_1 would be the unimodal Gaussian proposals that explore the neighborhood of the original position, and P_2 would represent the trimodal distributions attempting big jumps in the parameter space. When the likelihood function is characterized by several isolated maxima, the acceptance probability of P_1 will be much higher than P_2. Another situation that could be well exemplified by the current toy model is a case where we would use delayed rejection (DR) in combination with RJMCMC in order to delay the possible rejection of transdimensional transitions; in this case, P_1 would be the proposals exploring the parameter space within the same model, and P_2 would represent the transdimensional proposals.

Following a similar approach than in the previous cases, we can compute the general expressions that relate the autocorrelation functions of the two chains schematized in
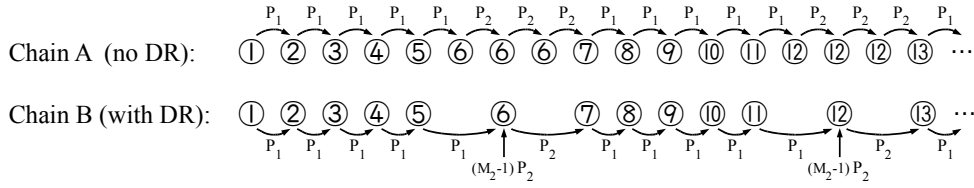
Figure 7.3: Case III. Example of the Markov chains that would be generated in the theoretical case in which every M_1 elements drawn from a certain proposal, P_1, M_2 transitions from a second proposal, P_2, are attempted but accepted with lower probability. The Delayed Rejection algorithm attempts the same number (M_2) of transitions drawn from P_2 as the standard MCMC, but it only stores the one that is accepted. Different circled numbers represent possible different elements of the chain, whereas the repeated ones explicitly denote the rejected transitions drawn from P_2. In this example we are considering $M_1 = 5$ and $M_2 = 3$.

(a) $(\Delta_{\mathrm{var}}/\mathrm{var}) \times 100$ (b) M_1 that maximizes $(\Delta_{\mathrm{var}}/\mathrm{var})$
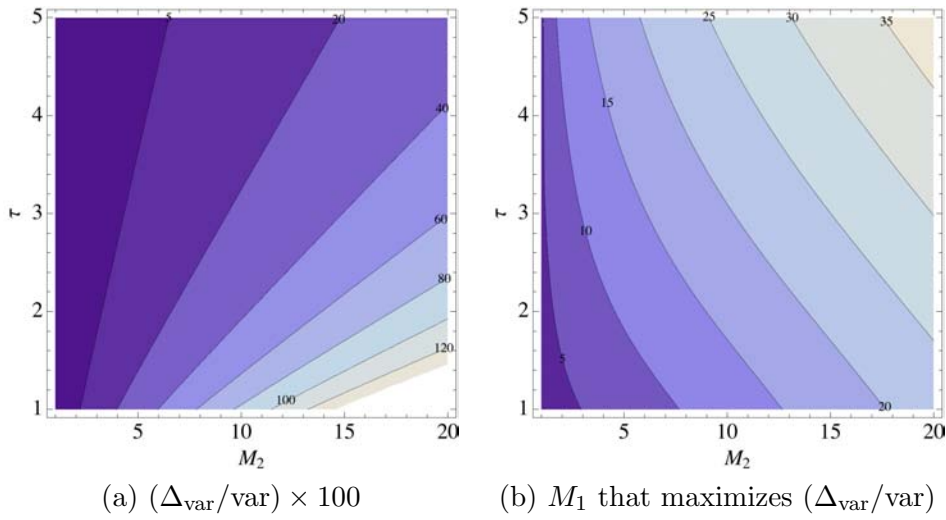
Figure 7.4: Maximization of Eq. (7.31) over M_1 assuming different values for M_2 and τ. For a given $\{M_2, \tau\}$ values, contour plot '(a)' shows the (maximized) percentage reduction of the variance when the repeated elements of the chain are removed (*i.e.* when DR is used); whereas '(b)' plots the M_1 values that maximized this variance reduction.

Fig. 7.3, A and B; then we use Eq. (7.7) to compute the integrated autocorrelation time for each of the chains; and, finally, one makes use of Eq. (7.8) to compare the two variances. The final result that it is obtained after adopting similar approximations as the ones described in the previous cases is:

$$\frac{\mathrm{var}_A(\bar{I}) - \mathrm{var}_B(\bar{I})}{\mathrm{var}_B(\bar{I})} = \left(\frac{M_2 - 1}{M_1 + M_2}\right)^2 \left[(M_1 + 1)\coth\left(\tfrac{M_1+1}{2\tau}\right)\tanh\left(\tfrac{1}{2\tau}\right) - 1\right] \geq 0 \,, \quad (7.31)$$

where we have used the definition of the exponential autocorrelation time, $\tau_{exp,B} \equiv \tau$, given in (7.6). In Fig. 7.4 we shall denote the quantity defined here, in Eq. (7.31), as $(\Delta_{\mathrm{var}}/\mathrm{var})$.

Notice that, although 'a priori' and intuitively it could be difficult to see which of the effects related to the efficiency of the chain (*to reduce the autocorrelation by removing repeated elements*; or *to reduce the length of the chain for a fixed computational cost*; see discussion at the beginning of this addendum) would dominate; the result obtained in Equation (7.31) shows that, for a fixed computational time, *we always obtain a benefit from removing repeated elements of a chain in terms of reducing the variance of any estimate.*

It is clear that the current toy model we are considering here is just a canonical representation of the chains usually found in actual applications of DR, but at least it provides an approximated, and quantitative, result that supports the formal proofs provided by Mira *et al.* [1, 2]. Besides obtaining that $\mathrm{var}_B(\bar{I}) \leq \mathrm{var}_A(\bar{I})$, Eq. (7.31) also can be used to obtain some quantitative information as a function of $\{M_1, M_2, \tau\}$. In particular, we shall consider $\{M_2, \tau\}$ to be given by the problem at hand [M_2 as a typical value for the inverse of the acceptance probability of the P_2 proposal, and τ as the typical autocorrelation time of the elements generated from P_1], thus we are studying the variance reduction as a function of M_1 [we recall that this parameter represents how often a set of P_2 proposals is attempted]. It turns out that Eq. (7.31) always shows a single local maximum as a function of M_1 (keeping $\{M_2, \tau\}$ fixed); and, indeed, Fig. 7.4 plots the result of this maximization process [(a) the maximum values of the percentage variance reduction, and (b) the M_1 values that maximized ($\Delta_{\mathrm{var}}/\mathrm{var}$)] as a function of $\{M_2, \tau\}$. We observe that the most important variance reductions are obtained when M_2 is large and τ small, *i.e.* when the acceptance probability of P_2 is much smaller than P_1's. In these cases, we observe that the reductions can be $\gtrsim 100\%$.

References

[1] A. Mira, Metron **LIX** (3-4), 231-241 (2001).

[2] L. Tierney and A. Mira, Statistics in Medicine **18** (17-18), 2507-2515 (1999).

[3] P. H. Peskun, Biometrika **60** 607 (1973).

[4] A. D. Sokal, *Monte Carlo methods in statistical mechanics: foundations and new algorithms*, lectures given at the Cours de Troisième Cycle de la Physique en Suisse Romande, Lausanne, Switzerland (1989).

[5] W. Gilks, S. Richardson and D. Spiegelhalter, *Markov Chain Monte Carlo in practice*, (Chapman & Hall, London) (1995).

[6] A. Gelman *et al.* Bayesian Statistics **5** 599-607, (Clarendon Press, Oxford) (1996).

Chapter 8

Studying the accuracy and effectualness of closed-form waveform models

The following published article was included in this chapter of the thesis:

- T. Damour, A. Nagar and **M. Trias**, *Accuracy and effectualness of closed-form, f-dom waveforms for nonspinning BBHs*, Physical Review D **83**, 024006 (2011) [30 pages]

Chapter 9

Conclusions

The coalescence of *similar-mass compact binary objects* are among the most important sources of GW radiation expected to be observed with current and future interferometric detectors. The potential astronomical GW sources within *similar-mass CBCs*, cover a very wide range of observable masses (from $\sim M_\odot$ up to $\sim 10^7 M_\odot$) and distances (from the galactic vicinity up to cosmological distances), which is directly related to the great scientific impact that such observations will have on the knowledge about our Universe. In order to make all this possible, it is necessary to understand the dynamics that characterize such events and to develop data analysis techniques for the detection of signals from the noisy strain and the extraction of reliable physical information about the emitting source.

This PhD thesis is devoted to tackle several significant data analysis (DA) problems that need to be solved in the current 'pre-detection' era. In particular, we have worked on *detection, parameter estimation* and *template accuracy* studies following, basically, three different research lines that are summarized in Table 9.1. Despite always considering the same theoretical source [namely, the *coalescence of (similar-mass) compact binary objects*]; the astrophysical background of the sources, their stage of evolution (and therefore, the model waveform that can be used), the GW detector and the data analysis technique that have been considered are completely different in each of the cases, and cover a very extensive range of possibilities within GW data analysis.

SOURCE	DETECTOR	MODEL WVF.	DA TECHNIQUE	ORIGINAL CONTRIBUTION
SMBHs	LISA	PN	FIM	Ch. 4: Impact of HHs Ch. 5: Measuring DE EoS
gal.binaries	LISA	monochromatic	MCMC	Ch. 6: MLDC search Ch. 7: DR-MCMC algorithm
BBHs	LIGO/Virgo	EOB,PN,phen.	accuracy/ effectualness	Ch. 8: Model comparison

Table 9.1: Summary of the source, detector, model waveform and data analysis technique used in each of the chapters of this thesis.

The election of the particular projects that have been carried out during the PhD period, respond to a balance between *pedagogical reasons* and *scientific relevance*. On one hand, we have tried to acquire a wide knowledge in GW data analysis problems by exploring different sorts of data analysis techniques, using most of the model waveforms that currently exist for CBCs and alternating both, ground-based and space-based detectors. On the other hand, we have tried to produce relevant scientific results within the GW community.

In particular, in Chapter 1 we give a brief introduction to the GW data analysis field. Chapter 2 is devoted to derive the expression of the GW strain measured at the detector, $h(t)$, in terms of the original, raw output of a numerical simulation; this is, the (spherical harmonic components of the) Regge-Wheeler and Zerilli functions, $\Psi_{\ell m}^{(o)}$ and $\Psi_{\ell m}^{(e)}$. In the process, we are obtaining the explicit dependency of $h(t)$ with all the orientation angles involved [see Eqs. (2.52) and (2.55) for the end results].

Then, Chapter 3 introduces the basic nomenclature and main results used in GW data analysis, and studies the mass and distance ranges of potential GW sources within the similar mass CBCs, considering both ground- and space-based detectors. In particular, we describe a very useful way to graphically represent signal and noise amplitudes, and to intuitively visualize the expected SNR of the signals (see Figs. 3.4 and 3.5); and then we provide astrophysical arguments to justify the expected population of (similar-mass) CBC sources. In particular,

1. LISA is expected to observe the coalescence of SMBHs from any point in our Universe with SNRs of several hundreds; these observations will help to understand the history of galaxy mergers in our Universe and therefore the galaxy formation, but they also can provide very useful cosmological information;

2. LISA will observe thousands of galactic stellar-mass binaries in very early stages of their evolution, where their emitted GW radiation can be well defined as a simple monochromatic signal, only modulated (in phase and amplitude) by the anisotropic sensitivity of the detector and its motion around de Sun;

3. ground-based detectors are expected to observe the late-inspiral, merger and ring-down stages of CBCs with total masses within $M \in (1M_\odot, 500M_\odot)$, located in the Virgo supercluster. In this case, the expected SNRs are very low and therefore, accurate waveform representations will be required in order to extract the maximum SNR from the measured strain.

These first three chapters form Part I of the thesis, devoted to *introductory notions*. In Chapters 4-8 (Part II), we present all our *original scientific results*, whose conclusions are summarized in the following three sections [organized according to the three research lines carried out during the doctorate (see Tab. 9.1 for a summary)].

Parameter estimation of SMBHs inspiral signals

In the current (evaluation) stage of the LISA project, it is crucial to understand the science that shall be extracted from LISA observations, thus, this is why parameter estimation studies like the ones presented in Chapters 4 and 5 are so important.

We have started by studying the impact of including all the harmonics of the SMBH inspiral waveform on the parameter estimation, instead of only using the dominant ($\ell = 2, m = \pm 2$) as it was done before. On one hand, the contribution of these new terms to higher harmonics (HHs) of the orbital frequency increases LISA's mass range of detectability of SMBHs to more massive systems, which have their dominant mode ($2f_{\mathrm{orb}}$) below the low-frequency edge of the LISA noise PSD, but not the higher harmonics ($3f_{\mathrm{orb}}, 4f_{\mathrm{orb}}, 5f_{\mathrm{orb}}, \ldots$). On the other hand, and more importantly, these new terms contribute to increase the richness of the waveforms, breaking some degeneracies between the parameters and therefore, significantly improving the parameter estimation. The impact is found to be more important in massive systems, $M \gtrsim 5 \times 10^6 M_\odot$, obtaining improvements of several orders of magnitude in some parameters (like the reduced mass) and factors $\sim 10 - 50$ of improvement in the most relevant parameters (from the scientific point of view), such as the luminosity distance and the sky resolution.

Moreover, we have found these improvements to make significant differences in terms of the fraction of events that could be identified. If we recall the results in Tab. 2 of [1] (in Chapter 4), we obtain that just by the inclusion of the HHs, we go from 0.8% to 19.3% of SMBHs binary systems with $\Delta\Omega_{\mathrm{N}} < (1° \times 1°)$ for ($10^7 M_\odot + 10^7 M_\odot$) systems located at $z = 1$. The impact is also important when considering lower mass systems, *e.g.* from 10% to 35% for ($10^6 M_\odot + 10^5 M_\odot$) systems located at the same fiducial distance.

Once learnt about the importance of including HHs in the SMBH inspiral signal, we have studied the potential scientific results that could be achieved from LISA observations of SMBHs. We first consider different models for the massive BH merger trees [2, 3], covering several possible scenarios given the limited knowledge that there exists about the actual formation history of SMBHs: small/large seeds and efficient/chaotic accretion. Results are summarized in Tab. 5 of [4] (in Chapter 4), and our conclusions are that ~ 30 (20) SMBHs events should be detectable during one year of observation with LISA when considering any small (large) seed scenario, which represents a fraction of $\sim 50\%$ (100%) of the mergers which occur in the universe during T_{obs}. From these events, there will be about 20 sources with a modest distance measurement (to within 10%) and about 10 sources with a modest sky resolution (10 deg^2); even more interestingly, each year LISA may observe a few sources with excellent sky resolution (1 deg^2) and luminosity measurements (to within 1%).

In Chapter 5, we also study the possibility of using a single LISA observation of SMBH as a new tool for precision cosmography, and in particular, for measuring the dark energy (DE) equation of state, w. After establishing a criterion for localizability, we obtain *(i)* the fraction of events at $z = \{0.55, 0.7, 1\}$ whose host galaxy could be identified; *(ii)* the impact on parameter estimation of removing the degeneracies with the sky position angles and, finally, *(iii)* the associated error in the estimation of w from an observation of a single SMBH merger event. Neglecting weak lensing effects and for a fiducial redshift of $z = 0.7$, we find that $\Delta w \sim 0.4\% - 5.5\%$, depending on the mass parameters of the event; however, weak lensing effects at these distances are expected to induce a 4% error in the estimation of D_L, which translates into an 20% error in w. So, the clear conclusion here is that LISA's potential as a new tool for precision cosmography is limited by the weak lensing effects in the redshift range $0.55 < z < 1$ rather than by the statistical errors in its measures, and therefore, further in-depth studies are urgently needed on ways to correct for weak lensing.

Search for galactic binary systems with LISA using MCMC

Also, there has been a great effort within the LISA community [5–8] in developing search tools. LISA will observe thousands of overlapped GW signals in a single strain time series, $h(t)$, and it will be a data analysis task to disentangle them and extract information about physical parameters. The work presented in Chapters 6 and 7 goes in this direction and in particular, we think that MCMC implementations (combined with RJMCMC in order to deal with multiple sources in a Bayesian way; and enhanced with the DR algorithm to efficiently explore multimodal distributions) can play an important role in LISA searches.

In this thesis we have started the implementation of a MCMC-based search algorithm for single and multiple (but fixed number of) galactic binary signals (see Chapter 6). This is still work in progress as we are currently testing an RJMCMC implementation that will allow us to search for an unknown number of sources and even, to search for different kind of signals simultaneously (*e.g.* galactic binaries, SMBH inspirals and EMRIs) and estimate the number of them present in the data using all the power of Bayesian statistics. In parallel to this effort, we have developed a completely general and fully Markovian method to efficiently explore multimodal distributions based on the delayed rejection (see Chapter 7). This algorithm can be used in any MCMC problem presenting a target distribution with a (roughly known) multimodal structure [this was the motivation for submitting our article presented in Chapter 7 to a more general journal on computational statistics and data analysis]; and, in particular, we think that this algorithm can be applied to increase the efficiency of the MCMC-search for most of LISA sources.

Accuracy and effectualness of BBH waveform models

Ground-based detectors have reached their design sensitivity and the first direct detection of a GW should become a fact in the next few years, with CBCs being one of the most promising sources. For this reason it is crucial to have available fast and accurate model waveforms and, in any case, to understand the validity range of any approximated model one has at hand. The study performed in Chapter 8 tries to establish, in a formal and exhaustive way, these boundaries for the fastest, closed-form, frequency-domain model waveforms (PN-SPA and phenomenological models), using EOB waveforms as reference [which have shown to be more accurate than the former, though also slower to generate].

Our conclusions are that current closed-form models can be used for detection purposes in searches for CBCs with mass ratio $q \in (1, 4)$ and missing less than 6% of potential events in case of initial detectors, and less than 9% when considering advanced detectors. The construction of new phenomenological waveform models in a wider range of mass ratios, could extend these results. When one is interested in extracting reliable physical information [biases smaller than typical statistical errors] from the GW observations, then more accurate models shall be required in any case.

We also have obtained the compatibility range between EOB and PN waveforms in terms of frequency, separation distance and number of orbits before merger (see Fig. 4 in Chapter 8), finding, for 4:1 and 10:1 systems, an important gap (of several tens of orbits) between the upper limit of this range and the merger. Currently, the longest NR simulations only span $\sim 10 - 15$ orbits.

We think that the results presented in this work should be useful for the LSC in order to choose between the different waveform models that are used when performing a search. We also wish that in future works, the accuracy standards introduced in Chapter 8 and by other authors [9–12] are used rigorously (as they have been originally presented); remaining faithful to their mathematical and physical meaning.

Future work and final remarks

All the studies performed in this PhD thesis have considered *non-spinning* compact objects and, except for the galactic binary signals (which would be quasi-monochromatic anyway), we have *neglected a possible equation of state* of the matter conforming the compact object; which is valid in case of BHs, but just an approximation for NSs. Thus, the natural extension of some of these results would be *(i)* to also consider spinning systems and furthermore, *(ii)* to start investigating the potential astrophysics that can be done from GW observations of NSs.

From the results obtained in Chapter 8, it seems clear that there is still a long road ahead in order to obtain fast and accurate template banks. On one hand, for mass ratios greater than 4:1, we have found a gap of several tens of orbital cycles between the high-frequency end of the PN validity range and the merger, that will have to be filled using more accurate analytical methods, such as EOB, given the fact that current NR simulations are limited to $\sim 10 - 15$ orbits long. Also, on the other hand, the accuracy of the closed-form, frequency-domain waveforms is not good enough to exploit all the scientific potential that ground-based CBC observations have; thus, our future plans also include the investigation of building EOB-based, or NR-based, template banks.

Also, we are in the process of upgrading our MCMC-based search algorithm to a 'DR-RJMCMC' scheme that should represent the core of a search algorithm to deal with the "whole enchilada" of GW sources that will be an actual LISA data set, and also the next MLDC-4 [8].

Finally, let us point out that all the studies presented in this thesis are theoretical, in the sense that no actual data from current GW detectors have been used. However, during this period, the PhD candidate has also collaborated within the LSC in the search for continuous waves emitted by rapidly rotating NSs using the Hough transform and he also took part during three months of the LSC Astrowatch program for students to operate the 2 km LIGO interferometer in Hanford (H2) between S5 and S6 science modes (February 2008 – June 2009).

During these last four years of PhD, the LSC has published 39 scientific articles in which the candidate appears as a co-author.

References

[1] M. Trias, A. M. Sintes, Class. Quant. Grav. **25** 184032 (2008).

[2] M. Volonteri, F. Haardt, P. Madau, Astrophys. J. **582** 559-573 (2003).

[3] M. C. Begelman, M. Volonteri, M. J. Rees, Mon. Not. Roy. Astron. Soc. **370** 289-298 (2006).

[4] K. G. Arun *et al.*, Class. Quant. Grav. **26** 094027 (2009).

[5] K. A. Arnaud *et al.* [MLDC Collaboration], Class. Quant. Grav. **24** S529-S540 (2007).

[6] S. Babak *et al.* [MLDC Task Force Collaboration], Class. Quant. Grav. **25** 114037 (2008).

[7] S. Babak *et al.* [MLDC Task Force Collaboration], Class. Quant. Grav. **25** 184026 (2008).

[8] S. Babak *et al.* [MLDC Task Force Collaboration], Class. Quant. Grav. **27** 084009 (2010).

[9] T. Damour, B. R. Iyer, B. S. Sathyaprakash, Phys. Rev. D **57** 885-907 (1998).

[10] L. Lindblom, B. J. Owen, D. A. Brown, Phys. Rev. D **78** 124020 (2008).

[11] L. Lindblom, Phys. Rev. D **80** 064019 (2009).

[12] L. Lindblom, J. G. Baker, B. J. Owen, Phys. Rev. D **82** 084020 (2010).

List of Acronyms

ADM   Hamiltonian formulation of GR developed by Arnowitt, Deser and Misner.

AP   asymmetrical proposal

BBH   binary black hole

BBO   Big Bang Observer

BH   black hole

BSSN   Formalism developed by T. W. Baumgarte, S. L. Shapiro, M. Shibata and T. Nakamura from 1987 to 1999, which is a modication of the ADM formalism Hamiltonian formulation of GR.

CBC   compact binary coalescence

CPU   central processing unit (part of a computer system)

DA   data analysis

DE   dark energy

DECIGO   DECi-hertz Interferometer Gravitational wave Observatory

DR   delayed rejection

ECP   evolution of the center of the proposal

EM   electromagnetic

EMRI   extreme mass ratio inspiral

EOB   effective-one-body

EoS   equation of state

ESA   European Space Agency

ET   Einstein Telescope

FFT   Fast Fourier Transform

FIM   Fisher information matrix

FLRW   Friedman-Lemaître-Robertson-Walker

FT   Fourier transform

FWF   full waveform

GR   general relativity

GW   gravitational wave

HH   higher harmonic

INFN   Istituto Nazionale di Fisica Nucleare

ISCO   innermost stable circular orbit

LCGT   Large Cryogenic Gravitational Telescope

l.h.s.   left hand side

LIGO   Laser Interferometer Gravitational-wave Observatory

LISA   Laser Interferometer Space Antenna

LISA PE   LISA Performance Evaluation (Taskforce)

LSA   linearized-signal approximation

LSC   LIGO Scientific Collaboration

LSO   last stable orbit

LWA   long wavelength approximation

MC   Monte Carlo

MCMC   Markov chain Monte Carlo

MH   Metropolis-Hastings

ML   maximum likelihood

MLDC   Mock LISA Data Challenges

MM   minimal match

NASA   National Aeronautics and Space Administration

NR   Numerical Relativity

NS   neutron star

ODE   ordinary differential equation

PDF   probability density function

PN   post-Newtonian

PSD   power spectral density

r.h.s.   right hand side

RJMCMC   reversible jump Markov chain Monte Carlo

r.m.s.   root-mean-squared

RWF   restricted waveform

SMBBH   supermassive binary black hole

SMBH   supermassive black hole

SN   supernova

SNR	signal-to-noise ratio
SPA	Stationary Phase Approximation
SSB	Solar System Barycenter
TDI	time delay interferometry
TOA	time of arrival
TT	transverse-traceless
WD	white dwarf